UNIVERSITÄT DUISBURG ESSEN

Open-Minded

Behavior of toxicologically relevant silver compounds and barium sulfate particles in complex media: from synthesis to biological investigations

Dissertation

zur Erlangung des akademischen Grades eines
Doktors der Naturwissenschaften
– Dr. rer. nat. –

vorgelegt von

Kateryna Loza

geboren in Henitschesk/Ukraine

Institut für Anorganische Chemie
der
Universität Duisburg-Essen

2015

Die vorliegende Arbeit wurde im Zeitraum von Oktober 2011 bis November 2015 im Arbeitskreis von Prof. Dr. Matthias Epple am Institut für Anorganische Chemie der Universität Duisburg-Essen durchgeführt.

Tag der Disputation: 14.04.2016

Gutachter:	Prof. Dr. Matthias Epple
	Prof. Dr. Christian Mayer
Vorsitzender:	Prof. Dr. Stefan Rumann

List of contents

1 Introduction

An unintended exposure to particulate form materials may occur during different stages of the production, use and recycling of particulate systems. They may enter the food chain, water and air, and thus have environmental consequences through their interactions with nutrients and environmental pollutants.[1-10] It is known that ultrafine particles exhibit special properties that make them rather different from their corresponding bulk-scale equivalents. An increased specific surface area and quantum size effects are the main differentiating properties. However, the fate of ultra-fine particles in biological systems can be different from that of bulk material with the same composition. This work was performed to study the behavior of engineered particles under the conditions of biological environments. It is known that the specific surface area, solubility, hydrophobicity, surface functionalization, surface charge, colloidal stability, and particulate morphology may all influence the biological effects of nanomaterials. For that reason, questions concerning the mechanism of interaction on the cellular level are highly significant for this research.

Within the framework of this thesis, two exemplary systems were addressed. As the model of a biologically active material, silver compounds and silver nanoparticles were investigated in particular. In contrast, barium sulfate was considered as a bioinert system. Extensive use of silver and barium sulfate in nanoparticulate forms in different applications was reported.[1, 2, 4-6, 11-25] The morphological and colloidal characterization of particles has proven strong connections between properties such as average particle size, shape, and dispersity and inherently tuneable physico-chemical behavior.[26-28] As previously reported, the biological responses to small particles differ from responses to larger particles of the same composition.[27, 29] Considerable attention has been paid to investigations in complex media like physiological salt solutions and serum-rich environments, since particle interaction can depend on the presence of various components. This point is often underestimated when performing adequate control experiments. The interactions of silver compounds with biological media are

non-trivial cases, while catalytic reactions on the particle surface which depend on the size and shape of the nanoparticles can render the system very complicated.[11, 20, 30-33]

This work comprises an attempt to correlate the synthesis procedures of toxicologically relevant particles and their behavior in complex biological media in terms of stability and dissolution with specific biological responses.

2 Theoretical background

2.1 Definition and properties of colloidal systems

The term *colloid* was introduced by Graham in 1861, from Greek meaning glue-like.[34] The word *colloidal* refers to a state of division, indicating that the molecules or polymolecular particles dispersed in a medium have a minimum dimension in one direction between of approximately 1 nm and 1 µm, or that discontinuities are found at distances of that magnitude in a system.[35] Colloidal systems are combinations of two or more components. Another definition states that colloidal particles exist in a dispersed state and are intermediate in size between molecules and the smallest particles visible under an optical microscope. It is not essential for all three dimensions to be in the colloidal range. Colloidal dispersions are metastable mixtures. Although they are likely to form stable discrete phases upon storage, this can be a slow process. Gold sols prepared by Faraday in 1857 remain unchanged until today, *i.e.* more than 150 years after their synthesis.[36]

A colloidal system or dispersion contains particles of colloidal size, referred to as the *dispersed substance*, spread throughout a *dispersing medium*.[36] Table 1 provides examples of systems constituting a colloidal domain.

Table 1: Examples of colloidal systems.[36]

Dispersed substance	Dispersing medium	Common name	Examples
Liquid	Gas	Liquid aerosol	Fog
Solid	Gas	Solid aerosol	Smoke
Gas	Liquid	Foam	Whipped cream
Liquid	Liquid	Emulsion	Mayonnaise
Solid	Liquid	Sol	Paint
Gas	Solid	Solid foam	Marshmallow
Liquid	Solid	Solid emulsion	Opal
Solid	Solid	Solid sol	Some alloys

Colloidal systems often possess special physical and chemical properties. For instance, the electronic, optical, and chemical properties of the described systems may be varied by each component in the bulk form.

In principle, there are two different approaches to the production of colloidal systems. The first method is called dispersion or the top-down approach. It is actually based on breaking down a system into its compositional sub-systems. Tools are used to cut, mill, and form materials into the desired shape and order. In this method, large particles of the substances are converted into particles of colloidal dimensions in the presence of a dispersion medium. Systems formed in this way are often highly unstable. To mitigate this effect, additional components are often used.

The second principal way to produce colloids is condensation or aggregation. This tactic is the so-called bottom-up approach. It relies on material synthesis from atomic or molecular species via chemical reactions, allowing particles to grow in size. In this case, the original systems are sub-divisions of the emergent structure. This method consists of chemical reactions or changes of solvents whereby the atoms or molecules of the dispersed phase appear first, aggregating to form colloidal particles. To prevent

further growth, the conditions can be varied to permit the formation of sol particles. The control conditions are concentrations of the solutions, the presence of surfactants, and the temperature. Notably, the bottom-up approach uses the chemical properties of single molecules or atoms to cause self-organization into the desired formation.

Due to their intrinsic physical and chemical properties, colloids are widely used in various fields of electronics, energy harvesting, water supply, geoscience and medicine.[15, 37-43]

2.2 Stability of colloids

Since a colloidal system is defined as a combination of two or more components, a separation of these components may occur over time when they are exposed to the physical environment. The term of stability may rely on the physical state of the system: whether it is stable or dispersed. The forces that change this metastable state can be body forces as well as chemical transformation (*e.g.,* surface oxidation).

Unstable colloids tend to form aggregates or agglomerates. Upon reaction to external actions like stirring, mixing, milling, or sonication, such a formation can be reversible or irreversible. The irreversible form is often called coagulation.[34, 44]

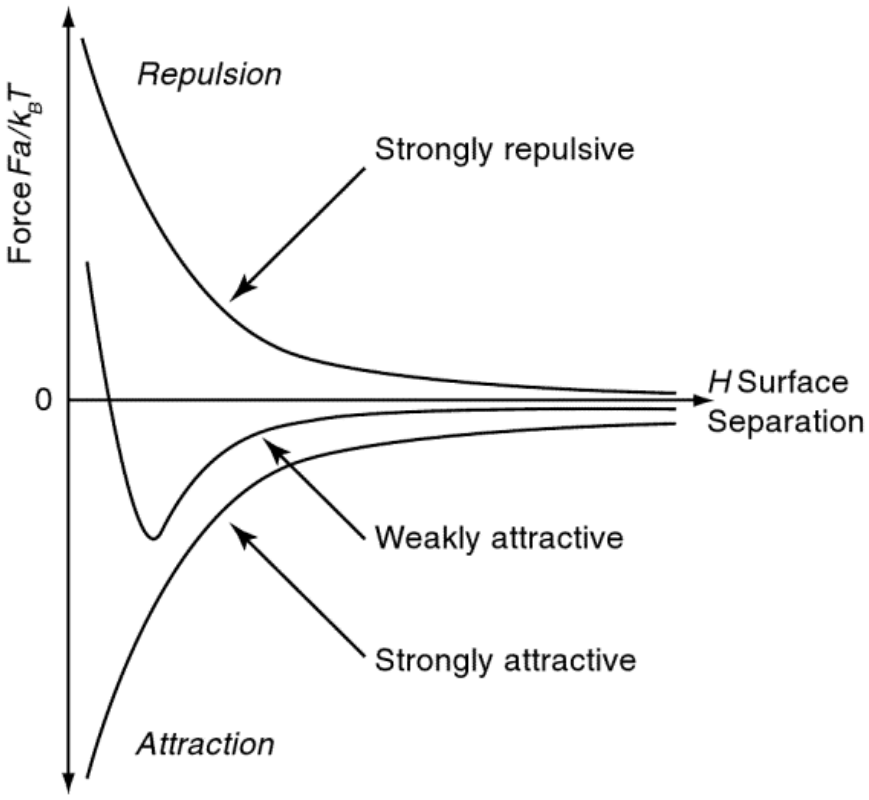

Figure 1: The interaction forces between pairs of colloidal particles.[34]

Using the DLVO theory (theory of Derjagin, Landau, Verwey and Overbeek), it is possible to describe the stability of colloidal disperse systems. Their stability comes from interactions between attractive and repulsive forces. Here, van der Waals forces play the role of attractive forces, and electrostatic forces act as repulsive forces. Figure 1 describes the interaction of forces between pairs of colloidal particles. Provided that the net interaction energy is sufficiently repulsive, the particles cannot collide and stick together. The greater the repulsion, the more stable the system.[34, 44]

In the presence of the Earth's gravitation field, this additional force will act on particles in the colloidal state. The particles will have a tendency to sediment if the dispersing medium is less dense. The sedimentation velocity can be estimated using the equation of Stokes drag with gravitational force:

$$v_s = \frac{2}{9}\frac{\Delta\rho g a^2}{\eta_0}$$

where v_s is the sedimentation velocity, $\Delta\rho$ is the difference of densities, g is the gravitational constant, a is the particle radius, and η_0 is the medium viscosity. It can be shown easily that the larger the particles, the greater the tendency to sediment. Colloidal particles will still sediment, even when attractive forces are small. Aggregates will sediment faster.[34]

To prevent colloidal systems from altering, they can be enhanced by electrostatic or steric stabilization. Electrostatic stabilization of colloids is the mechanism used to counterbalance the van der Waals attraction with the repulsive Coulomb forces acting between the charged colloidal particles. The electric double layer plays a fundamental role in the electrostatic stabilization of sols. Particles can gain an electric charge when charged ions of the dispersion medium are adsorbed onto the particles surface. The electric double layer is the layer surrounding a particle of the dispersed phase, including the ions adsorbed on the particle surface and a layer of the counter-charged dispersion medium. Overall, it is electrically neutral.

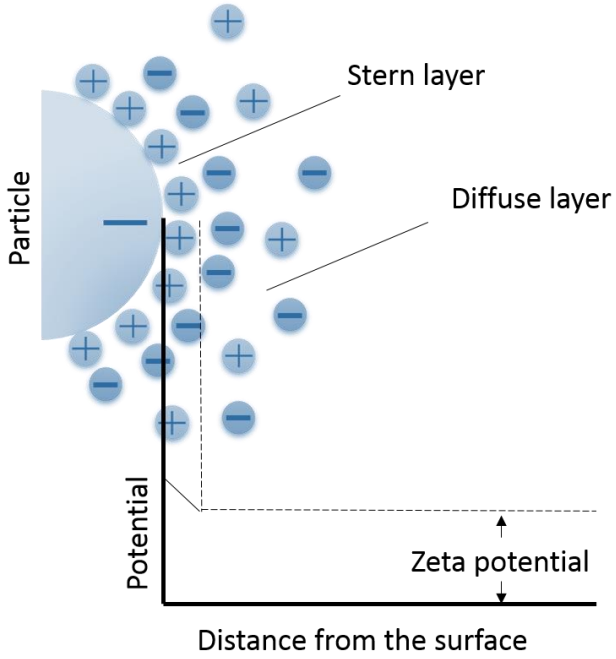

Figure 2: Schematic representation of electric double layer.

An electric double layer representation is shown in Figure 2. The Stern layer is created by counter ions (with opposite charge) attracted to the particle surface and closely attached by the electrostatic force. A diffuse layer can appear as a film of the dispersion medium next to the particle. The diffuse layer contains free ions with a higher concentration of counter ions. The ions of the diffuse layer are affected by the electrostatic force of the charged particle. The electrical potential within the electric double layer has its maximum on the particle surface (Stern layer).

Depletion stabilization, another tactic of colloid stabilization, uses polymeric molecules added to the dispersion medium to prevent the aggregation of particles. The polymeric chains produce a repulsive force, counterbalancing the attractive van der Waals force acting on a particle approaching another particle. The two types of such stabilization are shown in Figure 3.

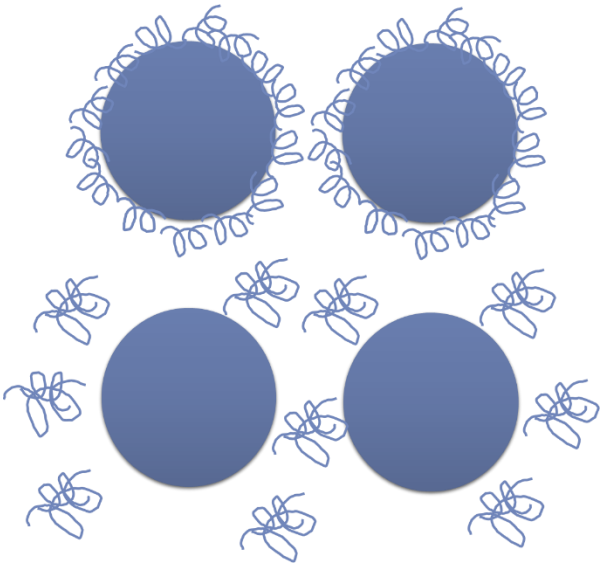

Figure 3: Schematic representation of depletion stabilization of colloids.

Steric stabilization (upper particles in Figure 3) of colloids is achieved by polymer molecules attached to the particle surface forming a coating, which creates a repulsive force and separates the particles from others. Depletion stabilization (lower particles in Figure 3) of colloids involves unanchored (free) polymeric molecules creating repulsive forces between the approaching particles. The increased amount of polymer reduces the probability that two colloidal particles will touch.[34, 44]

Electrosteric stabilization is a combination of the two mechanisms. At the same moment the electrostatic stabilization and the steric stability can be imparted by the polymer. Electrosteric stabilization is usually associated with the adsorption of polyelectrolytes onto the particle surface.[45]

2.3 Toxicologically relevant particles

Toxicology is a branch of biology, chemistry, and medicine concerned with the study of adverse effects of chemicals on living organisms. The main object of study is the damaging properties of chemical, biological and physical agents in biological systems. Nanotoxicology is a sub-division of particle toxicology. It addresses the toxicology of

ultrafine particles which appear to have harmful effects that are atypical for bulk material of the same composition. This field of study was established due to a large increase in nanoscale material production and use. It is known that ultrafine particles exhibit extraordinary properties that make them rather different from their corresponding bulk-scale equivalents. An increased specific surface area and quantum size effects are the main properties of interest. This results in different interactions with molecules (including biomolecules) at the surface of nanoparticles, which may lead to the ability to create materials with novel properties and applications.

An unintended disposal of particulate materials may occur during different stages of production, use, and waste. They may enter the food chain, water and air, and thus have environmental consequences through their interactions with nutrients and environmental pollutants. For example, it has been shown that particulate air pollution in urban areas can be linked with acute increases in morbidity and mortality rates, especially for persons with obstructive lung and cardiovascular diseases.[46-51] An early key study demonstrated that ultrafine TiO_2 caused greater inflammation in rat lungs than exposure to the same airborne mass concentration of fine TiO_2.[28, 52] Dermal exposure to nanoparticulate systems in sunblock cream is already occurring and this trend is increasing.[53, 54] Nanoparticles in food were reported to cross into the gut lymphatics and redistribute into other organs more readily than larger particles.[55, 56]

2.3.1 Silver compounds

Bacteria can adhere to and colonize the surfaces of various materials. Uncontrolled bacterial growth may result in the formation of bacterial biofilms which makes antibiotic treatment difficult if not ineffective.[57, 58] In toxicology, silver is well known for its biocidal action. Herodot has already mentioned the antibacterial action of silver.[59] Today, silver is still progressively implemented in many applications to move away from biocidal organic chemical agents towards inorganic additives. Silver can be used in much lower concentrations in a wider variety of products, including applications such as plastics, where high-temperature processing is not possible with organic compounds. Examples

of applications include: bacteriostatic water filters for household use; swimming pool algaecides; consumer commodities like mobile phones, refrigerators, and clothes; medical devices like catheters, implant surfaces, and plasters.[1, 2, 4-6, 11-22]

Experimental investigations have shown that the biocidal action results from the interaction of silver ions with bacteria.[11, 60, 61] To satisfy the diversity of application types, numerous different forms of silver compounds have been developed to serve the market. They can be primarily differentiated by the way the silver ions are stored in the product. Common silver products range from additives that store and release discrete silver ions from a ceramic or glass matrix, to products that contain silver ions as sparingly soluble silver salts (*e.g.,* Ag_2S, AgCl) or elemental silver (*e.g.,* nanoscale silver metal).

Humans can be exposed to silver nanoparticles through different ways. This can occur orally (*e.g.*, by colloidal solutions), dermally (*e.g.*, in contact with jewelry or burn creams), and via the inhalation of dusts or fumes. This is a major concern in handling silver nanoparticles at the point of production and during the manufacture of nanoparticle-containing materials. The interaction of silver compounds in biological media can be complex due to the reactions on the particle surface. Size and shape effects make the system even more complicated.[11, 20, 30-33]

2.3.2 Barium sulfate

Barium sulfate is an inorganic compound. It occurs as the mineral barite, which is the main commercial source of barium. Its white opaque appearance and high density leads to a wide range of possible applications such as oil drilling fluid, oil pigments ("permanent white"), paper brightener, and plastic filler.[23, 24] In medicine, barium sulfate is known as a radiocontrast agent; in the form of a suspension, it is frequently used for imaging of the digestive system and administrated orally.[25] The low solubility of barium sulfate protects the patient from absorbing harmful amounts of the toxic metal. During production, shipping, handling, incorporation into final products, and the use and disposal of products containing barium sulfate, an unintended exposure to aerosolized

$BaSO_4$ particles of different size and morphology may occur. Chronic exposure leads to baritosis in miners; nine cases of baritosis were described in a small factory in which barite was crushed, graded, and milled.[9]

In biological investigations, it is often assumed that the behavior of barium sulfate is similar to other poorly soluble materials. Most studies have described the lung clearance of intratracheally instilled micron-sized radioactive $BaSO_4$, and showed that the particle size influences the lung clearance of barite.[8, 62] In general, biological responses to small particles differ from responses to larger particles of the same composition.[27, 29] Moreover, the principal mechanisms of the lower toxicity and rapid lung clearance of $BaSO_4$ particles are not fully understood.[63]

3 Materials and methods

3.1 Dynamic light scattering

Dynamic light scattering (DLS) is a method that can be used to determine the size distribution profile of particles in suspension or polymers in solution. In addition, it is possible to make a statement about the dispersity of a sample. In the dispersion medium, particles move randomly in accordance with the Brownian motion. Upon irradiation, light will be scattered by the colloidal particles. Depending on the position of the individual scatterer, constructive and destructive interference will occur. This leads to time-dependent fluctuations in the scattered light intensity, which can be measured by a detector. From the correlation of time and light intensity, an auto-correlation function can be determined. By function analysis, the diffusion coefficient of the particles can be investigated. If temperature and solvent viscosity are known, the hydrodynamic diameter can be estimated.

The hydrodynamic diameter and the zeta potential of the dispersed nanoparticles were measured by dynamic light scattering using a Malvern Zetasizer Nano ZS instrument. The polydispersity index (PDI) was below 0.3 in all cases, indicating a good degree of dispersion.[44]

3.2 Nanoparticle tracking analysis

Nanoparticle tracking analysis (NTA) is a method for visualizing and analyzing particles in liquids. This technique is based on the relationship of Brownian motion to particle size. Using a microscope, particles moving under Brownian motion can be detected. By image analysis, the average distance moved by each particle can be determined. This value allows the diffusion coefficient to be calculated. The hydrodynamic diameter of the aggregate can be estimated from the Stokes-Einstein equation:

$$D_t = \frac{Tk_B}{3\pi\eta d}$$

where D_t is the particle diffusion coefficient, T is the temperature, k_B is the Boltzmann's constant, η is the solvent viscosity, and d is the hydrodynamic diameter.

NTA results in a size distribution profile of small particles with a diameter of approximately 10-1000 nm in liquid suspension. The examination was performed with a NanoSight LM10 HS instrument.

3.3 Fluorescence spectroscopy

Fluorescence spectroscopy is a type of electromagnetic spectroscopy that analyzes fluorescence from a sample. This method is used for the qualitative and quantitative measurement of the fluorescence emission of substances after excitation with a light source. The typical wavelength of irradiation is between 200 and 1000 nm. A beam of light excites the electrons in molecules of specific compounds and causes them to emit light. At low concentrations, the fluorescence intensity will usually be proportional to the concentration of the fluorophore. Fluorescence spectroscopy was carried out with a Carry Eclipse fluorescence spectrophotometer.

3.4 Atomic absorption spectroscopy

Atomic absorption spectroscopy is used for the quantitative determination of individual elements. The method is based on the absorption of optical radiation by free atoms in the gaseous state. The test sample is converted to the gaseous state and atomized by means of thermal dissociation: by being sprayed into a flame while in its dissolved form. The atoms in the ground state then absorb optical radiation, which they will emit in the excited state. The light source is a hollow cathode lamp, which is made of the element to be determined. Standards with known analyte contents are required to establish the relationship between the measured absorbance and the component concentration. This relation relies on the Lambert-Beer law.

The concentration of silver was determined by atomic absorption spectroscopy (Thermo Electron Corporation, M-Series). The detection limit for silver was 1 µg L^{-1}. Prior to analysis, silver nanoparticles were dissolved with nitric acid. Silver chloride was dissolved with ammonia solution.

3.5 Energy-dispersive X-ray spectroscopy

Energy-dispersive X-ray spectroscopy (EDX) is suitable for the qualitative and semi-quantitative analysis of the elemental constituents of solids. This method is based on the interaction between some sources of X-ray excitation and a sample. Each element has a unique atomic structure, resulting in a unique set of peaks in its X-ray emission spectrum.[64] The high-energy beam excites an electron in an inner shell, ejecting it from the shell. In this way, an electron hole is created. An electron from an outer (higher-energy shell) then fills the hole. The energy difference between the higher-energy shell and the lower energy shell may be released as X-ray photon. Photon number and energy of the X-rays emitted from a specimen can be measured by an energy-dispersive spectrometer. The energies of the X-rays are characteristic for the difference in energy between the two shells and the atomic structure of the emitting element. All elements with an atomic number >4 are detectable; the sensitivity increases with increasing atomic number.

3.6 Thermogravimetric analysis

Thermogravimetry (TG) is a thermal analysis method based on the measurement of a change in mass of a substance during a specific temperature program. The result can be plotted as mass change with temperature and time. TG can provide information about first-order phase transitions, including vaporization, sublimation, absorption, adsorption, and desorption. Similarly, TG can provide information about chemical processes like chemisorption, dehydration, decomposition, oxidation or reduction.[65] The profile of the mass loss usually contains characteristic regions, which can be associated with physical or chemical transformations.

The experiments were carried out in a dynamic oxygen atmosphere at a heating rate of 2 K min^{-1} in alumina crucibles. During thermogravimetric examination, the sample was heated up to 1273 K. The examination was performed with a TG 449 F3 Jupiter Netzsch instrument.

3.7 X-ray powder diffraction

X-ray diffraction is an analytical method for investigations of the atomic and molecular structure of a crystal. It is often used to identify unknown substances, to determine different polymorphic phases of the same material, and to ascertain the purity of a known substance. Crystals are regular arrays of atoms, and X-rays can be considered as waves of electromagnetic radiation. X-ray diffraction is based on the constructive interference of monochromatic X-rays and a crystalline sample. When the geometry of the incident X-rays impinging the sample satisfies Bragg's law, constructive interference occurs and a peak in intensity occurs. Bragg's law:

$$n \cdot \lambda = 2d \cdot sin\theta$$

where n is a positive integer, λ is the wavelength of incident wave, d is the spacing between diffracting planes, and θ is the incident angle. By measuring the angles and intensities of the diffracted beams, structural information can be obtained. The diffraction peak positions can be converted to *d*-spacings. This allows the identification of the mineral by comparing *d*-spacings with standard reference patterns. X-ray diffractometers consist of three basic elements: An X-ray tube, a sample holder, and an X-ray detector. X-rays are generated in a cathode ray tube by heating a filament to produce electrons, accelerating the electrons toward a target by applying a voltage, and bombarding the target material with electrons.

X-ray powder diffraction was carried out on a Bruker D8 Advance instrument in Bragg-Brentano mode with Cu Kα radiation (1.54 Å; 40 kV and 40 mA), using a silicon single crystal with a crystallographic (911) plane as a sample holder to minimize scattering.

For better homogenization, the dried powder samples were redispersed with ethanol on the silicon surface and then investigated in the range of 5 to 90 °2θ with a step size of 0.01 °2θ and a counting time of 0.6 s. Rietveld refinement (Le Bail method) with the program package TOPAS 4.2 from Bruker was performed to determine the average crystallite size and lattice parameters. For each Rietveld refinement, the instrumental correction determined with a standard powder sample LaB_6 from NIST (National Institute of Standards and Technology) and standard reference material (SRM 660b; $a(LaB_6)$=4.15689 Å) was taken into account. As a reference, a microcrystalline silver powder was also studied (Fluka, sintered for 3 h at 700 °C to ensure microcrystallinity and the absence of microstrain), mixed with LaB_6. All powder diffraction data were obtained at ambient temperature, *i.e.* at 25±2 °C.

The size of the crystallites was calculated with the Scherrer equation:

$$D = \frac{K \cdot \lambda}{FWHM \cdot cos\theta}$$

with K a constant set to 0.89, λ the wavelength of the X-ray radiation, $FWHM$ the full width at half maximum for the diffraction peaks, and θ the diffraction angle.

3.8 Scanning electron microscopy

A scanning electron microscope (SEM) is a type of electron microscope that produces images of a sample by scanning it with a focused beam of electrons. SEM is usually used to depict structures if their dimensions are smaller than half the wavelength of visible light, and so they cannot be imaged with light microscopic techniques due to the Abbe diffraction limit. The electrons interact with atoms in the sample, producing various signals that can be detected and that contain information about the sample surface topography and composition. The secondary electron (SE) signal is the most often used signal. It varies with the topography of the sample surface: Edges are bright, recesses are dark. Backscattered electrons (BSE) consist of high-energy electrons that are back-scattered out of the specimen interaction volume by elastic scattering

interactions with sample atoms. BSE are often used to detect a contrast between areas with different chemical compositions, because heavy elements backscatter electrons more strongly than light elements.

All scanning electron microscopic examinations were performed with ESEM Quanta 400 FEG (FEI) instrument. All measurements were performed in high vacuum mode. If the specimen contained any volatile components such as water, they were put through a drying process before use in the high vacuum system. Because non-conducting specimens will accumulate charge under electron bombardment, they were coated with a conducting layer (Au:Pd = 80:20). Typical thicknesses were in the range 2-15 nm, depending on the sample and application. However, the cover layers should not be visible at the chosen magnification. A planar silicon wafer was used as a substrate. It was washed with acetone before the application. It was then mounted with carbon tape on an aluminum sample holder.

3.9 Transmission electron microscopy

Transmission electron microscopy (TEM) is a microscopic technique in which a beam of electrons is transmitted through an ultra-thin specimen, interacting with the specimen as it passes through. An image is formed from the interaction of the electrons transmitted through the specimen. There are four main components in a transmission electron microscope: An electron optical column, a vacuum system, the necessary electronics (lens supplies for focusing and deflecting the beam) and the high voltage generator for the electron source. The specimen must be thin enough to transmit the electrons. Passing through the specimen, transmitted electrons are collected and focused by the objective lens and a magnified real image of the specimen is projected by the projection lenses onto the viewing device at the bottom of the column.

Transmission electron microscopy was carried out with a CM200 FEG-Instrument (Philips) with a Supertwin-Lens, operated at an accelerating voltage of 200 keV. The

samples were ultrasonically dispersed in ethanol and then transferred to holey carbon-coated copper grids.

4 Experimental section

4.1 Synthesis of silver nanoparticles

Poly(vinylpyrrolidone) (PVP)-coated silver nanoparticles were synthesized by reduction of silver ions with glucose (Figure 4) in the presence of PVP (Figure 5) in aqueous medium according to *Wang et al.*[66]

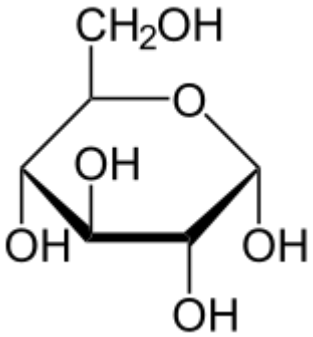

Figure 4: Haworth projection of D-(+)-glucose.

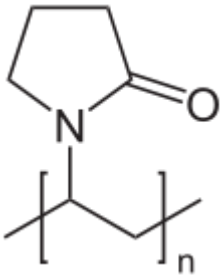

Figure 5: Structural formula of poly(vinylpyrrolidone).

Here, 2 g glucose (11.10 mmol) and 1 g PVP (0.025 mmol based on the molar mass of the monomer; M_w = 40,000 g mol^{-1}) were dissolved in 40 g water and heated to 90 °C in a silicon oil bath for 30 min. Then, 0.5 g $AgNO_3$ (2.94 mmol) dissolved in 1 mL water was quickly added. Prior to addition, the silver nitrate solution was kept under light exclusion. The dispersion was kept at 90 °C for 1 h and then allowed to cool to room temperature. The synthesis was carried out under continuous vigorous stirring. During

the reaction, the color of the solution changed from transparent pale yellow to opaque grey. The particles were collected by ultracentrifugation (29,400 g; 20,000 rpm; 30 min), redispersed in pure water and collected again by ultracentrifugation. In that way, NO_3^-, excess glucose and its oxidation products, excess polymer, and excess Ag^+ were all removed. Then, the silver nanoparticles were redispersed in pure water by ultrasonication. In the last step, degassed and argon-saturated ultrapure water was used in order to avoid a release of silver ions from the particles during storage. All samples were stored at 4 °C in the dark until further analysis. The nanoparticles were characterized by scanning electron microscopy, energy-dispersive X-ray spectroscopy, dynamic light scattering, and nanoparticle tracking analysis. The final silver concentration in all dispersions was determined by atomic absorption spectroscopy.

4.1.1 Synthesis of silver nanoparticles under partial air exposure and exposure to ambient light

To study the influence of partial air exposure and exposure to ambient light, the synthesis according to *Wang et al.* was modified.[66] For this, 16 g glucose (88.80 mmol) and 8 g PVP (0.2 mmol based on the molar mass of the monomer; M_w = 40,000 g mol^{-1}) were dissolved in 320 mL water and heated to 90 °C. Then 4 g $AgNO_3$ (23.55 mmol) dissolved in 8 mL water was quickly added. Prior to the addition, the silver nitrate solution was kept under light exclusion. The dispersion was kept at 90 °C for different times (up to 7,000 min) and then allowed to cool to room temperature. For partial air exposure, a synthesis was performed in an Erlenmeyer flask covered with a concave watch glass. The system was heated to 90 °C in a silicon oil bath under ambient light exposure. The synthesis was carried out under continuous vigorous stirring. Aliquots of the reaction mixtures were taken after selected time periods. At each point, a 10 mL aliquot of the solution was taken with a syringe. The particles were collected and separated from synthesis by-products by ultracentrifugation (29,400 g; 20,000 rpm; 30 min), redispersed in pure water and collected again by ultracentrifugation. This procedure was repeated three times. Thereby nitrate, excess glucose and its oxidation

products, excess PVP, and excess silver ions were removed. After the third cycle the sample was redispersed in 10 mL of distilled water. All samples were stored at 4 °C in the dark until further analysis.

4.1.2 Synthesis of silver nanoparticles under exposure to ambient light

To study the influence of exposure to ambient light, the synthesis according to *Wang et al.* was modified.[66] For this, 16 g glucose (88.80 mmol) and 8 g (0.2 mmol based on the molar mass of the monomer; M_w = 40,000 g mol^{-1}) PVP were dissolved in 320 mL water and heated to 90 °C. Then 4 g $AgNO_3$ (23.55 mmol) dissolved in 8 mL water was quickly added. Prior to addition, the silver nitrate solution was kept under light exclusion. The dispersion was kept at 90 °C for different times (up to 7,000 min) and then allowed to cool to room temperature. The system was heated to 90 °C in a silicon oil bath under ambient light exposure. A synthesis was carried out in a round bottom flask with a reflux condenser (water cooling) under exposure to ambient light. All syntheses were carried out under continuous vigorous stirring. Aliquots of the reaction mixtures were taken after selected time periods. At each point, a 10 mL aliquot of the solution was taken with a syringe. The particles were collected and separated from the synthesis by-products by ultracentrifugation (29,400 g; 20,000 rpm; 30 min), redispersed in pure water and collected again by ultracentrifugation. This procedure was repeated three times. Thereby nitrate, excess glucose and its oxidation products, excess PVP, and excess silver ions were removed. After the third cycle, the sample was redispersed in 10 mL of distilled water. All samples were stored at 4 °C in the dark until further analysis.

4.1.3 Synthesis of silver nanoparticles under light exclusion

To study the influence of light exclusion, the synthesis according to *Wang et al.* was modified.[66] Here, 16 g glucose (88.80 mmol) and 8 g PVP (0.2 mmol based on the molar mass of the monomer; M_w = 40,000 g mol^{-1}) were dissolved in 320 mL water and heated to 90 °C. Then, 4 g $AgNO_3$ (23.55 mmol) dissolved in 8 mL water was quickly added. Prior to addition, the silver nitrate solution was kept under light exclusion. The

dispersion was kept at 90 °C for different times (up to 7,000 min) and then allowed to cool to room temperature. The system was heated to 90 °C in a silicon oil bath under ambient light exposure. The synthesis was carried out in a round bottom flask with reflux condenser (water cooling). To determine the role of light exposure, the synthesis under reflux was also carried out under completely dark conditions, *i.e.* protected from irradiation during the whole reaction process. All syntheses were carried out under continuous vigorous stirring. Aliquots of the reaction mixtures were taken after selected time periods. At each point, a 10 mL aliquot of solution was taken with a syringe. The particles were collected and separated from by-products of synthesis by ultracentrifugation (29,400 g; 20,000 rpm; 30 min), redispersed in pure water and collected again by ultracentrifugation. This procedure was repeated three times. Thereby nitrate, excess glucose and its oxidation products, excess PVP, and excess silver ions were removed. After the third cycle, the sample was redispersed in 10 mL of distilled water. All samples were stored at 4 °C in the dark until further analysis.

4.2 Synthesis of silver chloride nanoparticles

4.2.1 Synthesis of PVP-coated silver chloride nanoparticles

PVP-coated silver chloride nanoparticles were synthesized by precipitation from aqueous solutions of sodium chloride and silver nitrate in the presence of PVP.[67] Here, 45 mg sodium chloride (0.77 mmol) and 54 mg PVP (0.98 µmol based on the molar mass of the monomer; M_w = 55,000 g mol^{-1}) were dissolved in 12 mL water and heated to 60 °C in a silicon oil bath under ambient light exposure for 30 min. Then, 57 mg $AgNO_3$ (0.36 mmol) dissolved in 1 mL water was quickly added. Prior to addition, the silver nitrate solution was kept under light exclusion. The dispersion was stirred at 60 °C for 30 min. The particles were collected by ultracentrifugation (28,600 g; 13,000 rpm; 15 min), redispersed in pure water and collected again by ultracentrifugation. The silver chloride nanoparticles were then redispersed in water by ultrasonication. In that way, excess PVP and excess silver ions were removed. All samples were stored at 4 °C in the dark until further analysis. The nanoparticles were characterized by scanning electron microscopy, energy-dispersive X-ray

spectroscopy, dynamic light scattering, and nanoparticle tracking analysis. The final silver concentration in all dispersions was determined by atomic absorption spectroscopy.

4.2.2 Synthesis of fluorescent silver chloride nanoparticles

Poly(ethyleneimine) (PEI)-coated silver chloride nanoparticles were synthesized by precipitation from aqueous solutions of sodium chloride and silver nitrate in the presence of PEI by simultaneously pumping aqueous solutions of sodium chloride (30 mg mL^{-1}; 0.51 mol L^{-1}) and silver nitrate (25 mg mL^{-1}; 0.15 mol L^{-1}) in a volume ratio of 1 mL:1 mL into a stirred glass vessel containing 5 mL of PEI solution (2 mg mL^{-1}; 0.08 mmol L^{-1} based on the molar mass of the monomer; M_w = 25,000 g mol^{-1}) for 1 min and then stirring for 10 min. Then, 50 µL of a solution of fluorescein in ethanol (20 mg mL^{-1}; 0.06 mol L^{-1}) was added as a dye. The dispersion was stirred at room temperature for 120 min. The particles were collected by ultracentrifugation (29,400 g; 20,000 rpm; 15 min), redispersed in pure water and collected again by ultracentrifugation. The excess PEI, dye and excess silver ions were removed. The silver chloride nanoparticles were then redispersed in water by ultrasonication. All samples were stored at 4 °C in the dark until further analysis. The nanoparticles were characterized by scanning electron microscopy, energy-dispersive X-ray spectroscopy, dynamic light scattering, and nanoparticle tracking analysis. The final silver concentration in all dispersions was determined by atomic absorption spectroscopy. Dye concentration was determined by UV/Vis spectroscopy.

4.3 Synthesis of fluorescent barium sulfate particles

4.3.1 Synthesis of fluorescent barium sulfate microparticles

Fluorescent barium sulfate microparticles were synthesized by precipitation from aqueous solutions of barium hydroxide and sodium sulfate in the presence of carboxymethylcellulose conjugated with 6-aminofluorescein (CMC-F) by simultaneously pumping aqueous solutions of barium hydroxide (100 mmol L^{-1}) and sodium sulfate (100 mmol L^{-1}) in a volume ratio of 12 mL:12 mL into a stirred glass

vessel containing 25 mL of CMC-F solution (2 g L^{-1}; 0.02 mmol L^{-1} based on the molar mass of the monomer; M_w = 90,000 g mol^{-1}) for 0.5 min and then stirring for 10 min. The particles were collected and separated from synthesis by-products by ultracentrifugation (1,250 g; 3,000 rpm; 30 min), redispersed in pure water and collected again by ultracentrifugation. The barium sulfate microparticles were then redispersed in water by ultrasonication. All samples were stored at 4 °C in the dark until further analysis. The particles were characterized by scanning electron microscopy, energy-dispersive X-ray spectroscopy, dynamic light scattering, thermogravimetry, and X-ray powder diffraction.

4.3.2 Synthesis of fluorescent barium sulfate sub-microparticles

Fluorescent barium sulfate sub-microparticles were synthesized by precipitation from aqueous solutions of barium hydroxide and sodium sulfate in the presence of carboxymethylcellulose conjugated with 6-aminofluorescein by simultaneously pumping aqueous solutions of barium hydroxide (100 mmol L^{-1}) and sodium sulfate (100 mmol L^{-1}) via Y-connector in a volume ratio of 12 mL:12 mL into a stirred glass vessel containing 25 mL of CMC-F solution (2 g L^{-1}; 0.02 mmol L^{-1} based on the molar mass of the monomer; M_w = 90,000 g mol^{-1}) for 0.5 min and then stirring for 10 min. The particles were collected by centrifugation (1,250 g; 3,000 rpm; 30 min), redispersed in pure water and collected again by centrifugation. The barium sulfate sub-microparticles were then redispersed in water by ultrasonication. All samples were stored at 4 °C in the dark until further analysis. The particles were characterized by scanning electron microscopy, energy-dispersive X-ray spectroscopy, dynamic light scattering, thermogravimetry, and X-ray powder diffraction.

4.3.3 Synthesis of fluorescent barium sulfate nanoparticles

Fluorescent barium sulfate nanoparticles were synthesized by precipitation from solutions of barium chloride and sodium sulfate in the presence of carboxymethylcellulose conjugated with 6-aminofluorescein. Here, 1 mL of sodium sulfate solution (50 mmol L^{-1}; ethanol:water = 1:1 v/v%) was pumped into a stirred

glass vessel containing 25 mL of barium chloride-CMC-F solution (50 mmol L^{-1} $BaCl_2$; 2 g L^{-1} CMC-F (0.02 mmol L^{-1} based on the molar mass of the monomer; M_w = 90,000 g mol^{-1})) for 4 min and stirred for 10 min. The particles were collected by ultracentrifugation (29,400 g; 20,000 rpm; 30 min), redispersed in pure water and collected again by ultracentrifugation. The barium sulfate nanoparticles were then redispersed in water by ultrasonication. All samples were stored at 4 °C in the dark until further analysis. The particles were characterized by scanning electron microscopy, energy-dispersive X-ray spectroscopy, dynamic light scattering, thermogravimetry and X-ray diffraction.

4.4 Experiments with silver compounds in biological media

4.4.1 Precipitation experiments with silver nitrate in biological media

Silver nitrate was added to different biological media (physiological salt solution, glucose solution, phosphate-buffered saline, Lysogeny Broth, Roswell Park Memorial Institute medium) with silver ion concentrations between 0.01 g L^{-1} and 0.1 g L^{-1} (10 to 100 ppm). This is the range for the cytotoxicity of silver.[11, 31, 68-70] The solutions of silver nitrate were stirred at room temperature for 7 days under sterile conditions. Light was not explicitly excluded. All precipitates were isolated by ultracentrifugation (29,400 g; 20,000 rpm; 30 min), redispersed in pure water, again subjected to ultracentrifugation and then analyzed by X-ray powder diffraction, scanning electron microscopy, and energy-dispersive X-ray spectroscopy.

4.4.2 Immersion experiments with silver nanoparticles in biological media

Silver nanoparticles were added to biological media (physiological salt solution, glucose solution, phosphate-buffered saline, Lysogeny Broth, Roswell Park Memorial Institute medium) with silver concentrations between 0.01 g L^{-1} and 0.1 g L^{-1} (10 to 100 ppm). The particle synthesis was described in Chapter 4.1. The dispersions of silver nanoparticles in different media were stirred at room temperature for 7 days under sterile conditions. Light was not explicitly excluded. The nanoparticles and all precipitates were isolated by ultracentrifugation (29,400 g; 20,000; 30 min),

redispersed in pure water, again subjected to ultracentrifugation, and then analyzed by X-ray powder diffraction, scanning electron microscopy, and energy-dispersive X-ray spectroscopy.

4.5 Quantification of dissolved species of silver compounds in biological media

4.5.1 Determination of silver nanoparticle dissolution in DMEM supplemented with 10% FCS by atomic absorption spectroscopy

Silver nanoparticles were added to Dulbecco's modified Eagle's medium (DMEM) supplemented with 10% fetal calf serum (FCS) with silver concentration 0.05 g L^{-1} (50 ppm). The dispersions of silver nanoparticles in medium were incubated at 37 °C with gentle shaking for various periods of time under sterile conditions. After incubation, the samples were ultracentrifuged (77,000 g; 35,000 rpm; 30 min) and then the supernatant was pipetted off as much as possible, without removing any residue. Then, 2 mL of supernatant was collected for analysis with 2 mL NH_3 and 2 mL H_2O. The residue was washed three times with ultrapure water by repeated ultracentrifugation (77,000 g; 35,000 rpm; 30 min). Then the residue was treated with 1 mL of concentrated HNO_3 and 4 mL ultrapure water, shaken well and centrifuged (1,250 g; 4,000 rpm; 60 min). The supernatant filled in the flask to 10 mL with ultrapure water. The new residue was treated with 1 mL of H_2O and 2 mL NH_3, also shaken well, and filled in the flask to 10 mL with ultrapure water. For all samples, duplicate procedures were performed and the values were averaged after analysis. From incubation until the last step, the samples were treated in their own thick-walled 10 mL centrifuge tubes to avoid losses. The silver concentration in all dispersions was determined by atomic absorption spectroscopy. A schematic representation of the protocol for quantification of silver nanoparticle dissolution is shown in Figure 6.

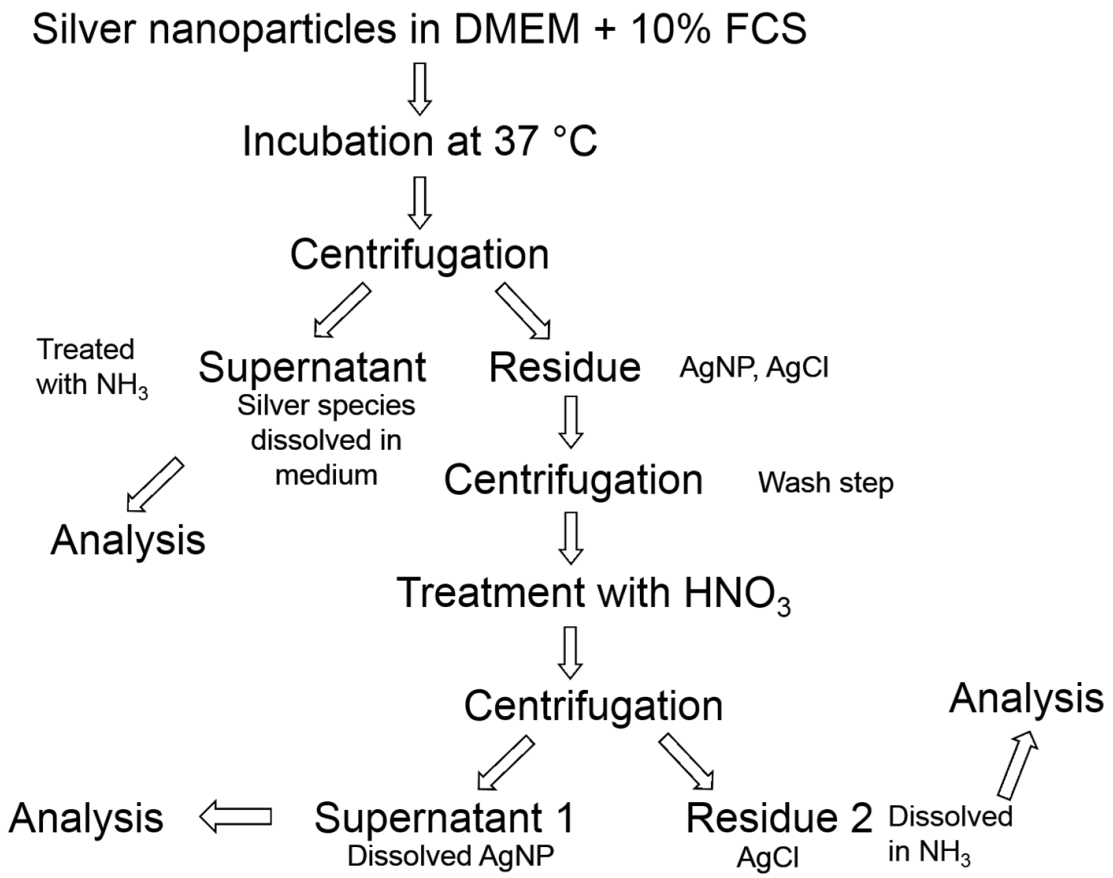

Figure 6: Schematic representation of the protocol for the quantification of silver nanoparticle dissolution.

4.5.2 Determination of silver chloride nanoparticle dissolution in biological media

Silver chloride nanoparticles were added to DMEM, DMEM medium supplemented with 10% FCS, 10% FCS solution and phosphate-buffered saline (PBS) with silver concentrations of 0.005 g L^{-1} and 0.1 g L^{-1} (5 ppm and 100 ppm). The dispersions of silver chloride nanoparticles in medium were incubated at 37 °C with gentle shaking for 24 h under sterile conditions. After incubation, the samples were ultracentrifuged (66,000 g; 30,000 rpm; 30 min) to separate dissolved silver species from remaining silver chloride nanoparticles. Then, 1 mL of supernatant was collected for analysis with

2 mL NH_3 and 7 mL H_2O. The silver concentration in all dispersions was determined by atomic absorption spectroscopy.

4.5.3 Determination of silver nitrate solubility in biological media

Silver nitrate solution was added to DMEM, DMEM medium supplemented with 10% FCS, 10% FCS solution and PBS with silver concentration 0.005 g L^{-1} and 0.1 g L^{-1} (5 ppm and 100 ppm). The dispersions of silver nitrate in biological medium were incubated at 37 °C with gentle shaking for 24 h under sterile conditions. After incubation, the samples were ultracentrifuged (66,000 g; 30,000 rpm; 30 min) to separate dissolved silver species. 1 mL of supernatant was collected for analysis with 2 mL NH_3 and 7 mL H_2O. The silver concentration in all dispersions was determined by atomic absorption spectroscopy.

4.6 Biological experiments

4.6.1 Eukaryotic cell culture experiments

4.6.1.1 Human mesenchymal stem cells

Human mesenchymal stem cells (hMSCs, 3rd to 7th passage, Lonza, Walkersville Inc., MD, USA) were cultured in cell culture medium RPMI + 10% FCS using 24-well cell culture plates (Falcon, Becton Dickinson GmbH, Heidelberg, Germany). Cells were maintained at 37 °C in a humidified atmosphere with 5% CO_2. hMSCs were sub-cultivated every 7-14 days, depending on the cell proliferation rate. Adherent cells were washed with PBS solution (GIBCO, Life Technologies) and detached from the culture flasks by addition of 0.2 mL cm^{-2} 0.25% trypsin/0.1% ethylenediamine tetraacetic acid (EDTA, Sigma-Aldrich, Taufkirchen, Germany) for 5 min at 37 °C. Then the hMSCs were collected and washed twice with RPMI + 10% FCS.

Cell cultivation was performed by Jun.-Prof. Dr. Christina Sengstock.

4.6.1.2 Viability of hMSCs treated with silver chloride nanoparticles in correlation with fetal calf serum in medium

For the viability experiment, $1.5 \cdot 10^4$ hMSCs mL^{-1} were cultured in RPMI 1640 containing 10% FCS using a 24-well cell culture plate (Falcon, Becton Dickinson GmbH, Heidelberg, Germany) for 24 h. Afterwards, the hMSCs were cultured in cell culture medium RPMI 1640 with or without 10% FCS, in the presence or absence of 5.0, 2.5, 2.0, 1.0, and 0.5 µg mL^{-1} silver chloride nanoparticles for 24 h under cell culture conditions. The working solutions were prepared by serial dilutions of a PVP-coated AgCl nanoparticle stock solution with sterile ultrapure water. The viability and morphology of the incubated hMSCs were analyzed using calcein-acetoxymethylester (calcein-AM, Calbiochem, Schwalbach, Germany) fluorescence staining. After incubation for 24 h, the nanoparticle-treated and silver ion-treated cells were washed twice with RPMI and incubated with calcein-AM (1 mM) at 37 °C for 30 min under cell culture conditions. Then, the adherent cells were washed again with RPMI and analyzed by fluorescence microscopy (Olympus MVX10, Olympus, Hamburg, Germany). Fluorescence microphotographs were taken (Cell P, Olympus) and digitally processed using Adobe Photoshop® 7.0. The cell morphology was analyzed by phase contrast microscopy (Olympus CK 2) and documented by microphotography (Camedia C3030, Olympus). In this method, living cells emit green fluorescence.

Cell cultivation and viability assay were performed by Jun.-Prof. Dr. Christina Sengstock.

4.6.1.3 Peripheral blood mononuclear cells

Peripheral blood mononuclear cells (PBMC) were isolated by a single-step procedure that was based on a discontinuous double-Ficoll gradient described by English and Andersen.[71] Briefly, EDTA-anticoagulated peripheral blood (9 mL, Monovette®, Sarstedt, Nürnbrecht, Germany), obtained from healthy volunteers (covered by the approval of the local ethics committee), was diluted with an equal volume of 0.9% aqueous NaCl and carefully overlaid on a double gradient formed by layering 10 mL of

aqueous polysucrose/sodium diatrizoate, adjusted to a density of 1.077 g mL^{-1} (Histopaque 1077, Sigma-Aldrich, Taufkirchen, Germany), on 10 mL Histopaque 1119 (Sigma-Aldrich) in 50 mL Falcon tubes (BD-Biosciences, Heidelberg, Germany). The tubes were centrifuged at 700 g for 30 min at room temperature. After centrifugation, two distinct leukocyte cell layers (PBMC and polymorphonuclear neutrophil granulocytes (PMN)) were obtained above the bottom sediment of erythrocytes. The PBMC layer was carefully aspirated and transferred to a separate 50 mL tube, and the tube was filled with PBS (Sigma-Aldrich) and centrifuged at 200 g for 15 min at 4 °C. This method led to more than 95% pure and viable PBMC. Cell counting was performed using Tuerk staining solution (Sigma-Aldrich). The isolated cells were adjusted to $1 \cdot 10^6$ cells mL^{-1} in RPMI 1640 (GIBCO, Invitrogen GmbH, Karlsruhe, Germany), cell culture medium supplemented with L-glutamine (0.3 g L^{-1}), sodium bicarbonate (2.0 g L^{-1}), 10% FCS (GIBCO, Invitrogen GmbH), and 20 mM N- (2- hydroxyethyl)-piperazine-N´-(2-ethanesulfonic acid) (HEPES, Sigma-Aldrich). For the differentiation of monocytes and T-cells in the PBMC-fraction, the cells were centrifuged at 370 g for 5 min at room temperature. The supernatants were discarded, and the pellets were carefully resuspended. Fluorochrome-labelled anti-CD3 and anti-CD14 (BD Bioscience, Heidelberg, Germany) were added (20 µL each), and the samples were incubated for 30 min in the dark at room temperature. Then the cells were washed with PBS, centrifuged at 370 g for 5 min at room temperature, and fixed with 1.5% formaldehyde.

Cell cultivation and viability assay were performed by Jun.-Prof. Dr. Christina Sengstock.

4.6.1.4 Uptake of silver chloride nanoparticles by HeLa cells

HeLa cells were cultivated in DMEM, supplemented with 10% FCS at 37 °C in a humidified atmosphere with 5% CO_2. Approximately 12 h prior to the addition of the silver compounds, the cells were seeded into a six-well plate over cover glass. The silver concentration in cell culture medium was 2 µg mL^{-1} (2 ppm). The cells were

incubated for 4 h under cell culture conditions, then washed three times with PBS, and studied under a fluorescence microscope BZ-9000 (Keyence, Japan).

Cell cultivation and uptake experiments were performed by Dr. Svitlana Chernousova.

4.6.1.5 NR8383 cells

Rat alveolar macrophages NR8383 were purchased from ATCC via LGC Standards GmbH (Wesel, Germany) and cultivated at 37 °C, 100% humidity and 5% CO_2 in Ham's F12 + 15% FCS (Biochrom KG, Berlin, Germany), 2 mM L-glutamine, 100 µg mL^{-1} penicillin, and 100 µg mL^{-1} streptomycin. Approximately $1.2 \cdot 10^6$ cells were seeded in 2.5 mL medium each.

4.6.1.5.1 Determination of cellular $BaSO_4$ particle uptake by laser scanning microscopy

Laser scanning microscopy was performed to demonstrate the occurrence of intracellular $BaSO_4$ particles in NR8383 cells after incubation. Therefore, NR8383 cells were subconfluently grown on 2-well Lab-TekTM glass chamber slides (Thermo Fisher Scientific, Langenselbold, Germany) and subsequently washed and exposed to 50 µg mL^{-1} $BaSO_4$ particles for 24 h under cell culture conditions. After this incubation, cells were labeled with specific cell organelle fluorescent probes (Life Technologies). As a marker for late endosomes and lysosomes, the cells were incubated with 50 nM Lyso Tracker Red DND 99 in pure RPMI 1640 for 30 min at 37 °C. For labelling of the cell nucleus, the cells were incubated with 162 µM Hoechst33342 in pure RPMI 1640 for 5 min at 37 °C. After three rinses in RPMI 1640, the cells were mounted on glass chamber slides. Images were taken using a 40x oil immersion objective in a laser scanning microscope (LSM 700; Zeiss) and Zeiss 2010 software.

Laser scanning microscopy studies were performed by Dr. Isabell Schremmer and Jun.- Prof. Dr. Christina Sengstock.

4.6.1.5.2 Particle-induced cell migration assay

Prior to the test, the trans-retinal differentiated human leukemia cells (dHL-60) were starved by culturing without FCS overnight. For this, 200,000 of these dHL-60 cells were added to 200 µL RPMI without FCS and seeded in each plate well insert (THINCERT, 3 µm pore size, Greiner bio-one, Frickenhausen, Germany) of the "Boyden Chamber". The inserts were placed on 24 black well plates (Krystal, Duna Labortechnik, Asbach, Germany). The wells contained 500 µL supernatants of the challenged NR8383 cells. The dHL-60 cells were allowed to migrate across the membrane at 37 °C, 100% humidity and 5% CO_2 for 20 h. Four plate wells were left without inserts and served for calibration. For this purpose, up to 200,000 dHL-60 cells were seeded directly into the plate wells.

The migrated cells were stained by adding 500 µL calcein-AM (>90% HPLC, Sigma-Aldrich) (4 µM in PBS) into the plate wells. Calcein-AM was delivered as 4 mM solution in DMSO. The solution was stored in aliquots at -18 °C. Prior to use, 12.5 µL of this solution was diluted in 12.5 mL PBS to yield a final concentration of 4 µM. The samples were incubated for another 60 min at 37 °C and 5% CO_2. Following staining, the cell suspensions were removed from the plate wells and collected by centrifugation at 400 g for 5 min at room temperature. Here, 850 µL of the supernatant was discarded and the pellet was resuspended in the remaining 150 µL. In parallel, adherent cells were detached from the outside of the inserts by incubating the inserts in the plate wells with 500 µL trypsin/EDTA (0.05%/0.02%, Biochrom KG, Berlin, Germany). Incubation was performed for 10 min at 37 °C and 5% CO_2 and the inserts were removed from the plate wells. Finally, the 150 µL samples of the collected cells were added to the detached cells in the plate wells. Fluorescence was measured at 490/520 nm (SpectraMax M3, Molecular Devices, Sunnyvale, USA). Before each measurement, the plates were vigorously shaken by the shaker which is integrated in the fluorescent photometer.

Particle induced cell migration assay was performed by Dr. Isabell Schremmer.

4.6.2 Bacterial culture experiments

4.6.2.1 Staphylococcus aureus

Bacterial tests were performed with *Staphylococcus aureus* (DSMZ 1104), obtained from the DSMZ (German Collection of Microorganisms and Cell Cultures). *S. aureus* was grown in BHI broth (brain-heart infusion broth, bioMérieux, Nürtingen, Germany) overnight at 37 °C in a water bath. Bacterial concentrations of overnight cultures were measured using a Densichek® (bioMérieux, Lyon, France) turbidity photometer. The calculation of bacterial counts was based on turbidity standard solutions (McFarland scale). The antimicrobial activity of nanoparticulate silver chloride was tested using standard methods which determine the minimum inhibitory concentration (MIC) and the minimum bactericidal concentration (MBC). MIC was determined in RPMI 1640 (Life Technologies) containing 10% FCS (Life Technologies) and L-glutamine (0.3 g L^{-1}, Life Technologies), and defined as the lowest silver concentration able to inhibit bacterial growth (no visible growth) in 2 mL plastic macrodilution test tubes. Therefore, working silver stock solutions (50 µL) were added to 1 mL of the respective liquid culture medium, and different cell numbers (10^3 to 10^6 mL^{-1}) of bacteria were used for inoculation. Cells were incubated in a cell culture incubator (RPMI + 10% FCS) in the presence of 5% carbon dioxide in a humidified atmosphere at 37 °C overnight. The minimum bactericidal concentration (MBC) was subsequently determined by plating 100 µL aliquots of the MIC samples on blood agar plates. The MBC was defined as the lowest silver concentration which completely prevented colony forming units (CFU) on the agar plate.

Antimicrobial tests were performed by Jun.-Prof. Dr. Christina Sengstock.

5 Results and discussions

5.1 Characterization of silver nanoparticles

Silver nanoparticles were synthesized with glucose in the presence of poly(vinylpyrrolidone) according to Wang *et al.*[66] Particles were characterized using scanning electron microscopy and dynamic light scattering. All measurements were performed with the purified nanoparticles. The size analysis by dynamic light scattering is shown in Figure 7. The measurement was carried out in a disposable polystyrene cuvette of dilute aqueous dispersion.

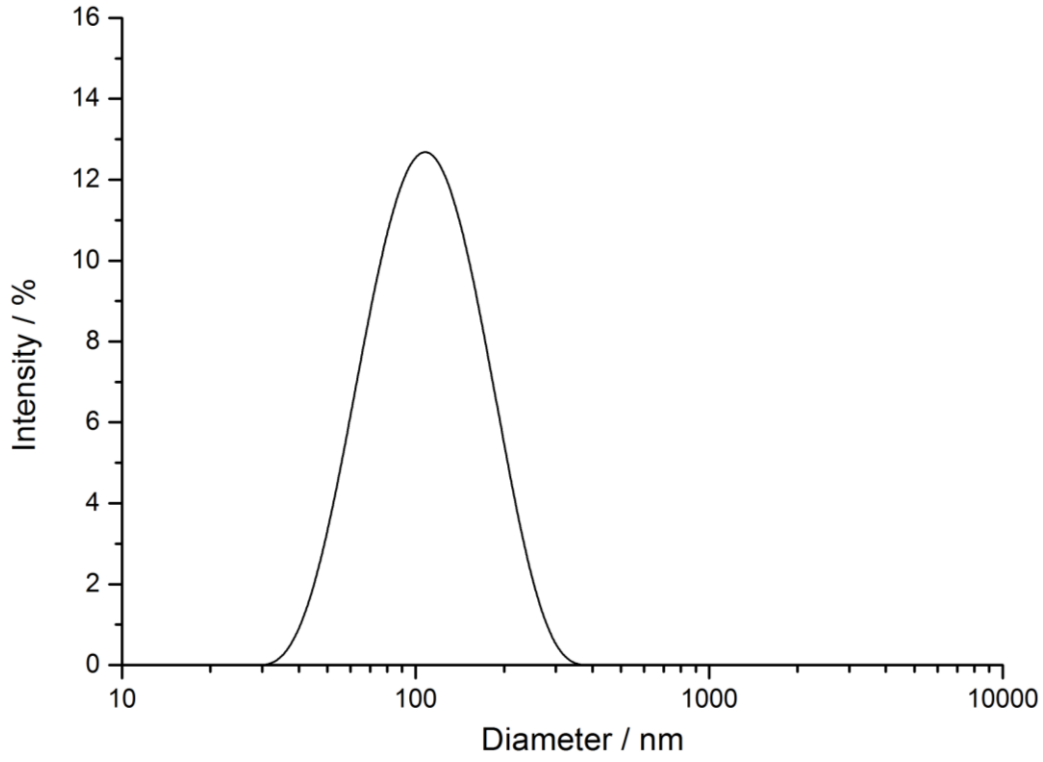

Figure 7: Particle size distribution of PVP-coated silver nanoparticles as measured by dynamic light scattering.

The hydrodynamic diameter as measured by dynamic light scattering pattern was about 120 nm. The hydrodynamic diameter gives information about the metal core and

outer ligand shell, which may consist of adsorbed PVP in our case. The polydispersity index (PDI) was lower than 0.3 in all cases. It is typical for a well-dispersed system.

The zeta potential distribution is shown in Figure 8. The particles were negatively charged with the zeta potential of -20 mV. This means that PVP-coated silver nanoparticles were electrosterically stabilized, because PVP molecules provide colloidal stability of particles by steric repulsion.

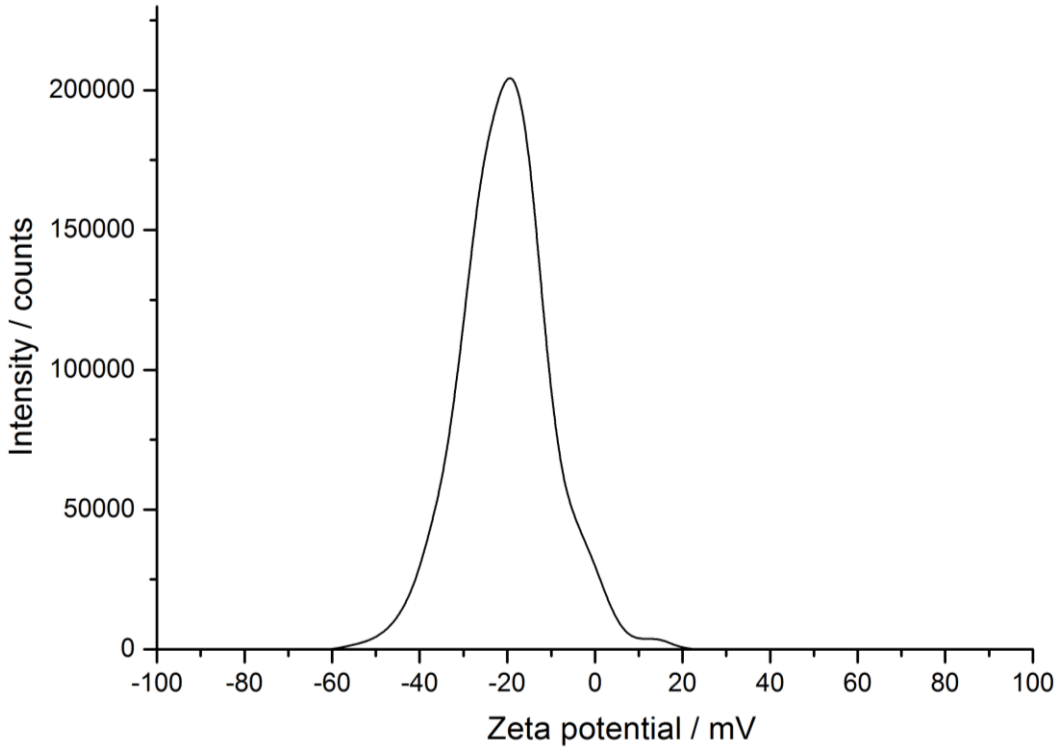

Figure 8: Zeta potential of PVP-coated silver nanoparticles.

Figure 9 shows a typical SEM image of the synthesized silver nanoparticles. For preparation, the diluted dispersion of purified silver nanoparticles was dried on a silicon wafer. Figure 9 depicts particles with prevalent spherical morphology with a minor presence of polygones. The particles were well distributed on the substrate and show no strong agglomeration. The particle size distribution was performed by electron

microscopy and is displayed in Figure 10. The diameter of the metallic core was about 65 nm.

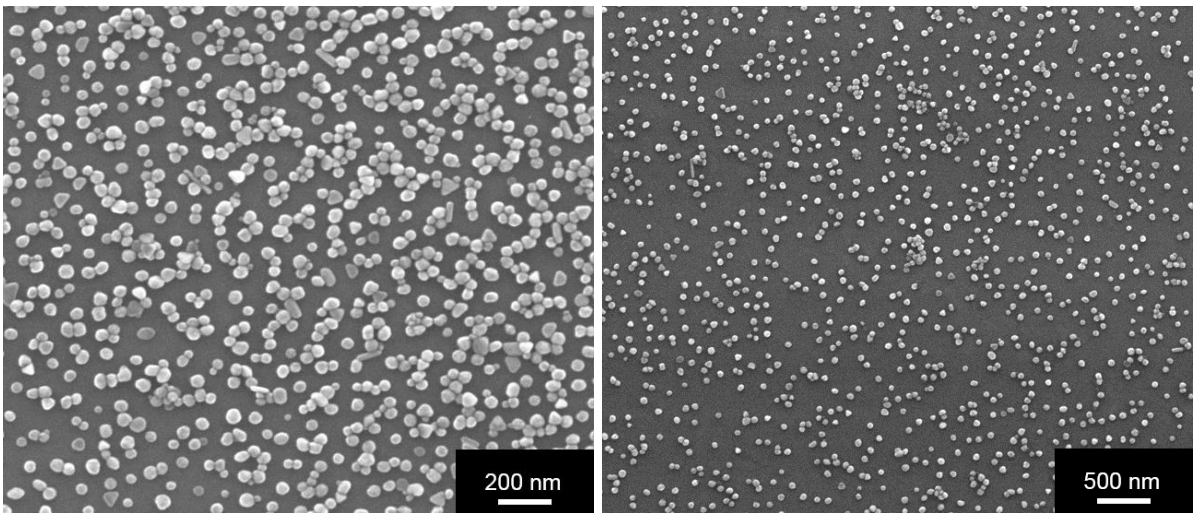

Figure 9: Scanning electron microscopy images of PVP-coated silver nanoparticles.

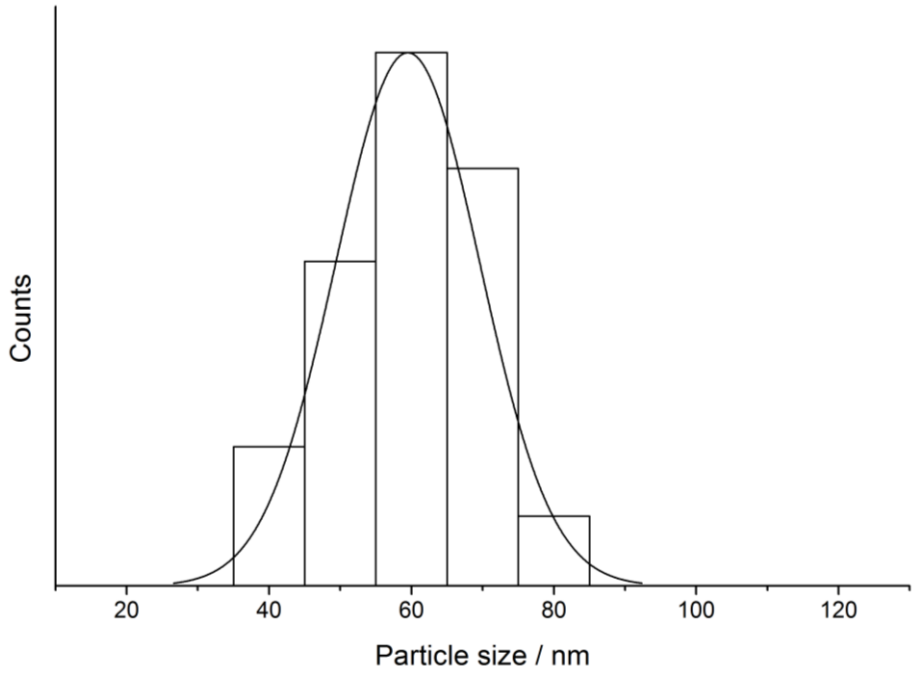

Figure 10: Particle size distribution of PVP-coated silver nanoparticles as measured by scanning electron microscopy.

Energy-dispersive X-ray spectroscopy confirmed the formation of silver nanoparticles (Figure 11). The dominant peak of silicon resulted from the substrate (silicon wafer). The carbon peak was due to the PVP polymer.

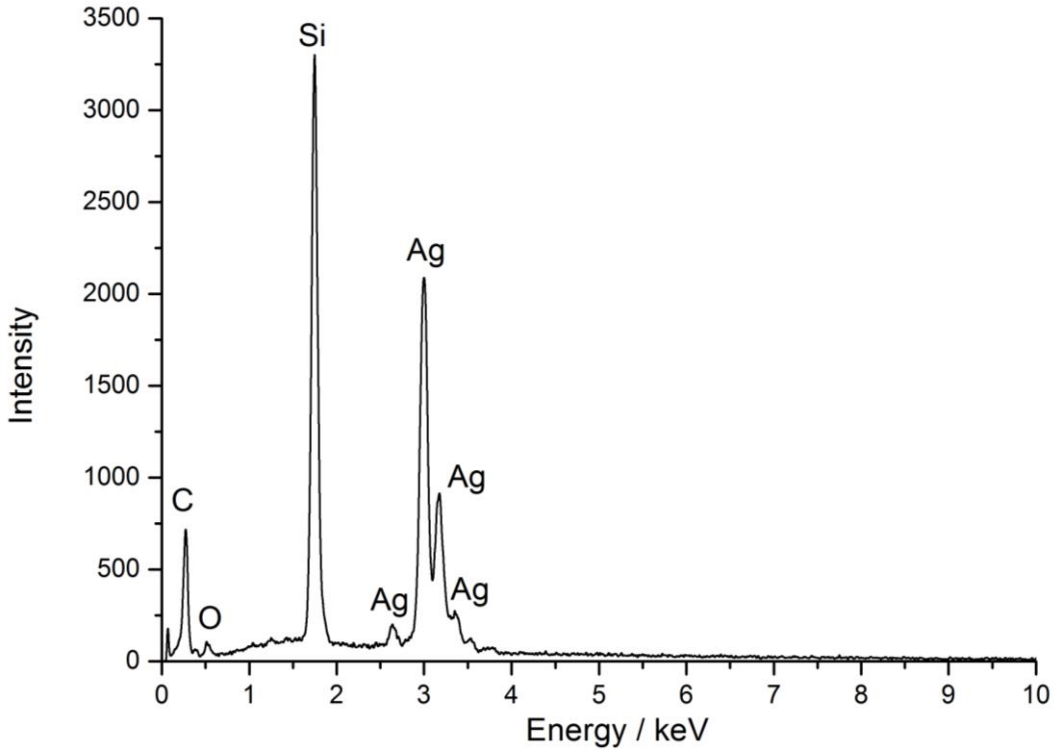

Figure 11: Energy-dispersive X-ray spectrum of PVP-coated silver nanoparticles.

In summary, the hydrodynamic diameter of PVP-coated silver nanoparticles was about 100 nm. The core diameter of synthesized particles was around 65 nm. Dynamic light scattering and scanning electron microscopy each probe different particle sizes. This can be explained by investigation of the same sample in non-comparable states. Electron microscopy gives information about the dried sample, while dynamic light scattering measurements were performed in dispersion. Another possible explanation is an overestimation of the scattered light proportion of larger particles and possible agglomerates.

In particular, PVP-coated silver nanoparticles were explicitly used for characterization of the physico-chemical properties (growth, dissolution, protein adsorption, dispersability) and the cellular consequences of exposure to a broad range of biological test systems.[31, 68, 69, 72-75] Moreover, in the described synthetic pathway, particles can be produced with high quality and in large quantities. This point is essential for biological experiments, because reliably-produced particles are required for a large number of experiments.[72]

Synthesized PVP-coated silver nanoparticles were used in this study for immersion experiments, evaluation of dissolution in cell culture media as well as for biological investigations.

5.2 Characterization of PVP-coated silver nanoparticles synthesized under the variation of light and air exposure

As described in the previous chapter, the synthesis of silver nanoparticles in the presence of poly(vinylpyrrolidone) (PVP) by reduction of silver ions with glucose offers a reliable quality and quantity of material for further investigations.[72] However, the presence of a small fraction of non-spherical particles (triangular plates) was observed. Morphological and colloidal characterization of silver nanoparticles demonstrates strong correlations between average particle size, shape, and dispersity and the observed tunable physico-chemical behavior of those particles.[76, 77]

The structure of silver nanoparticles was studied during the reduction of silver ions with glucose under the variety of light and air exposures. PVP was used as a capping agent. The structural and morphological properties of silver nanoparticles were studied extensively by electron microscopy and X-ray powder diffraction. For all kinds of measurements, only purified dispersions of silver nanoparticles were used. The washing step was consisted of ultracentrifugation and eventual sonication in pure water. After that, all of the samples were preserved in light exclusion conditions at 4 °C. The detailed procedure of synthesis was described in Chapter 4.1. Variations of in air (oxygen) and light exposure were selected to be studied, while the possible effects on silver particle formation were shown.[78]

As shown by scanning electron microscopy, the diameter of the nanoparticles increased monotonically during the synthesis. The particle size from SEM was obtained by image analysis to differentiate between particles of various morphology. Figure 12 shows the growth of the spherical silver nanoparticles during the synthesis.

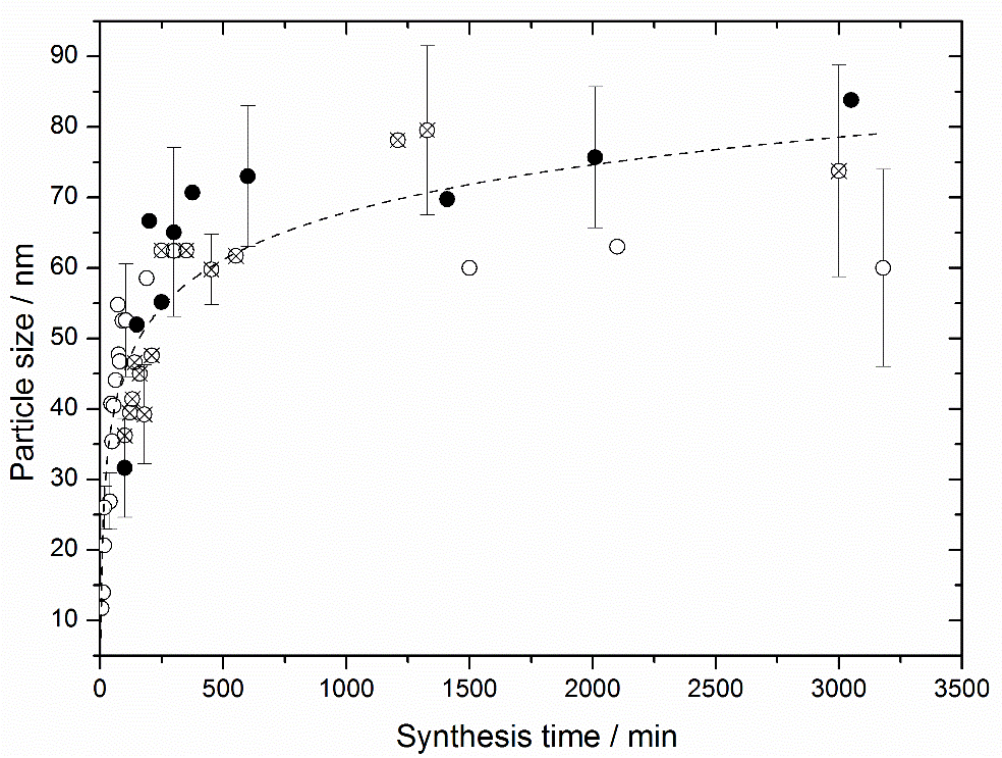

Figure 12: Growth of spherical silver nanoparticles over time as determined by scanning electron microscopy. Open circles: Synthesis in air; crossed circles: Synthesis under reflux and ambient light exposure; closed circles: Synthesis under reflux in the dark.

For the estimation of particle size, at least 200 individual spherical particles were analyzed. It is notable that the particles grew rapidly in diameter during the first 500 min and then remain at a practically constant size. There is no significant difference between the syntheses under variation of light or air exposure, although the deviation in particle diameters increases with extended reaction time. Figure 13 displays the particle size distribution of the spherical nanoparticles for different reaction times. In spite of the fact that the particle size distribution became broader with longer reaction times, the nucleation took place mainly at the beginning of the synthesis and was not continuous.

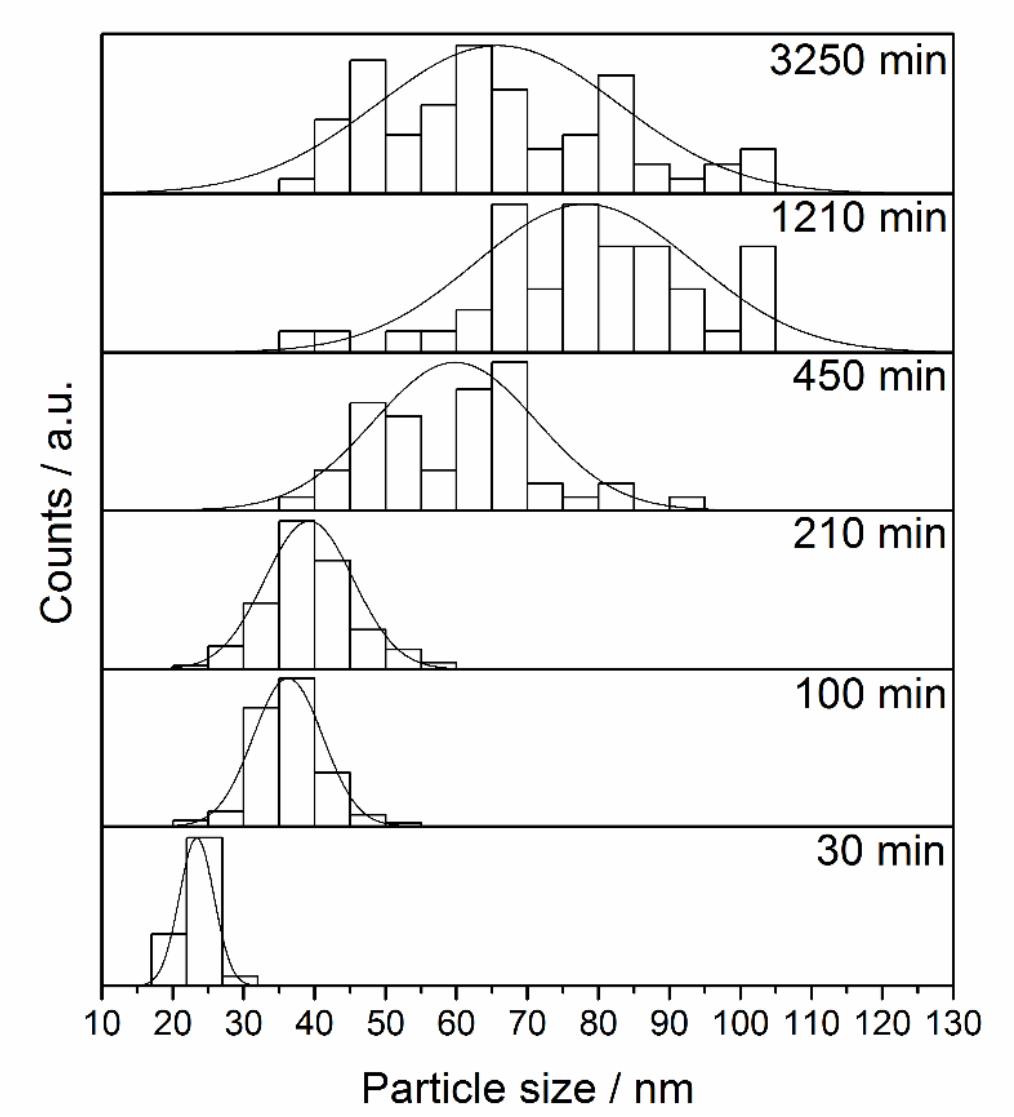

Figure 13: Particle size distribution of the spherical nanoparticles (as diameter) as a function of reaction time ($N \geq 200$).

Figure 14 shows representative scanning electron micrographs of silver nanoparticle samples after different time periods. The dispersions were dried in air, and a silicon wafer was used as a substrate. The diameter of the spherical particles increased with time. A closer look at the data indicated that triangular particles occurred first as a small fraction of the particle population but then strongly increased in number and also in size.

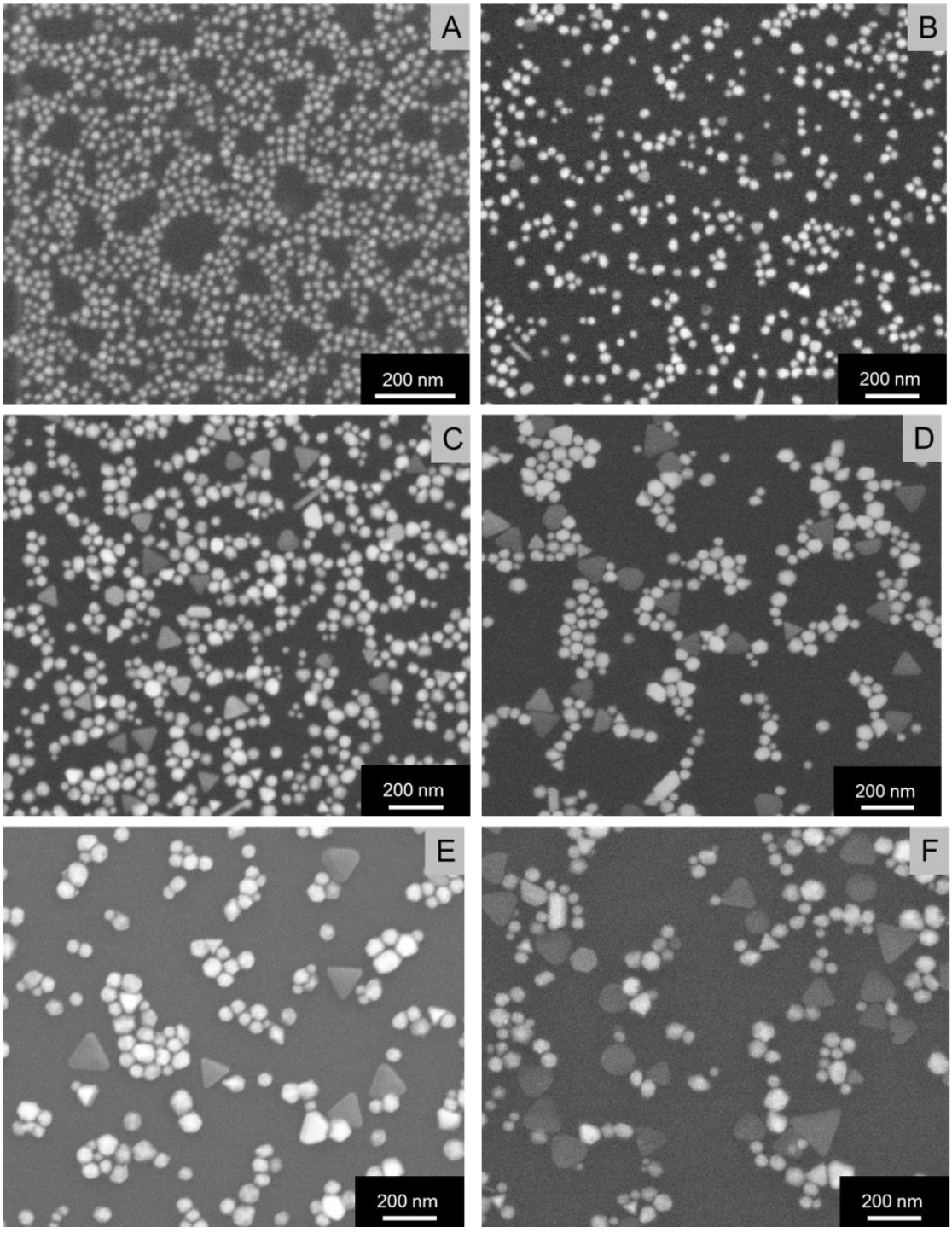

Figure 14: Representative SEM images of silver nanoparticles synthesized under reflux and ambient light exposure after 30 min (A), 100 min (B), 210 min (C), 450 min (D), 1210 min (E) and 3250 min (F).

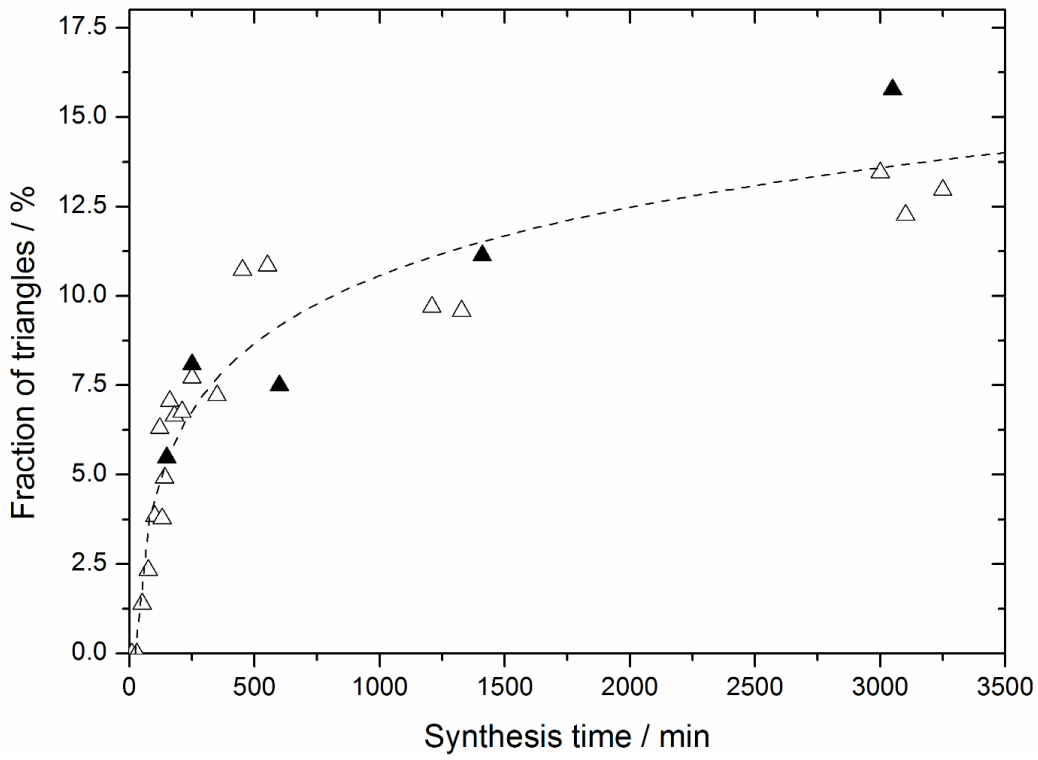

Figure 14: Fraction of triangles on all silver nanoparticles. Open triangles: Synthesis under reflux and ambient light exposure; closed triangles: Synthesis under reflux in the dark.

The fraction of triangles was computed by analyzing the number of particles (*N*>2,000). The increase in the fraction of triangles over the reaction time is shown in Figure 14. Furthermore, a very small fraction of silver triangles in the overall particle population could be observed even in the early stages of synthesis. The fraction of triangles increased rapidly during the first 500 min. After 3500 min, around 13% of particles were triangles. The presence or absence of light had no significant effect on the particle shape.

Scanning electron images show geometrically well-defined flat silver triangles. The triangle edge length also increased monotonically during the synthesis (Figure 15) to about 140 nm after 1000 min. At the same time, the spherical particles reached a diameter of only 65 nm. Similarly, light exposure was insignificant. However, spheres

and triangles originated from separate nucleation steps with different nucleation and growth kinetics. The thickness of the particles could neither be determined by SEM (because it was too small) nor by TEM (because it was impossible to orient the flat triangles perpendicular to the electron beam). In a similar study, *Zhang et al.* determined the thickness of silver nanoplates by atomic force microscopy (AFM) to be below 10 nm, which appeared to be realistic in our case as well.[79]

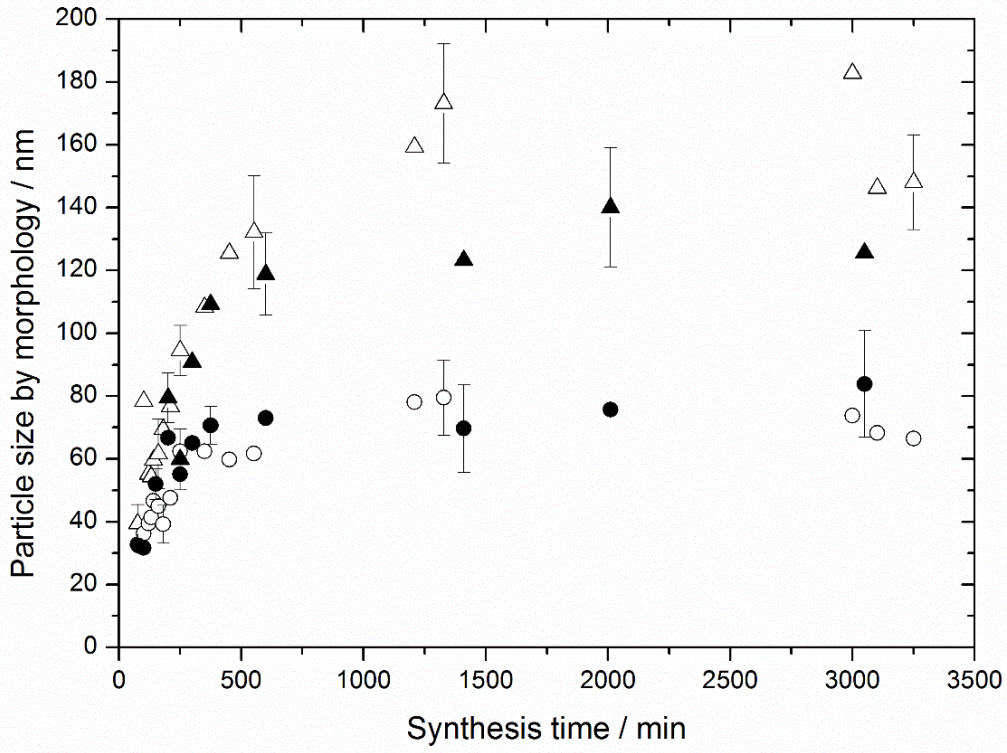

Figure 15: Particle size for different morphologies vs. time: spheres (maximum diameter) and triangles (edge length of a perfect triangle): Open circles: Spherical particles from the synthesis under reflux and ambient light exposure; open triangles: Triangular particles from the synthesis under reflux and ambient light exposure; closed circles: Spherical particles from the synthesis under reflux in the dark; closed triangles: Triangular particles from the synthesis under reflux in the dark.

The crystallographic properties of the nanoparticles were analyzed by X-ray powder diffraction. For an accurate determination of the unit cell parameter *a* of silver, a

nanoparticle sample was mixed with the LaB_6 standard before the diffraction experiment. LaB_6 is certified with respect to its lattice parameter and internal stress. Figure 16 shows a representative X-ray powder diffractogram with narrow peaks from LaB_6 and broad peaks from nanocrystalline silver. It was possible to determine the silver crystallite size to 24 nm and the silver unit cell parameter *a* with 4.0877(2) Å.

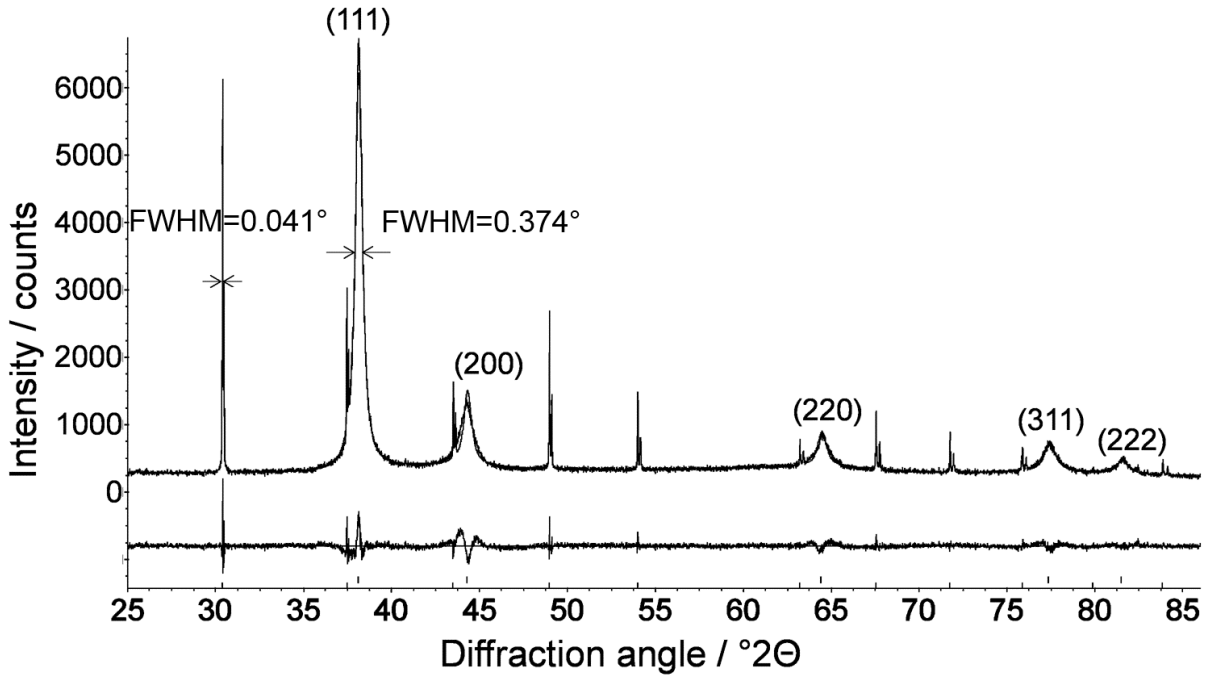

Figure 16: Representative X-ray powder diffractogram (with Rietveld refinement, R_{wp} = 6.6) of a mixture of silver nanoparticles with the microcrystalline standard LaB_6. Notably, in comparison with the narrow peaks of the LaB_6 standard, the peak width for the silver nanoparticles was considerably increased. The silver peaks are denoted by their lattice plane indices.

Figure 17 shows the unit cell parameter *a* of silver nanoparticles as a function of diameter. This was determined without the LaB_6 standard, therefore, the standard deviations were higher for the individual data points due to uncertainties of the measurement, *e.g.,* the sample displacement error.[80] Microcrystalline silver powder

was generated by sintering commercially available silver powder for 3 h at 700 °C to ensure microcrystallinity and the absence of a microstrain. For microcrystalline silver mixed with LaB_6, *a*=4.08635 Å was found, in good agreement with literature data (4.0862 Å[81] and 4.086 Å[82]). The lattice of the nanoparticles was significantly expanded in comparison to microcrystalline silver, but there is no significant variation in the unit cell parameter of nanoparticles as a function of their size, and also no influence of air or light exposure. *Fukuhara et al.* confirmed the lattice expansion of a unit cell in three kinds of nanoscale compound particles like MgO, α-Fe_2O_3 and TiC.[83]

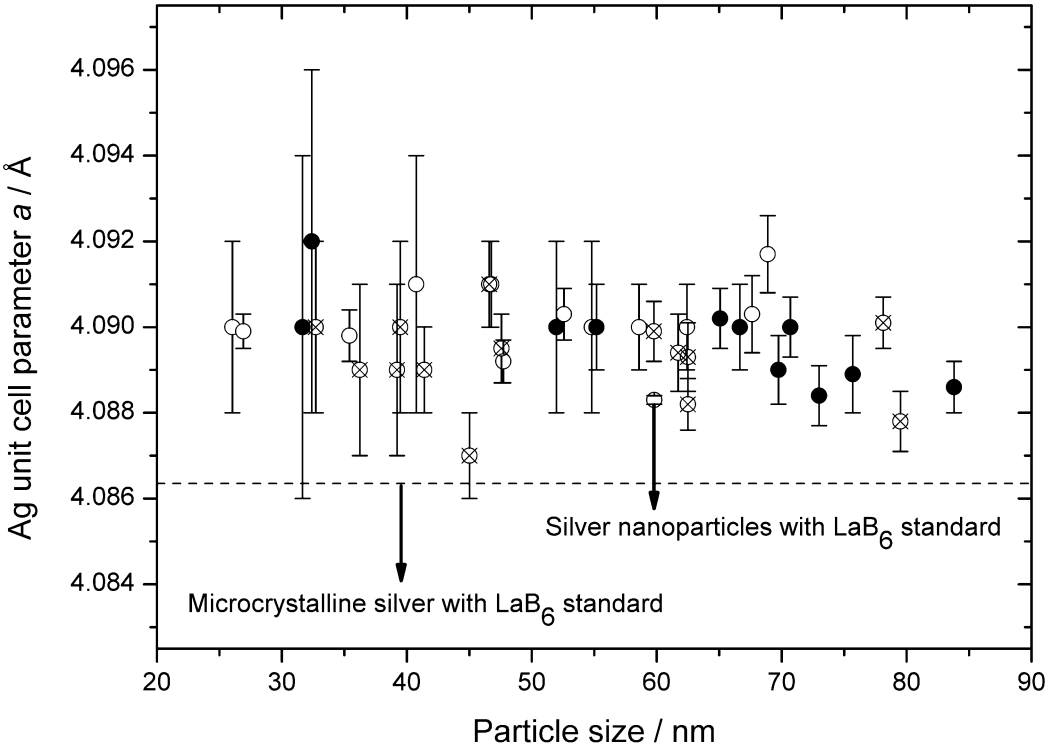

Figure 17: Unit cell parameter *a* vs. particle size as determined by dynamic light scattering including error bars. Open circles: Synthesis in air under ambient light exposure; crossed circles: Synthesis under reflux and ambient light exposure; closed circles: Synthesis under reflux in the dark. The circled value at 60 nm corresponds to a sample measured with the internal standard LaB_6. The dashed line corresponds to microcrystalline silver, measured with the internal standard LaB_6.

Rietveld analysis gave the crystallite size of the nanoparticles from X-ray diffraction peak broadening (Figure 16). The nanoparticle displayed a linear correlation (y=0.25x+3.5; R^2=0.86) between particle size and crystallite size. The Rietveld data were in excellent agreement with TEM data on the domain size (see below). This indicated that under these reducing conditions, the nucleation led to multiply twinned nanoparticles with domains that were of course smaller than the particle diameter. During the silver nanoparticle growth, the domains grew as well, but the domain structure of the nanoparticles remained unchanged. Otherwise, it would not be possible to observe a linear correlation between domain size and particle diameter. If secondary nucleation occurred, the domain size would increase more slowly than the particle diameter. Notably, there was again no effect of air or light exposure.

The Rietveld analysis averages out many particles without being able to differentiate between individual particles of different size and shape. However, as the spheres constituted the majority of the particle population and as they were rather uniform in size, it could be safely assumed that X-ray powder diffraction gave a reasonable approximation of the domain size of spherical particles.

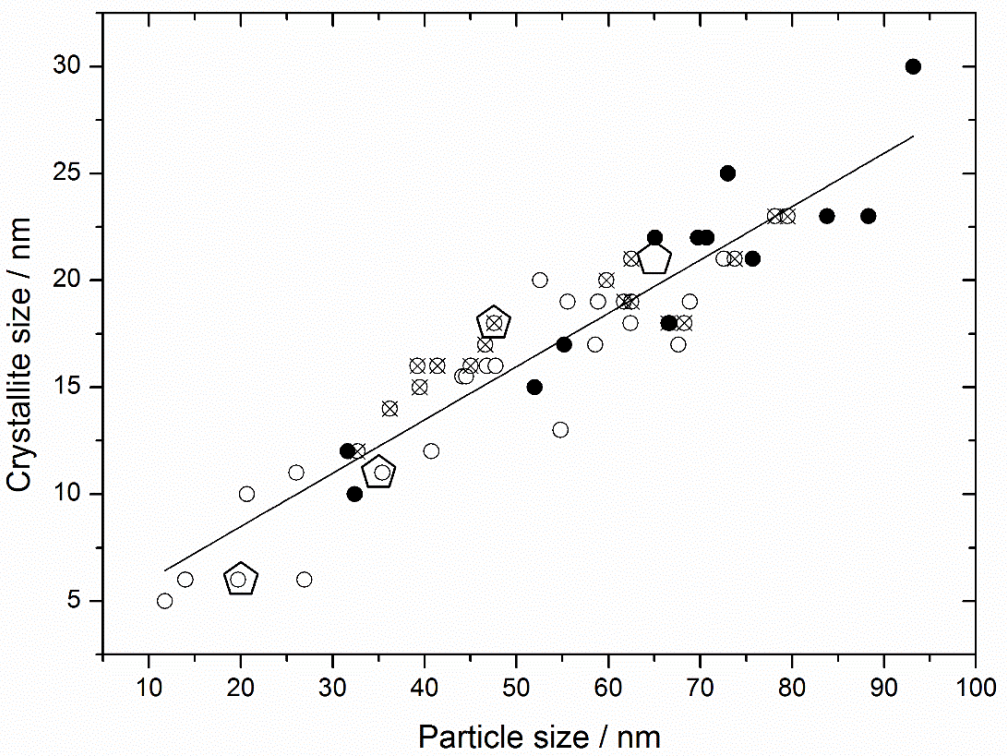

Figure 18: Crystallite size from X-ray powder diffraction vs. particle size from dynamic light scattering. Open circles: Synthesis in air under ambient light exposure; crossed circles: Synthesis under reflux and ambient light exposure; closed circles: Synthesis under reflux in the dark. The four open pentagons denote domain sizes as derived from TEM data (see Figure 19 A-D).

Further evidence came from transmission electron microscopy (TEM) of individual nanoparticles (Figure 19). This provided a direct measure of the domain size, as discernible from grain-boundaries between tetrahedra within the particle ultrastructure.[84] Measurements of the average domain size from TEM agreed well with the crystallite size calculated with the Rietveld method. In TEM, a five-fold symmetry of the domains was observed, indicating that the particles actually consist of pentagonal bipyramids. Within extended reaction time, triangular platelets and also few rod-like particles evolved. Both appeared to consist of only one crystallographic domain. This sharply contrasted with the spherical particles which are always twinned.

There were no non-twinned spherical particles observed, which indicates that twinning occurs very early during the nucleation.

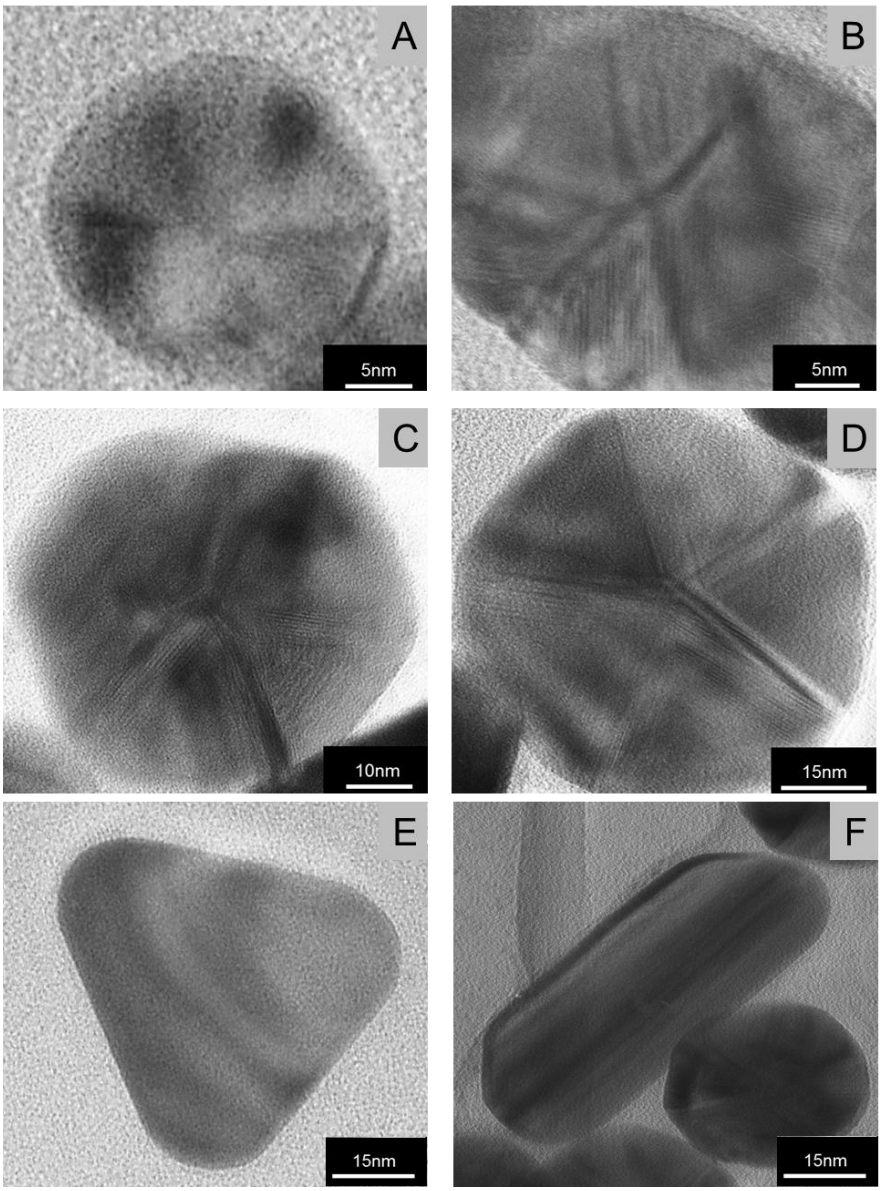

Figure 19: Representative TEM images of silver nanoparticles synthesized under reflux and ambient light exposure after 15 min (A; diameter 20 nm/domain size 6 nm), 42 min (B; 35 nm/11 nm); 65 min (C; 48 nm/18 nm); 350 min (D; 65 nm/21 nm). E shows a representative image of a triangular particle and F presents a representative image of a rod-like particle.

The effects of the reducing agent glucose and the capping agent PVP were not investigated in this study. However, these are standard synthetic conditions and reagents which often lead to nanoparticles with different sizes and shapes.[85-88] Our results showed that there were considerable dynamics in the system, up to about 1000 min reaction time. Nucleation appeared to occur in the early stages, with an imprint of the final morphology: sphere (in fact: pentagonal twin) or triangle. These initially formed nuclei (or seeds) grew with time by attracting more silver ions from the solution, but their internal crystallographic structure remained the same. The different growth rates of spheres and triangles had to be related to different kinetics of reduction of silver ions and subsequent attachment onto the silver particle surface.

For most wet-chemical synthesis procedures, adequate information about size, morphology or dispersity is needed to tailor the synthesis conditions by manipulating the reagents or physical impact during synthesis.[77, 84, 86-90] There is a high need to provide a correlation between the final morphology of nanoparticles and the preferred experimental parameters by analyzing particle ultrastructural and crystallographic growth.

Based on the results, it can be concluded that the reduction of silver with glucose in the presence of PVP mostly led to spherical nanoparticles, but triangles also occurred at a very early stage. Their fraction grew with increasing reaction time. Moreover, a few rod-like particles were observed at later stages. It is remarkable that both spherical and triangular particles continued to grow during synthesis, and that they seemed to originate from different nucleation events. After about 1000 min, the dynamics of the system appeared to have ceased. It was demonstrated that the increase in domain size was proportional to particle size. The nanoparticles just grew in size together with their domains. The silver lattice unit cell parameter *a* was significantly increased in the nanoparticles by about 0.002 Å. Neither air exposure nor ambient light had a significant effect on the reaction products.

Adapted with permission from S. Banerjee, K. Loza, W. Meyer-Zaika, O. Prymak, M. Epple, "Structural evolution of silver nanoparticles during wet-chemical synthesis", Chemistry of Materials 26 (2014) 951-957. Copyright (2015) American Chemical Society.

5.3 Behavior of silver compounds in biological media

Silver is increasingly used as a biocidal agent in many applications.[11, 16, 59, 91-97] To meet the diversity of application types, different kinds of silver compounds have been developed to serve this market. However, there are increasing concerns about potential risks to humans and the environment, especially in the case of silver nanoparticles.[3, 7, 98-102] The most potent compounds for a high silver release are soluble silver salts like silver nitrate or silver acetate. These are fully water-soluble with a high rate of silver ion release. They are often used in cell culture experiments to elucidate the biological effect of silver.[31, 61, 93, 102-112] In these cases, it is tacitly assumed that the concentration of free silver ions is the same as that of the added silver salts. This obviously cannot be the case, because a whole set of proteins, biomolecules and inorganic ions like chloride and phosphate is present in the biological medium. These will react with silver ions in one way or another, reducing the concentration of dissolved silver ions, as pointed out by a number of authors.[30, 103, 108] This is also true for engineered silver nanoparticles after their release into the environment.[7, 107, 109, 113]

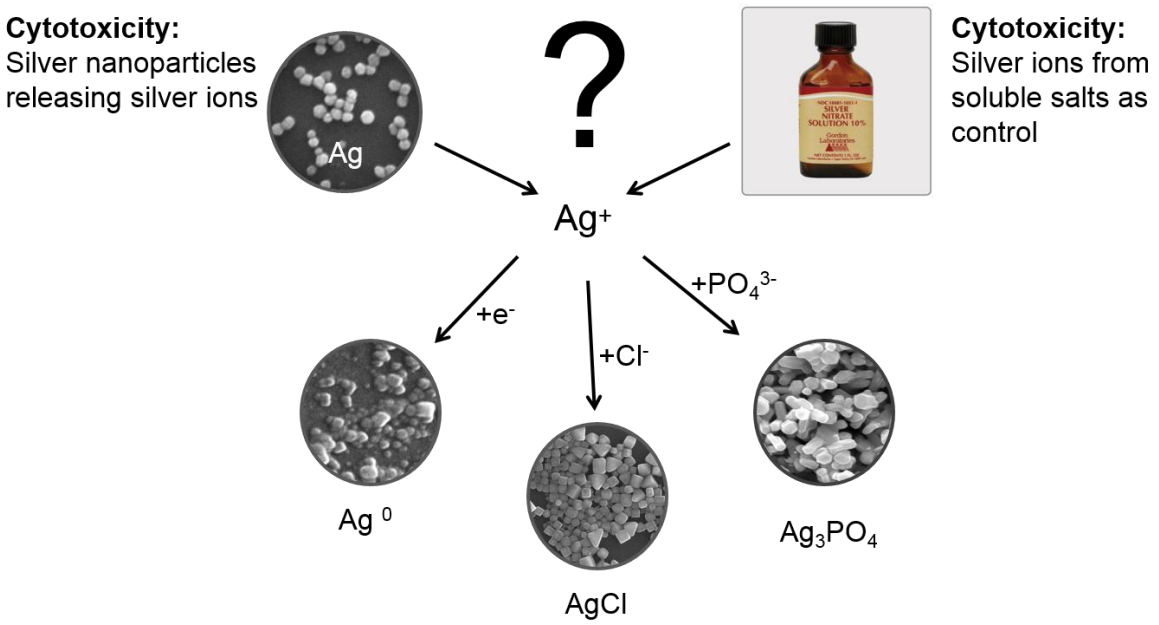

Figure 20: Schematic representation of possible interactions of silver ions (released from silver nanoparticles or from soluble silver salts) with components of biological media.

Figure 20 shows possible predicted reactions that can occur in complex media:

- precipitation of silver phosphate in the presence of phosphates,
- precipitation of silver chloride in the presence of chloride,
- reduction silver ions by sugar molecules,
- complex formation of the silver ions with a variety of biomolecules within a cell, *e.g.,* nucleic acids, lipids or sulfhydryl groups of metabolic enzymes.

Here, the behavior of silver compounds was addressed in biologically relevant concentrations in different media, from physiological salt solution over phosphate-buffered saline solution to cell culture media. X-ray diffraction methods were used for

sample characterization as a non-destructive analytical technique to reveal information about the crystallographic structure, chemical composition, and physical properties of centrifuged reaction products during the interaction between silver ions and the constituents of biological media. By scanning electron microscopy, information was obtained about the surface morphology and elemental composition of the resulting products (energy-dispersive X-ray spectroscopy) after the interaction of silver nitrate with biological media that also contain proteins.

5.3.1 Immersion experiments of silver nitrate in biological media

As a model system of free silver ions silver nitrate was added to different biological media with silver ion concentrations between 0.01 g L^{-1} and 0.1 g L^{-1} (10 to 100 ppm). This was the typical range for biological studies using silver.[11, 31] The solutions of silver nitrate were stirred at room temperature for 7 days under sterile conditions. Light was not explicitly excluded. The isolation of possible products was accomplished by ultracentrifugation.

The results are summarized in Table 2 and show that silver ions, initially present as silver nitrate, were mainly precipitated as AgCl if chloride was present. In all cases, sub-microparticles of silver chloride were found. The only exception was the aqueous solution of glucose in the absence of chloride (*i.e.* a reducing agent), where metallic silver was found. Glucose was able to reduce Ag^{+} to Ag^{0}. Silver phosphate was not observed in any case, probably due to the moderate pH (around 7) at which phosphate is mostly protonated to hydrogen phosphate and dihydrogen phosphate. In the absence of biomolecules, the silver chloride crystals were able to grow until the supersaturation was consumed by crystallization. No metallic silver was found by X-ray diffraction together with silver chloride, indicating that any reduction (*e.g.,* by light) was either minor or absent. The equilibrium concentration of free ionic silver can be calculated using the solubility product of AgCl ($1.7 \cdot 10^{-10}$ mol^2 L^{-2}).[11]

Table 2: Nature of the formed solid, isolated by ultracentrifugation, after adding silver nitrate at a silver concentration of 0.1 g L^{-1} (100 ppm) and stirring for 7 days at room temperature. The particles were analyzed by SEM, EDX and XRD. The maximum possible amount of dissolved free Ag^+ in equilibrium was calculated by the chemical equilibrium software Visual MinteQ 3.0.

Medium (aqueous solutions)	Size of the particles by SEM / nm	Maximum possible concentration of Ag^+ in the immersion medium / µg L^{-1}	Concentration of Cl^- / mol L^{-1}
glucose (2 g L^{-1})	50..100 (Ag^0)	-	0
NaCl (0.9%)	300..1000 (AgCl)	0.225	0.154
NaCl (0.9%) + glucose (2 g L^{-1})	700..1500 (AgCl)	0.225	0.154
PBS	500..1000 (AgCl)	0.250	0.139
PBS + glucose (2 g L^{-1})	800..1500 (AgCl)	0.250	0.139
RPMI 1640 medium + 10% FCS	200..350 (AgCl)	0.327	0.108
LB medium	30..50 nm (AgCl)	0.372	0.085

The dispersed particles were also detected by nanoparticle tracking analysis (NTA) in RPMI + 10% FCS (Figure 20). The measurement was performed after incubation of silver nitrate for 10 min. This was not possible in Lysogeny Broth (LB) medium due to the its high turbidity and the small silver chloride crystals. For primary systems (solvent without silver nitrate) and the reaction products (after addition of silver salt), experimental data based on nanoparticle tracking analysis were used to determine the size distribution profile of such small particles in suspension. The initial components were silver nitrate and cell culture medium supplemented with fetal calf serum. The resulting reaction products were likely to be present in the colloidal state, because of the presence of biomolecules, like proteins. It is probable that a protein corona prevented formed products from agglomerating. In biological fluids, proteins bind to the surface of nanoparticles to form a coating known as the protein corona, which can critically affect the interaction of nanoparticles with living systems. Since physiological systems are highly dynamic, it is important to obtain a time-resolved knowledge of protein-corona formation.[114]

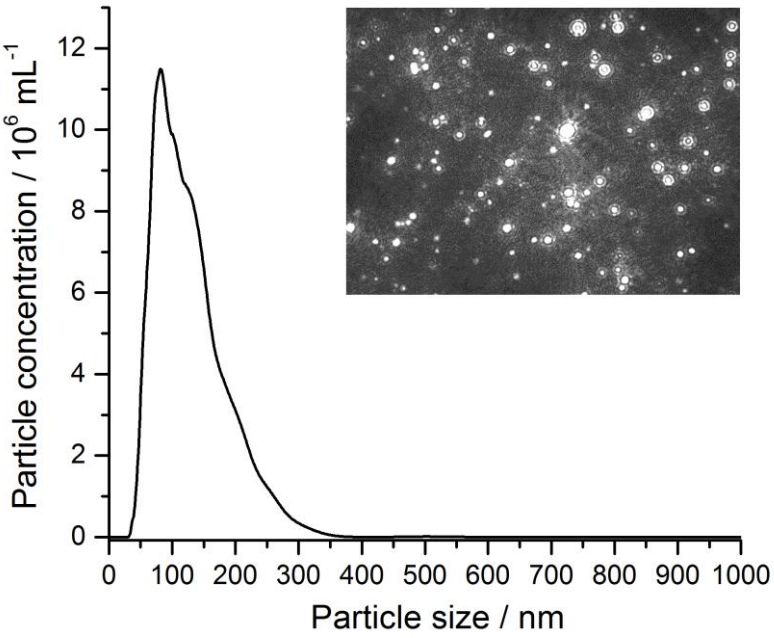

Figure 20: Particle size distribution and representative scattering image (right corner) from 10 µg mL^{-1} Ag^{+} (10 ppm) after 10 min incubation in RPMI + 10% FCS. In the control experiment (pure RPMI + 10% FCS), no scattering particles of this size were observed.

Figure 21 shows SEM images of AgCl nanoparticles, isolated from phosphate-buffered saline (PBS) (*i.e.* no protein present) and Lysogeny Broth (LB) medium, respectively. LB medium is a nutritionally rich medium used for the growth of bacteria. The typical formulation of LB medium contains peptides and casein peptones, vitamins, trace elements (*e.g.,* sulfur, magnesium), and minerals (sodium chloride). On the other hand, PBS is a salt solution containing sodium phosphate, sodium chloride, potassium chloride, and potassium phosphate. The isolated particles from LB medium were around 30-50 nm, most likely due to the presence of a protein corona, which inhibits the further growth of crystals.[115-125] The morphology of isolated particles from protein-containing media was difficult to determine due to the resolution limit of SEM and the

residual organic matrix. However, particles isolated from PBS showed the morphology typical of synthetic silver chloride.

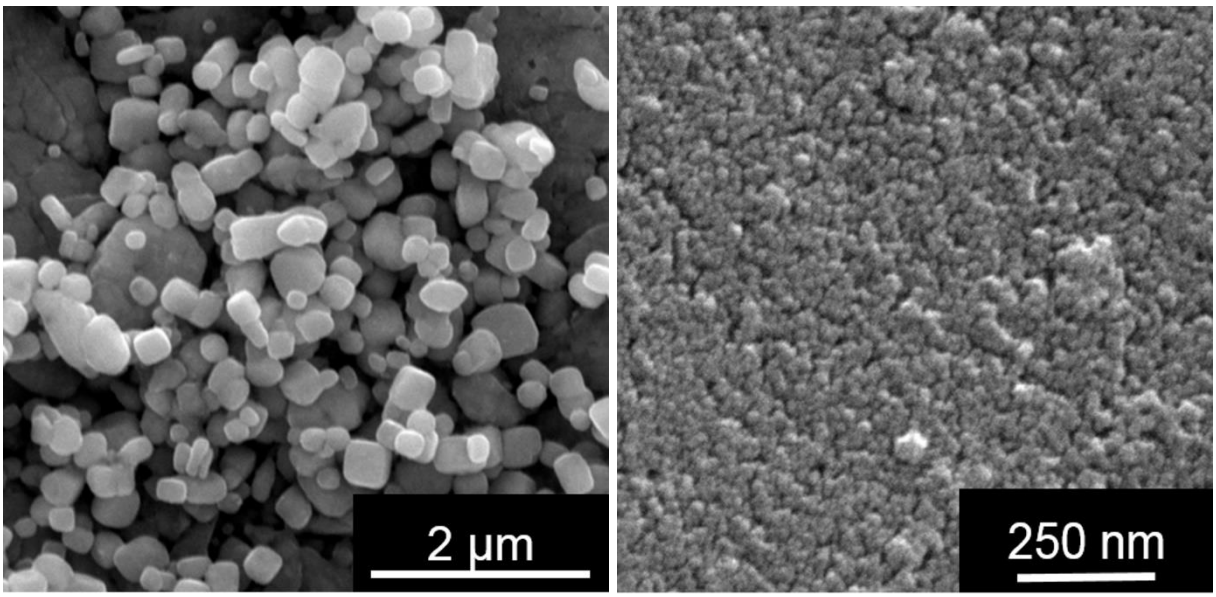

Figure 21: Representative scanning electron micrographs of silver chloride nanoparticles, isolated from PBS (no proteins present; left) and LB medium (high protein concentration; right).

Figure 22 shows X-ray diffractograms of the products isolated from LB medium and PBS. The identified phase was silver chloride. For this, the formed particles were isolated by ultracentrifugation and redispersion in pure water. As mentioned before, neither elemental silver nor silver phosphate was detectable. Notably, the narrow diffraction peaks corresponded to sub-microparticles isolated from PBS. These result were in good agreement with scanning electron microscopy (Figure 22), while a characteristic peak broadening gave information about the crystallite size.

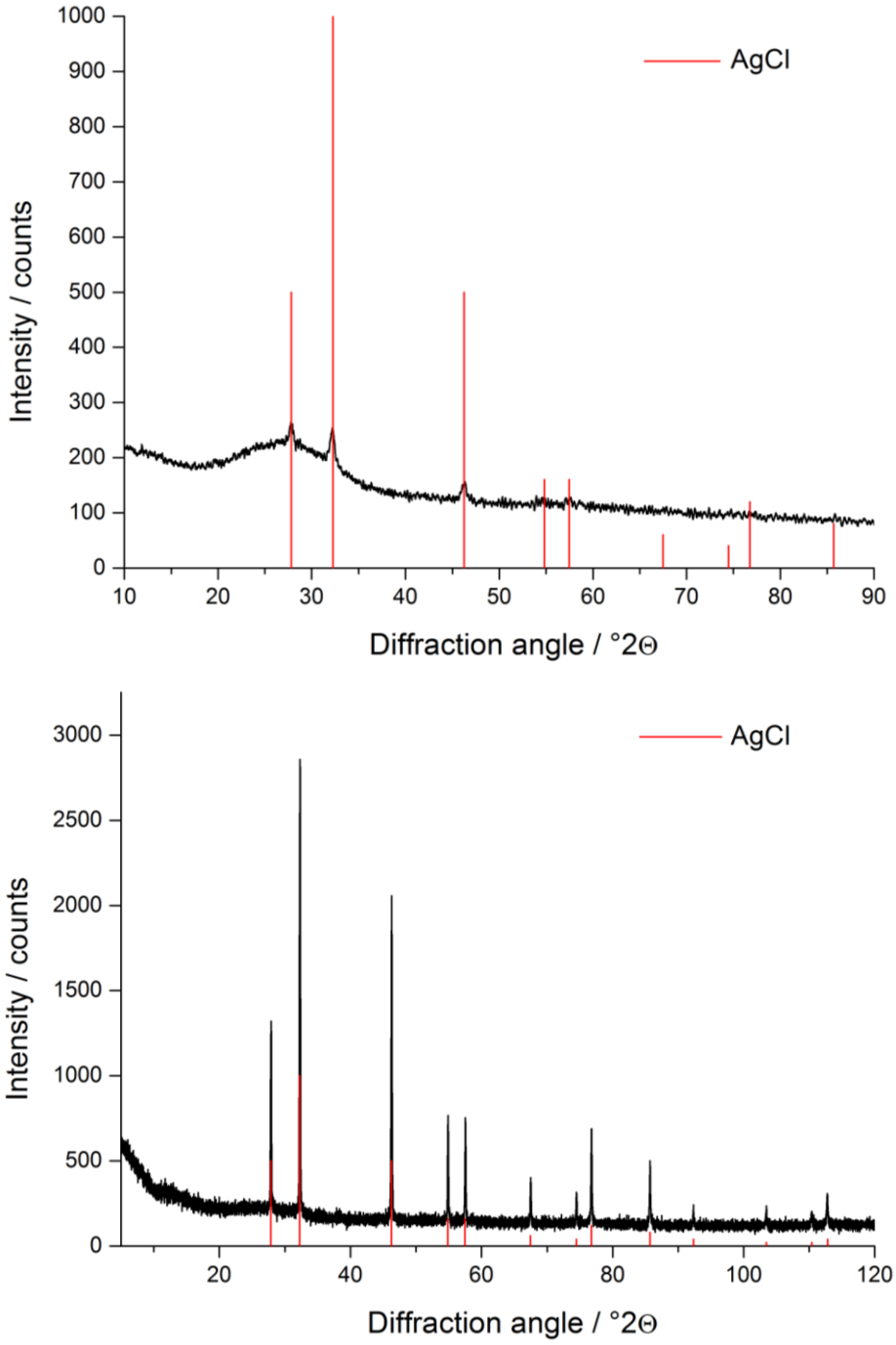

Figure 22: Representative X-ray powder diffractograms of precipitates isolated from LB medium (upper pattern) and PBS (lower pattern). The silver chloride peaks are denoted by red bars (PDF No. 00-031-1238)

5.3.2 Immersion experiments of silver nanoparticles in biological media

In order to better understand the processes during immersion, the studies were extended by mixing silver nanoparticle dispersions with media of increasingly biological nature and studying the (nano-)particulate reaction products. As a model for engineered particles, PVP-coated silver nanoparticles were used. The detailed characterization of the nanoparticles was described in Chapter 5.2. The dispersions were stirred for equilibration (7 days) and then subjected to ultracentrifugation. All precipitates and nanoparticles were isolated by this method and then analyzed by scanning electron microscopy, energy-dispersive X-ray spectroscopy and X-ray powder diffraction. This gives an essential view on all the particulate species that are present after immersion. Table 3 summarizes the results. The original silver nanoparticles were found to be practically unaffected after the immersion, indicating that they had only partially dissolved. It is important to mention that the gravimetric determination of the amount of precipitate was impossible due to the very small amount (about 10-100 mg from 1 L of dispersion).

Table 3: Results of the immersion experiments after 7 days. PVP-stabilized silver nanoparticles were used at a concentration of 0.1 g L^{-1}. All solid products were isolated by ultracentrifugation. The possible amount of dissolved Ag^+ was calculated by the chemical equilibrium software Visual MinteQ 3.0.

Medium	Diameter of the particles by SEM / nm	Maximum possible concentration of Ag^+ in the immersion medium / µg L^{-1}	Concentration of Cl^- / mol L^{-1}
glucose (2 g L^{-1})	Ag (70 nm)	N/A	0
NaCl (0.9%)	Ag (70 nm), AgCl (400-800 nm)	0.225	0.154
NaCl (0.9%) + glucose (2 g L^{-1})	Ag (70 nm), AgCl (200-500 nm)	0.225	0.154
PBS	Ag (70 nm), AgCl (200-300 nm)	0.250	0.139
PBS + glucose (2 g L^{-1})	Ag (70 nm), AgCl (200-500 nm)	0.250	0.139
RPMI medium +10% FCS	Ag (70 nm), AgCl (110-140 nm)	0.327	0.108
LB medium	Ag (70 nm), AgCl (250-300 nm)	0.372	0.085

In the case of silver nanoparticles, the situation was very similar to that resulting from the immersion of soluble silver salt in biological media. The released silver ions were mainly precipitated as AgCl if chloride is present. The maximum concentration of silver was computed in the presence of various inorganic ions and it was found that less than 1 µg of silver per liter may be present in thermodynamic equilibrium. This neglect both the influence of organic species that may act as coordinating ligands, and a possible non-equilibrium state of the dispersion.[126, 127] The initially present silver nanoparticles were recovered in all cases. Silver phosphate was not observed in any case, probably due to the moderate pH (around 7) at which phosphate is mostly protonated to hydrogen phosphate and dihydrogen phosphate.

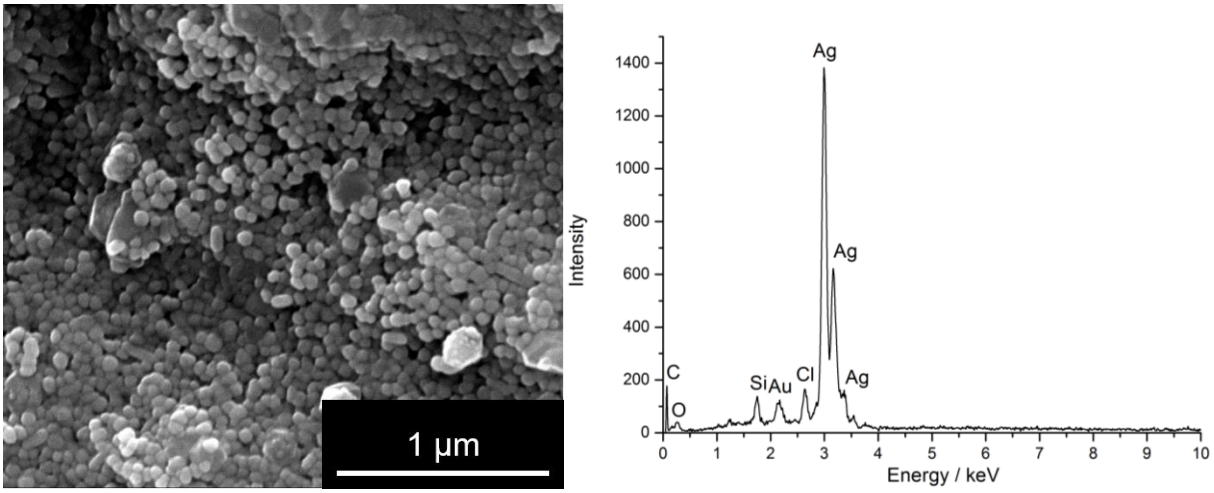

Figure 23: Scanning electron micrograph (left image) and energy-dispersive X-ray spectrum (right image) of products isolated from PBS solution after the immersion of silver nanoparticles.

Figure 23 shows particles isolated from PBS and their elemental composition. PVP-coated silver nanoparticles remained unchanged. This was supposedly due to the similar particle distribution before and after immersion. On the micrograph, some secondary formed particles were present. The particle morphology was typical for silver chloride crystals. The EDX spectrum revealed the presence of silver and chlorine. The signals of Si and Au resulted from the background and sputtering of

samples prior to microscopy, respectively. The carbon and oxygen peaks can be attributed to the polymer content of PVP-coated silver nanoparticles, since these elements were also present in the EDX spectrum of silver nanoparticles from the aqueous solution (see Chapter 5.2).

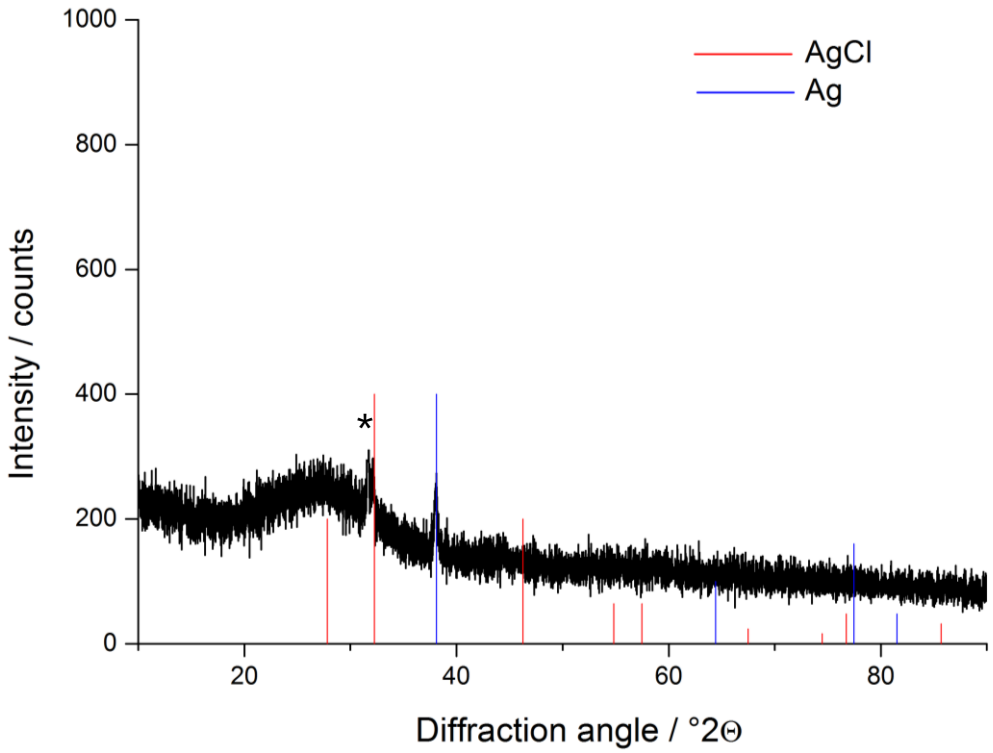

Figure 24: X-ray powder diffractogram of particles isolated from RPMI + 10% FCS medium. Peaks of silver chloride and elemental silver are denoted by red and blue bars, respectively. An asterisk corresponds to sodium chloride peak.

X-ray powder diffractogram of particles isolated from RPMI + 10% FCS medium is displayed in Figure 24. Although the samples were proceeded to a wash step, the peak of sodium chloride was still present. The elemental silver and silver chloride were present.

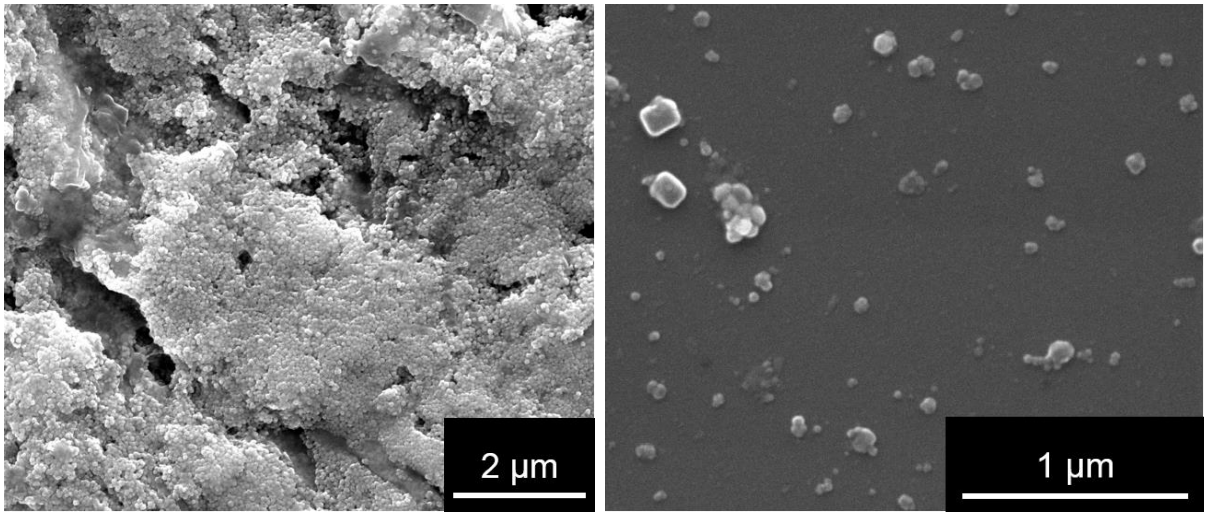

Figure 25: Representative scanning electron micrographs of particles isolated from RPMI + 10% FCS medium after immersion.

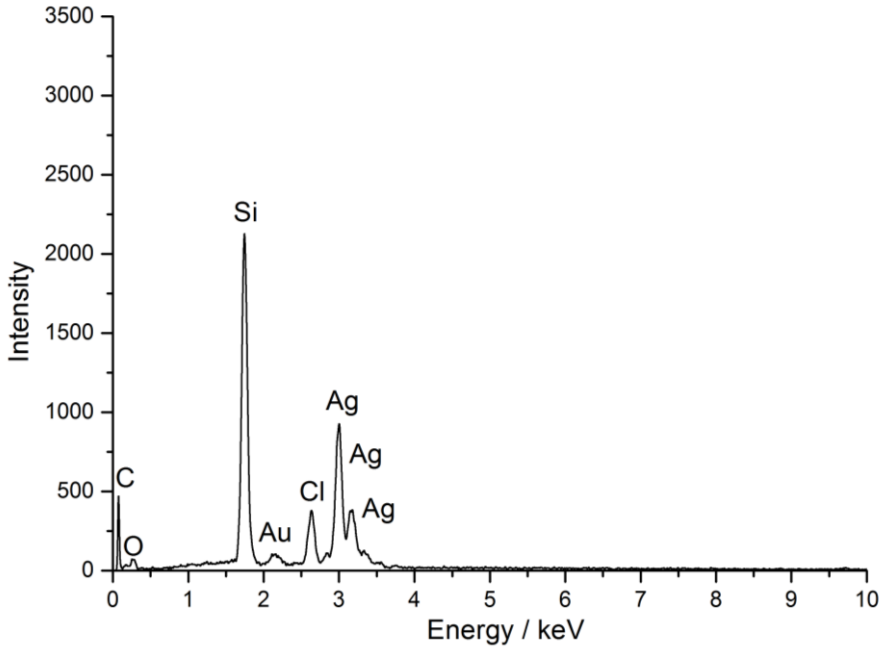

Figure 26: Energy-dispersive X-ray spectrum of particles isolated from RPMI + 10% FCS medium after immersion.

Micrographs (Figure 25) show isolated silver nanoparticles and secondary formed particles after incubation in RPMI + 10% FCS medium. The particles with cubic morphology were detectable. Silver chloride crystallizes typically in cubic morphology. The high content of proteins made the analysis complicated, while the isolated precipitates were covered with serum from the medium. The EDX spectrum showed the signal from silver and chlorine (Figure 26). The silicon signal was from the background, and gold came from sputtering of samples prior to microscopy. The carbon and oxygen peaks could be attributed to the polymer content of PVP-coated silver nanoparticles as well as to residual proteins from the immersion experiments.

In conclusion, in chloride-containing media, silver ions were mostly precipitated as silver chloride (Figure 27). If high amounts of proteins were present, as it is usually the case in cell culture media and biological fluids (*e.g.*, blood), the silver chloride particles remained in nanoparticulate state, surrounded and preserved by a protein corona, which prevented further growth of crystals.

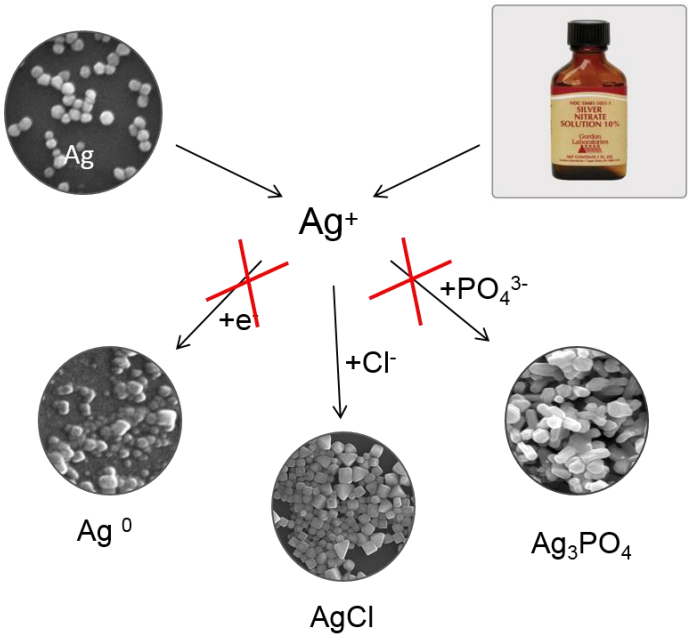

Figure 27: Schematic representation of the interactions of silver ions with components of biological media.

5.3.3 Characterization of PVP-coated silver chloride nanoparticles

Since most of the cell culture studies using silver ions as a control are actually studying the influence of colloidal silver chloride on the cells, comparable particles which are colloidally stable in biological media were prepared.

Synthetic silver chloride particles were obtained by precipitation in the presence of PVP. Here, PVP was needed to enhance the colloidal stability of formed particles. Before characterization, the dispersions were subjected to ultracentrifugation, to remove the polymer excess and by-products (sodium nitrate). The purified PVP-coated silver chloride nanoparticles were analyzed by dynamic light scattering, scanning electron microscopy, and energy-dispersive spectroscopy. All samples were stored at 4 °C in the dark until further analysis. Storage under light exclusion is necessary, as silver chloride is known to be a photosensitive material and may rapidly darken on contact to light by decomposing into elemental chlorine and metallic silver.

The mean particle size was around 120 nm as measured in aqueous dispersion by dynamic light scattering (Figure 28). The PVP-coated silver chloride nanoparticles possessed a zeta potential of -42 mV, indicating electrosteric stabilization. The surface charge could be a consequence of adsorbed anions (*i.e*, Cl^-). Figure 28 shows representative micrographs of prepared silver chloride nanoparticles. The resulting morphology was very similar to that of particles isolated from PBS. The edge length of the synthetic PVP-coated silver chloride cubic nanoparticles was about 100 nm, as measured by electron microscopy.

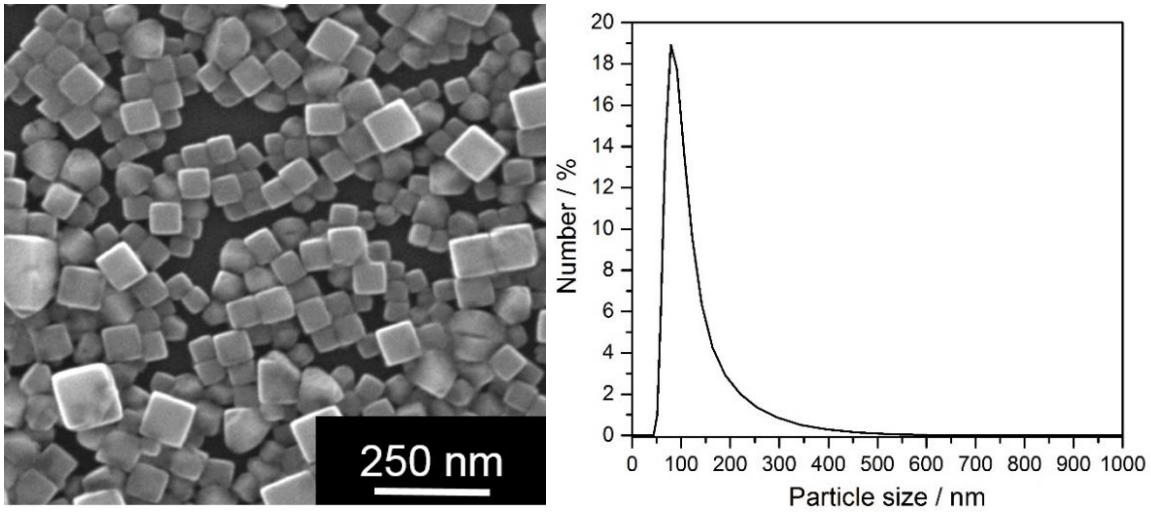

Figure 28: Representative electron micrograph of synthesized AgCl-PVP nanoparticles (left) and the associated particle size distribution (by number) determined by DLS in ultrapure water (right).

Synthetically prepared silver chloride nanoparticles were stable in cell culture medium RPMI + 10% FCS at least for a week, which is sufficient for further biological investigations. Their stability was estimated by dynamic light scattering, plotting hydrodynamic diameter and time of incubation.

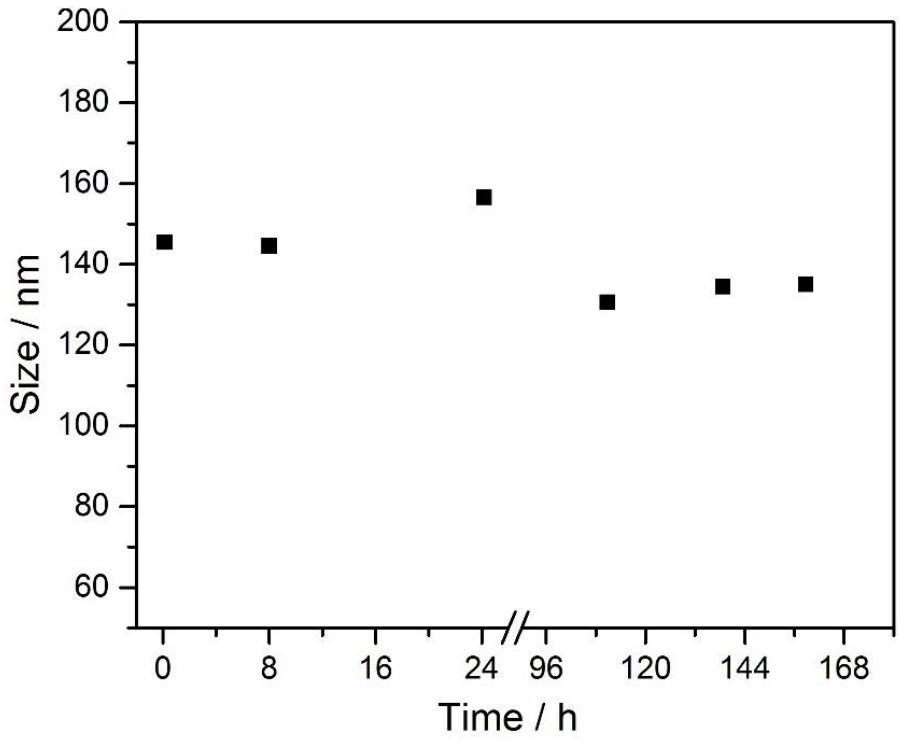

Figure 29: DLS measurements of synthetic AgCl-PVP nanoparticles, dispersed in RPMI + 10% FCS medium at 37 °C under sterile conditions up to 150 h. No precipitation or coagulation was observed.

5.3.4 Characterization of fluorescent silver chloride nanoparticles

To study the cellular uptake of synthetically prepared silver chloride, nanoparticles were treated with the organic dye fluorescein. In particular, silver chloride nanoparticles were synthesized in the presence of poly(ethylenimine) (PEI) and additionally functionalized by fluorescein. Then, the dispersion was purified by ultracentrifugation and redispersion in ultrapure water by sonication. Thereby Cl^-, excess PEI, and excess Ag^+ were all removed. All samples were stored at 4 °C in the dark until further analysis. The storage under light exclusion is necessary because of the photochemical decomposition of AgCl to elemental silver and chlorine.

Scanning electron micrograph shows fluorescent silver chloride nanoparticles with typical cubic morphology and an edge length of about 80 nm. The success of functionalization with the organic dye was confirmed by fluorescence spectroscopy. The emission spectrum is characteristic for fluorescein.[128]

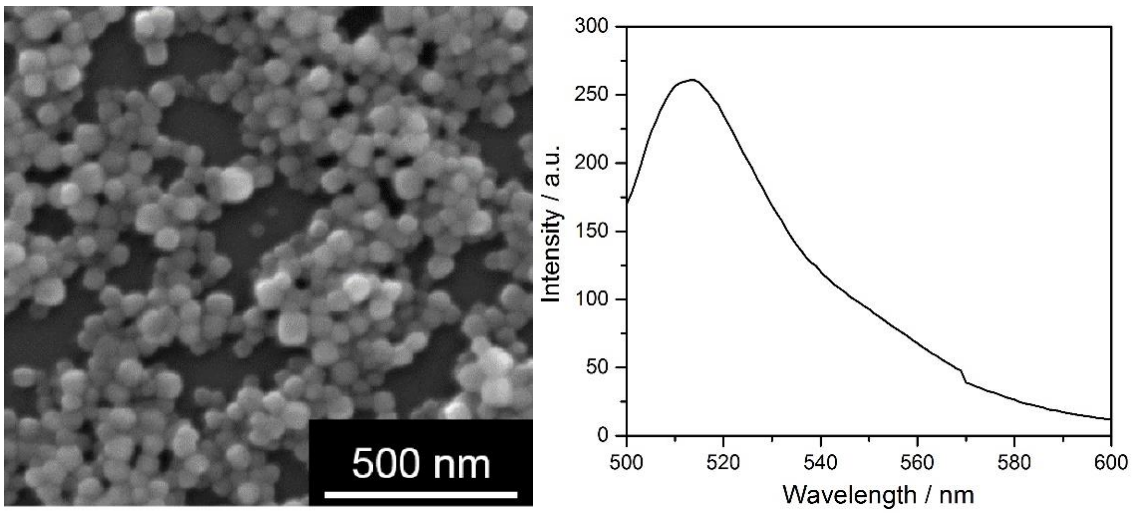

Figure 30: SEM image of AgCl nanoparticles, stabilized with PEI and labelled with fluorescein (left) and a corresponding fluorescence spectrum (right), excitation wavelength 490 nm.

Table 4 summarized the characterization data of the synthesized silver chloride nanoparticles in comparison to those formed in the biological media. The size of particles formed in media varied from 30 to 350 nm, depending on immersion medium. Synthetically prepared particles were of the same magnitude. It is the important to note that fluorescent silver chloride nanoparticles were highly positively charged due to the functionalization with PEI. This should be taken into account for the discussion of biological experiments, where the nanoparticle surface charge is significant for investigation of cellular uptake.[129]

Table 4: Colloid-chemical data of silver chloride particles, both isolated from biological media and synthetically prepared as colloidal dispersion in ultrapure water. Note that not all data were accessible for particles in biological media due to practical constraints (mainly the turbidity in solutions with high protein content).

	Size by DLS / nm	Size by SEM / nm	Zeta potential / mV	Size by NTA / nm
AgCl in LB	-	30..50	-	-
AgCl in RPMI+10% FCS	-	200..350	-	50..350
AgCl-PVP	120	100	-42	110
AgCl-PEI-FI	220	80	+67	180

5.3.5 Toxicity of silver chloride nanoparticles towards cells and bacteria

The data showed that the released silver ions precipitated mostly as AgCl in biological media, and that most cell culture studies where silver ions were used as a control were in fact studying the effect of colloidal silver chloride on the cells. To prove this assumption, human mesenchymal stem cells (hMSCs), monocytes, and T-cells were cultured in the presence of synthetically prepared silver chloride nanoparticles, and the viability of the cells was analyzed by fluorescence microscopy. The viability was evaluated by calcein-AM assay. As a control, silver acetate was used in cell culture media in the same concentration range as synthetically prepared silver chloride nanoparticles. Antimicrobial studies were performed on the relevant bacterial strain *S. aureus.* This bacterial strain is gram-positive bacterium and is often found in the respiratory tract and on the skin.

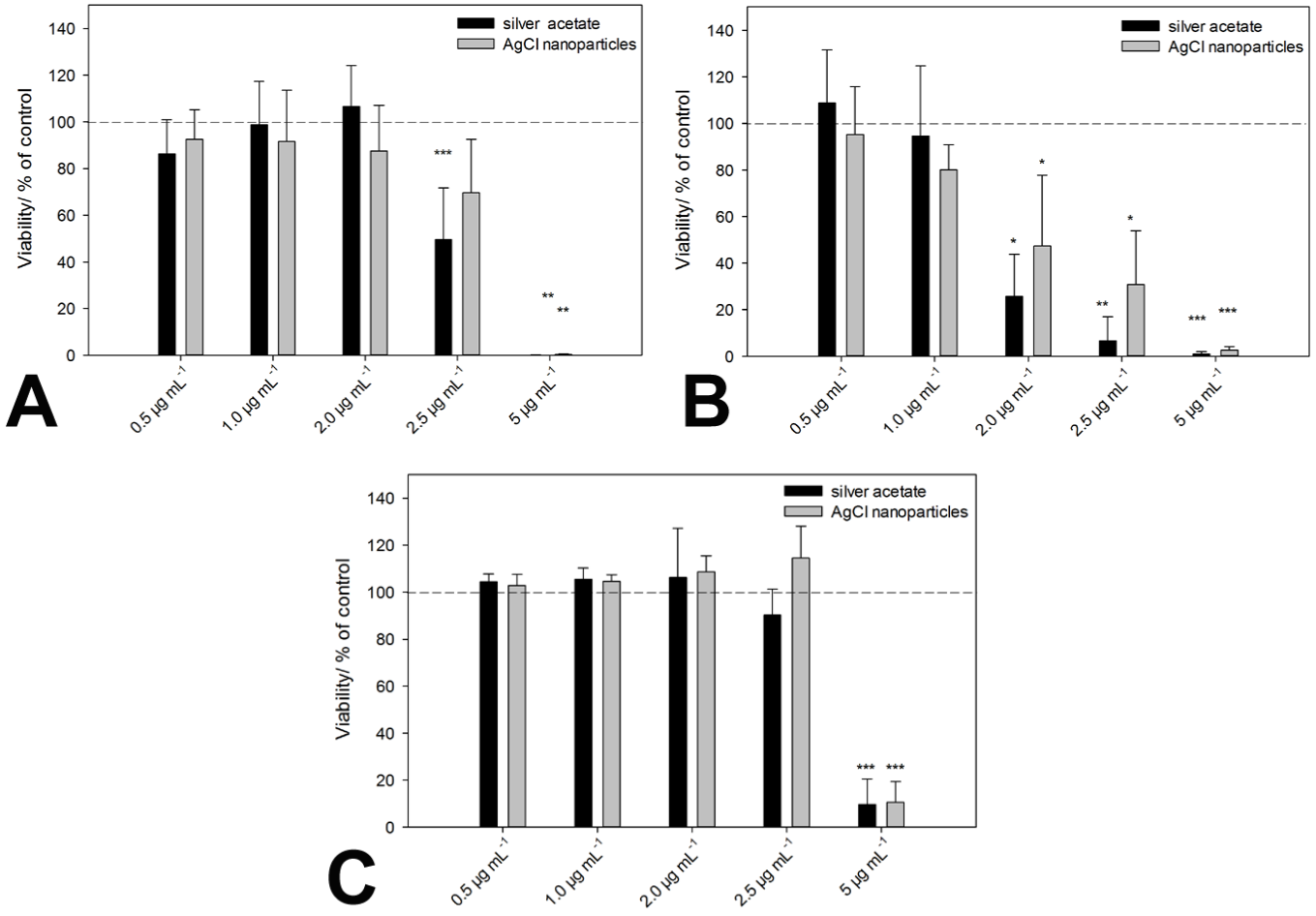

Figure 31: Cytotoxicity of ionic silver (silver acetate) and PVP-stabilized AgCl nanoparticles towards hMSCs (A), monocytes (B), and T-cells (C). Cells were treated with different concentrations of silver acetate and PVP-coated silver chloride nanoparticles (normalized to the same silver concentration) for 24 h under cell culture conditions, respectively.

Figure 31 shows the concentration-dependent silver toxicity without significant differences between different cell lines. Viable hMSCs were quantified by digital image processing (phase analysis). T-cell and monocyte viability were determined by measuring the cell number: counting cell events for 30 s under constant flow. The data were expressed as mean±standard deviation (*N*=3) given as the percentage of the

control (cells cultured without silver). An asterisk (*) indicates significant differences in comparison to the control (* $p<0.05$, ** $p<0.01$, *** $p<0.001$).

A similar effect was also observed for bacterial strains. The characteristic data of antimicrobial tests are shown in Table 5.

Table 5: Cytotoxicity of ionic silver (silver acetate) and PVP-stabilized AgCl nanoparticles towards *S. aureus.* The antibacterial effect against *S. aureus* was analyzed by measuring the minimal bactericidal concentration (MBC).

	Silver acetate (N = 3)	AgCl nanoparticles (N = 3)
Cell density / mL^{-1}	MBC / µg mL^{-1} Ag	MBC / µg mL^{-1} Ag
$1 \cdot 10^3$	2.0	2.0
$1 \cdot 10^4$	2.0	2.5 to 2.0
$1 \cdot 10^5$	2.5	5.0
$1 \cdot 10^6$	5.0	5.0

It is interesting that there is no significant difference between the biological action of silver ions and silver chloride nanoparticles towards eukaryotic cells and bacteria. As shown earlier, the cytotoxic concentration of silver acetate against eukaryotic cells and bacteria (*E. coli*) is in the same concentration range, and gram-negative bacteria are affected by silver ions in the same way as gram-positive bacteria.[11, 31] This underscores the presence and biological effect of dispersed AgCl nanoparticles in both cases. Finally, fluorescing nanoparticles of silver chloride were prepared to follow their pathway into cells. HeLa cells were chosen as a suitable model cell line.

Figure 32 shows the cellular uptake into HeLa cells which occurred within a few hours under cell culture conditions. The green fluorescence was from fluorescein, which was

used for nanoparticle labeling. The particles were accumulated in the perinuclear region. It may be assumed that the uptake occurred by endocytosis as in the case of other nanoparticles.[130-132]

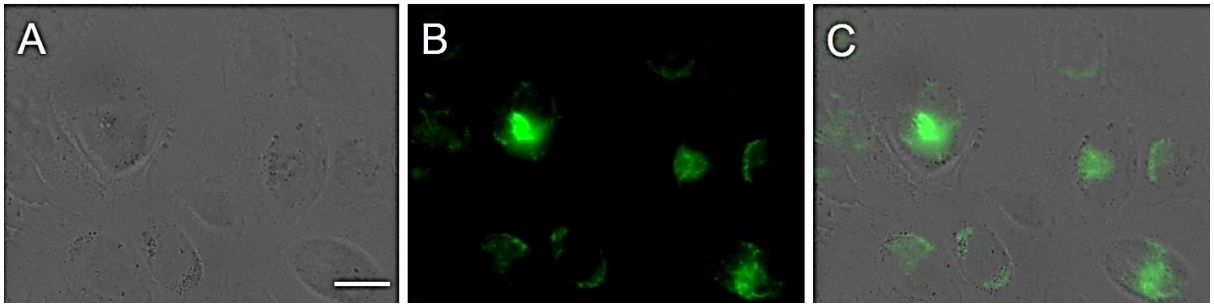

Figure 32: Cellular uptake of fluorescein-labelled AgCl nanoparticles by HeLa cells after 4 h under cell culture conditions. Prior to imaging, the cells were washed twice with PBS. Imaging was performed on unfixed cells. Fluorescently-labelled silver chloride nanoparticles show up in green. Light microscopy (A), fluorescence microscopy (B), and overlay (C) of cells with nanoparticles. Scale bar is 20 µm.

A final question remains: What is the origin of the cytotoxic effect of the AgCl nanoparticles? Obviously, it is important to differentiate the cytotoxic effect between bacteria and eukaryotic cells. The uptake of nanoparticles by bacteria is limited by the size of the particles (1-10 nm).[26, 30, 133] The attachment of these particles to the surface of gram-negative bacteria may disrupt the permeability. Moreover, they may be capable of entering the cell membrane and causing further damage to a variety of biomolecules (*e.g.,* by binding to sulfur-containing molecules or by the release of silver ions).[26, 30, 133] Thus, AgCl can be effective from the outside (*e.g.,* by disrupting the bacterial cell membrane), and also by inducing internal collateral damage like the formation of reactive oxygen species.[26] Here, the larger silver chloride nanoparticles found or prepared act from inside the eukaryotic cells due to the release of silver ions, as recently shown for silver nanoparticles.[129] It is interesting that *Zhang et al.* have shown that AgCl was less cytotoxic to red blood cells and human mesenchymal stem cells compared to the other silver materials tested. In addition, a decline in the

cytotoxicity of AgCl at significantly high concentrations was observed. This was attributed to the reduction of cytotoxicity of aggregated AgCl which limited the bioavailability of free Ag^+ ions, which is not true in our case.[108]

If AgCl nanoparticles are taken up into eukaryotic cells by endocytosis, they appear in the lysosome under acidic conditions. In principle, the solubility of AgCl should not depend on pH, with HCl being a strong acid. The conditions inside a lysosome were simulated, using the software Visual MinteQ 3.0. As a lysosomal liquid, hydrochloric acid was used with a pH of 5.[134] The calculation was performed for 100 µM silver chloride. In this case, about 10% of the AgCl is present in solution as silver ion Ag^+, with a small amount of the chloro-complex $[AgCl_2]^-$ that is also present. Therefore, the question of whether AgCl fully dissolves in lysosomes cannot yet be answered. Except for the formation of the chloro-complex and the unknown degree of complexation by biomolecules and proteins, the solubility of AgCl should not be increased inside a lysosome. However, it must be stressed that the solubility product for AgCl was derived for macroscopic crystals. As nanocrystals have a much higher specific surface area, their solubility will generally be higher, and hence their cytotoxicity will be higher than that of AgCl microcrystals.

These considerations should also apply to environmental systems like salt water with high chloride content, provided that biomolecules are present to form a stabilizing corona around the nanoparticles.[104, 135, 136]

Cell biological experiments were performed by Jun.-Prof. Dr. C. Sengstock and Dr. S. Chernousova.

Adapted from K. Loza, C. Sengstock, S. Chernousova, M. Köller, M. Epple, "The predominant species of ionic silver in biological media is colloidally dispersed nanoparticulate silver chloride", RSC Advances 4 (2014) 35290–35297 Published by The Royal Society of Chemistry.

Adapted from K. Loza, J. Diendorf, C. Sengstock, L. Ruiz-Gonzalez, J. M. Gonzalez-Calbet, M. Vallet-Regi, M. Köller, M. Epple, "The dissolution and biological effects of silver nanoparticles in biological media", Journal of Materials Chemistry B 2 (2014) 1634–1643 Published by The Royal Society of Chemistry.

5.3.6 Quantification of dissolved species of silver compounds in biological media

Silver nanoparticles are widely used due to their antibacterial action in consumer products and in medicine.[6, 11, 16, 59, 91, 93, 94, 99, 137, 138] However, there is increasing evidence that the release of silver ions from nanoparticles is responsible for this biological effect. *Xiu et al.* showed in a very sophisticated way that silver nanoparticles did not show a bactericidal effect if the bacteria were cultivated under anaerobic conditions, *i.e.* when no dissolution of the nanoparticles occurred.[61] Studies on the dissolution behavior were reported in a number of publications,[33, 61, 69, 106, 107, 109, 117, 138-147] but there is no agreement on the dissolution behavior in more complex media (*e.g.,* in biological systems and in the environment).

Based on our earlier results on the dissolution of dispersed silver nanoparticles in pure water,[60, 69] the studies were extended to more complex media. The dissolution kinetics of the silver nanoparticles were analyzed after immersion in DMEM medium supplemented with 10% FCS. Table 6 summarizes the results of dissolution experiments from the literature. The typically applied methods for silver determination are AAS or ICP-MS. The separation of silver nanoparticles and silver ions is typically accomplished by dialysis or nanofiltration. Despite the fact that there are a number of studies where the dissolution kinetics of dispersed silver nanoparticles were measured, they are practically incomparable (Table 1). The nanoparticle properties were quite different (*e.g.,* size, charge, functionalization), and it is very likely that this strongly influences the dissolution performance. Additionally, the immersion media were different and not easily comparable between the individual data points. Finally, it could be safely assumed that the total silver concentration will influence the dissolution

process, as critical factors like the solubility product of silver chloride or the reduction potential of silver ions directly depend on the concentration. However, some conclusions can be drawn, mainly by comparing results within one set of experiments, *i.e.* from one reference.

Liu et al. described the dissolution of silver nanoparticles in acetate buffer in the presence of citrate anions, sodium sulfide and 11-mercaptoundecanoic (MUA) acid and found that sulfidation and MUA reduced the dissolution rate to undetectable values.[139] They also investigated the role of humic and fulvic acid, dissolved oxygen, natural and low salt sea water and showed that the addition of organic matter can suppress the release of silver ions.[139] *Levard et al.* investigated the role of a surface sulfidation process and found that at a high ratio of sulfur to silver, the released silver content decreased to hardly detectable values.[144] *Zook et al.* measured the dissolution in cell culture medium (DMEM) and found a fractional dissolution of different polymer-coated silver nanoparticles. The dissolution was enhanced in biological media in comparison to inorganic salt solutions, which is probably due to complexation of the released silver ions.[109] *Zhang et al.* considered size effects on the dissolution kinetics in quarter-strength Hoagland medium and concluded that release rate depends on size and concentration. Smaller particles were found to dissolve faster.[145] The fate of silver nanoparticles in synthetic gastric fluid and wound fluid was studied by *Liu et al.* They reported a rapid dissolution in gastric acid in comparison to pseudoextracellular fluid and also found an interaction with thiol- and selenide-containing biomolecules. They proposed the formation of secondary thiol- and selenide-containing nanoparticles after partial dissolution in the gastrointestinal tract.[113]

Table 6: Results of dissolution experiments of silver nanoparticles. Room temperature means 25 °C. Citrate-stabilized nanoparticles can be assumed to have a negative zeta potential, but this was not always stated in the references. The immersion medium was water in all cases with the stated additives. All experiments were carried out at neutral pH, unless specified otherwise.[60]

Functionalization of silver nanoparticles	Diameter / nm	Zeta potential / mV	Silver concentration / g L^{-1}	Temperature / °C	Immersion medium	Immersion time / h	Degree of dissolution / %	Ref.
Citrate	85	-30	0.32	25	Water	336	15	[69]
Citrate	85	-30	0.14	25	Water	410	12	[69]
Citrate	85	-30	0.32	37	Water	307	56	[69]
Citrate	85	-30	0.14	37	Water	444	53	[69]
Citrate	4.8	-45	0.002	25	Air-saturated distilled water, $[O_2]$=9.1 mg L^{-1}; pH=5.68	3000	~100	[139]
Citrate	4.8	-45	0.0002	25	Air-saturated distilled water, $[O_2]$=9.1 mg L^{-1}; pH=5.68	240	~100	[139]
Citrate	4.8	-45	0.00005	25	Air-saturated distilled water, $[O_2]$=9.1 mg L^{-1}; pH=5.68	120	~100	[139]
Citrate	4.8	-45	0.00005	4	Air-saturated distilled water, $[O_2]$=9.1 mg L^{-1}; pH=5.68	120	36	[139]
Citrate	4.8	-45	0.00005	37	Air-saturated distilled water, $[O_2]$=9.1 mg L^{-1}; pH=5.68	120	96	[139]
PVP	50	-17	0.22	5	Water	411	9	[69]
PVP	50	-17	0.1	5	Water	149	8	[69]
PVP	50	-17	0.05	5	Water	149	12	[69]
PVP	50	-17	0.35	25	Water	134	48	[69]
PVP	50	-17	0.1	25	Water	81	52	[69]
PVP	50	-17	0.05	25	Water	42	43	[69]

PVP	50	-17	0.35	37	Water	27	52	[69]
PVP	50	-17	0.1	37	Water	27	89	[69]
PVP	50	-17	0.05	37	Water	11	68	[69]
PVP	70	-22	0.35	25	Oxygen-free water	1660	2	[60]
Citrate	4.8	-45	0.00005	25	Natural seawater, pH=7.90	192	38	[139]
Citrate	20	-	0.0003	25	Modified ¼ Hoagland medium, $[O_2]$=7.8 mg L^{-1}; pH=5.6	336	40	[145]
Citrate	20	-	0.0006	25	Modified ¼ Hoagland medium, $[O_2]$=7.8 mg L^{-1}; pH=5.6	336	29	[145]
Citrate	40	-	0.0003	25	Modified ¼ Hoagland medium, $[O_2]$=7.8 mg L^{-1}; pH=5.6	336	21	[145]
Citrate	40	-	0.0006	25	Modified ¼ Hoagland medium, $[O_2]$=7.8 mg L^{-1}; pH=5.6	336	20	[145]
Citrate	80	-	0.0003	25	Modified ¼ Hoagland medium, $[O_2]$=7.8 mg L^{-1}; pH=5.6	336	10	[145]
Citrate	80	-	0.0006	25	Modified ¼ Hoagland medium, $[O_2]$=7.8 mg L^{-1}; pH=5.6	336	8	[145]
PVP	70	-22	0.35	25	0.9% NaCl	3670	8	[60]
PVP	70	-22	0.35	25	PBS	3670	4	[60]
PVP	39	negative	1	25	0.01 M $NaNO_3$, pH=7	720	1.9	[144]
PVP, sulfidated	39	negative	1	25	0.01 M $NaNO_3$, pH=7	730	ca. 0 to 0.27	[144]
PVP	70	-22	0.35	25	10 mM H_2O_2	1821	90	[60]
Citrate	4.8	-45	0.002	25	Acetate buffer, pH 5.6	24	15	[139]
Citrate	4.8	-45	0.002	25	Acetate buffer, 0.4 mM citrate; pH 5.6	24	9	[139]
Citrate	4.8	-45	0.002	25	Acetate buffer, 10 mM citrate; pH 5.6	24	7	[139]
Citrate	4.8	-45	0.002	25	Acetate buffer, 0.4 mM Na_2S; pH 5.6	24	<1	[139]
Citrate	4.8	-45	0.002	25	Acetate buffer, 4 mM 11-mercaptoundecanoic acid; pH 5.6	24	ca. 0	[139]

PVP	70	-22	0.35	25	1 g L^{-1} cysteine	4366	ca. 0	[60]
PVP	70	-22	0.35	25	1 g L^{-1} glucose	4366	61	[60]
Citrate	4.8	-45	0.00005	25	Boric acid and bicarbonate low ionic strength seawater buffer, pH=7.90	192	54	[139]
Citrate	23	-	0.005	25	DMEM	22	ca. 75	[109]
Citrate	23	-	0.1	25	DMEM	22	ca. 7	[109]
PVP	23	-	0.005	25	DMEM	22	ca. 76	[109]
5 kDa PEG	23	-	0.005	25	DMEM	22	ca. 83	[109]
20 kDa PEG	23	-	0.005	25	DMEM	22	ca. 75	[109]
Dextran	23	-	0.005	25	DMEM	22	ca. 67	[109]
5 kDa PEG	23	-	0.1	25	DMEM	22	ca. 11	[109]
20 kDa PEG	23	-	0.1	25	DMEM	22	ca. 9	[109]
PVP	4-5	negative	0.005	37	Synthetic gastric acid, pH=1.12	24	~98	[113]
PVP	4-5	negative	0.005	37	Pseudoextracellular fluid, pH=7.52	24	~80	[113]

Adapted from K. Loza, J. Diendorf, C. Sengstock, L. Ruiz-Gonzalez, J. M. Gonzalez-Calbet, M. Vallet-Regi, M. Köller, M. Epple, "The dissolution and biological effects of silver nanoparticles in biological media", Journal of Materials Chemistry B 2 (2014) 1634–1643 Published by The Royal Society of Chemistry.

5.3.6.1 Determination of silver nanoparticle dissolution in Dulbecco's modified Eagle's medium supplemented with 10% fetal calf serum by atomic absorption spectroscopy

Since the silver ions are responsible for toxic effects in biological systems, the evaluation of the dissolution kinetic of silver nanoparticles is required. As described above, many studies have been performed in different media. Moreover, it was possible to show that the predominant species of silver ions interacting with cell culture components is nanoparticulate silver chloride. However, the previously used analytical protocols are unable to differentiate between various silver species.[109] Therefore, a new protocol for the determination of silver nanoparticle dissolution was developed. The schematic representation is shown in Figure 6.

PVP-coated silver nanoparticles were incubated in Dulbecco's modified Eagle's medium (DMEM) supplemented with 10% fetal calf serum (FCS) at 37 °C. DMEM is typically used cell culture fluid for eukaryotic cells and tissue. It contains salts, amino acids, vitamins, and glucose. FCS is often used to maintain cell growth. PVP-coated silver nanoparticles were characterized in Chapter 5.2 and stored under light exclusion at 4 °C before experiments.

To preserve nanoparticles from unwanted degradation by dissolved oxygen species, argon-saturated pure water was used. Ultracentrifugation was used as an effective method for the separation of solid compounds from the dissolved species. After a certain period, dispersions of possible silver chloro- or protein-complexes were separated from nanoparticulate silver chloride and remained silver nanoparticles by ultracentrifugation. The residual precipitate (precipitated AgCl and silver nanoparticles) was washed to remove the rest of the immersion medium. This was an essential point, since residual medium still contained a lot of chloride, which could disrupt further analysis. Afterwards, the dispersion was treated with nitric acid (silver dissolves completely in nitric acid) to dissolve the remaining silver nanoparticles for further quantification. Then, the solution was centrifuged to isolate solid silver chloride. Finally,

precipitated silver chloride was treated with ammonia solution to transfer it into soluble silver amino complexes. All of the received samples were analyzed by atomic absorption spectroscopy (AAS).

Such a routine procedure provided an overview of silver nanoparticle dissolution in complex media. A validation of every experimental point was possible by calculating the sample recovery. The recovery level was at 100% for all samples within the deviations (standard deviation of the AAS, minimal losses during the washing process, pipette deviations). To achieve a reproducible and consistent recovery for all samples, some optimization of the analysis process was needed. Firstly, it turned out that in spite of strongly basic or acidic solutions, adsorption of silver took place on the vessel walls of the polypropylene tube. To avoid these losses, samples were treated by ultrasonication.

Figure 34 shows the dissolution of PVP-functionalized silver nanoparticles over 168 h (7 days). The error bars are from the standard deviation of the AAS measurement plus the standard deviation of duplicate.

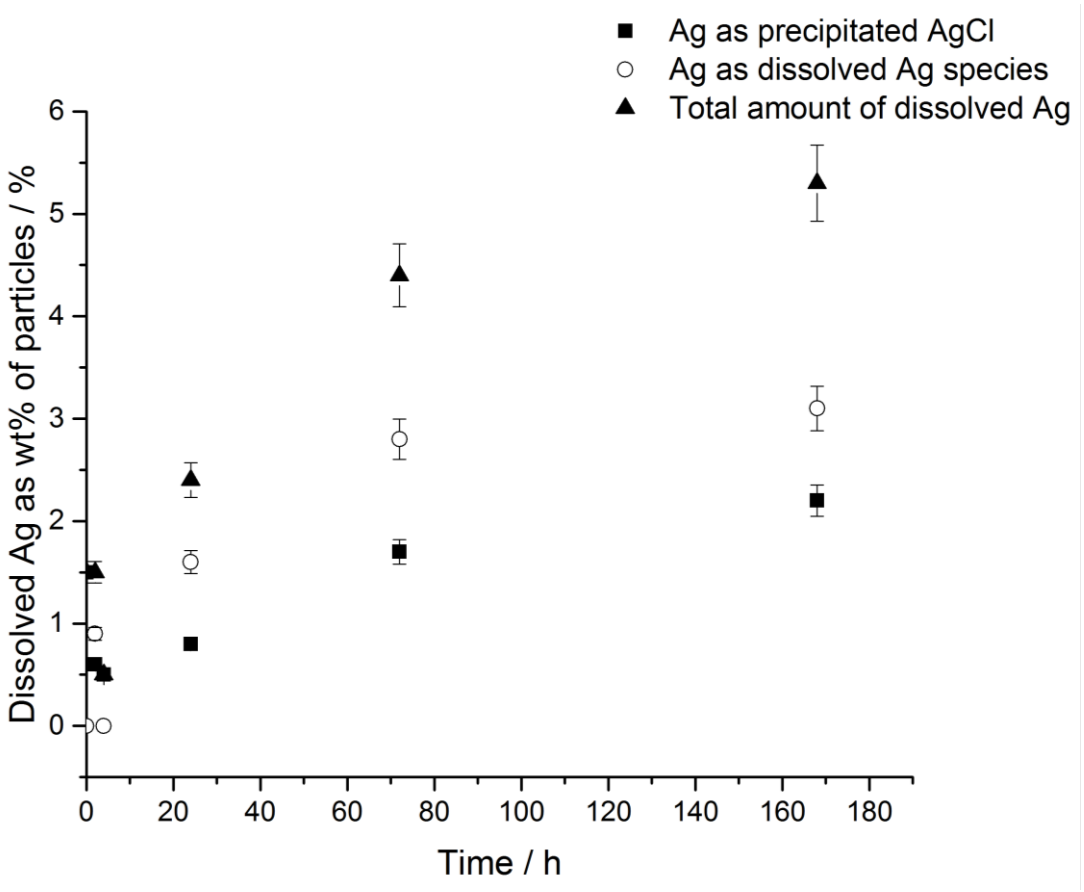

Figure 34: The dissolution of PVP-coated silver nanoparticles immersed in DMEM + 10% FCS at 37 °C. Initial concentration of silver nanoparticles was 50 µg mL^{-1}.

For 0, 2, and 4 h of incubation an accurate interpretation of the data was difficult, since the silver concentrations of the samples were partially below the detection limit of AAS (1 µg L^{-1}). Nevertheless, the trend shows that in the first few hours the amount of formed silver chloride is higher than the formation of dissolved silver species. After 168 h, it increases only slightly.

The initial trend of silver nanoparticle degradation slowly approached a saturation state at about 6%. Therefore, around 5.3% of used silver nanoparticles were dissolved after a week (equivalent to 2.65 µg mL^{-1}). As a result, 2.2% arose in the form of solid silver chloride (1.1 µg mL^{-1} as Ag or 1.46 µg mL^{-1} as AgCl) and 3.1% in the form of soluble

silver compounds in various dissolved forms in the medium (1.55 µg mL^{-1}). In the described literature data (Table 6), silver chloride was out of scope.[33, 60, 69, 109, 141, 145] Nevertheless, in this study, solid silver chloride content was around 42% of dissolved silver in cell culture medium after 7 days of incubation.

In summary, by establishment of the protocol, the dissolution of silver nanoparticles was studied including the distinction between formed silver chloride and soluble silver species. After 168 h (7 days) of incubation in cell culture medium, the incorporated PVP-coated silver nanoparticles were degraded up to 6%. These results were consistent with the literature data for similar particle functionalization and size.[60, 69] The fraction of formed solid silver chloride was around 42% of total silver amount. Generally, this method can be also used for different silver particles in chloride-containing media.

5.3.6.2 Quantification of soluble silver species in biological media

In Chapter 5.3.5, the biological investigations of synthetically prepared silver chloride nanoparticles were discussed. It was found that toxic effects for silver acetate in medium occur in the same concentration range as in synthesized silver chloride nanoparticles.[148] The results were representative for eukaryotic cells as well as for bacterial strains. It was supposed that some dissolution of silver chloride can take place in lysosomes. However, the uptake of particles by bacteria is unusual.[26, 133] The rate of dissolution of silver chloride particles and the bioavailability of soluble silver species were also unknown.

To shed light on the state of silver compounds, the amount of soluble silver species was quantified. The quantification procedure was based on atomic absorption spectroscopy, since gravimetric analysis was not possible, due to the low concentrations. Ultracentrifugation was used to separate soluble silver chloro- or protein-complexes from remained particles. Afterwards, the supernatant was treated with ammonia solution and proceeded to analysis.

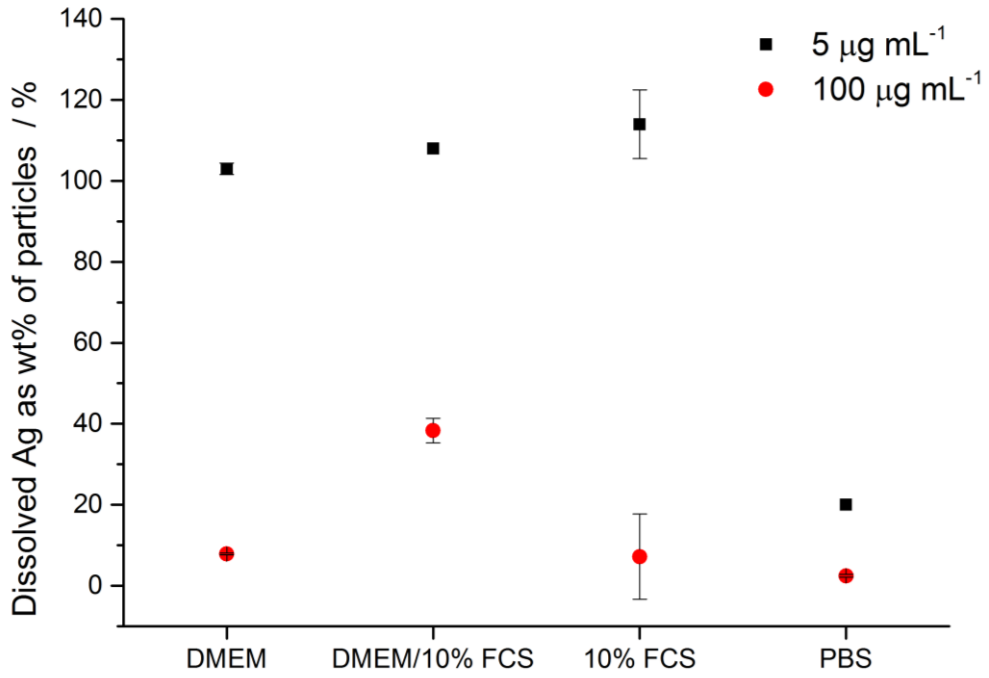

Figure 35: Amount of soluble silver species after incubation of PVP-coated silver chloride nanoparticles in biological media with different amount of serum. PVP-coated particles were incubated for 24 h; initial silver concentrations were 5 and 100 µg mL^{-1}.

Figure 35 shows the percentage of soluble silver species present in biological media with various serum contents after the immersion of engineered PVP-coated silver chloride for 24 h at 37 °C. The immersion conditions simulated relevant toxicological investigations in order to investigate the protein effect of serum-containing DMEM, serum-free DMEM, 10% FCS solution, and phosphate-buffered saline. Alone, DMEM medium contains around one weight percent of biomolecules. PVP-coated silver chloride nanoparticles were the same as used for biological tests. The physico-chemical characterization of particles was explicitly described in Chapter 5.2.

It is notable that after the incubation of PVP-coated silver chloride nanoparticles at a silver concentration of 5 µg mL^{-1} (5 ppm), silver existed as a soluble species if proteins were present. In the case of phosphate-buffered saline (no serum), only 20% of immersed silver chloride was complexed. As predicted by thermodynamics, the soluble

Ag species formed in PBS varied as a function of total Ag and Cl concentration and include Ag^+, $AgCl_2^-$, and $AgCl_3^{2-}$. No significant difference is observed between low-serum and serum-rich environments. However, after incubation of PVP-coated silver chloride nanoparticles at a silver concentration of 100 µg mL^{-1} (100 ppm), the dependence of soluble silver on protein content was observed. As shown in Figure 35, the higher the serum amount, the more silver was found in supernatant after ultracentrifugation. It was likely that these soluble compounds were in the form of silver protein complexes. Nevertheless, the identification of such complexes might be a challenge, since the exact formulation of fetal calf serum is unknown. FCS is the blood fraction remaining after the natural coagulation of blood, followed by centrifugation to remove any remaining red blood cells.

Figure 36 shows the percentage of soluble silver species present in biological media with various serum content after the addition of silver nitrate for 24 h at 37 °C. The preparation protocol was the same as for synthesized silver chloride nanoparticles. For the concentration of 5 µg mL^{-1} (5 ppm) silver was found in the supernatant if proteins were present. A closer look at the data for 100 µg mL^{-1} (100 ppm) revealed a similar trend as PVP-coated silver chloride nanoparticles.

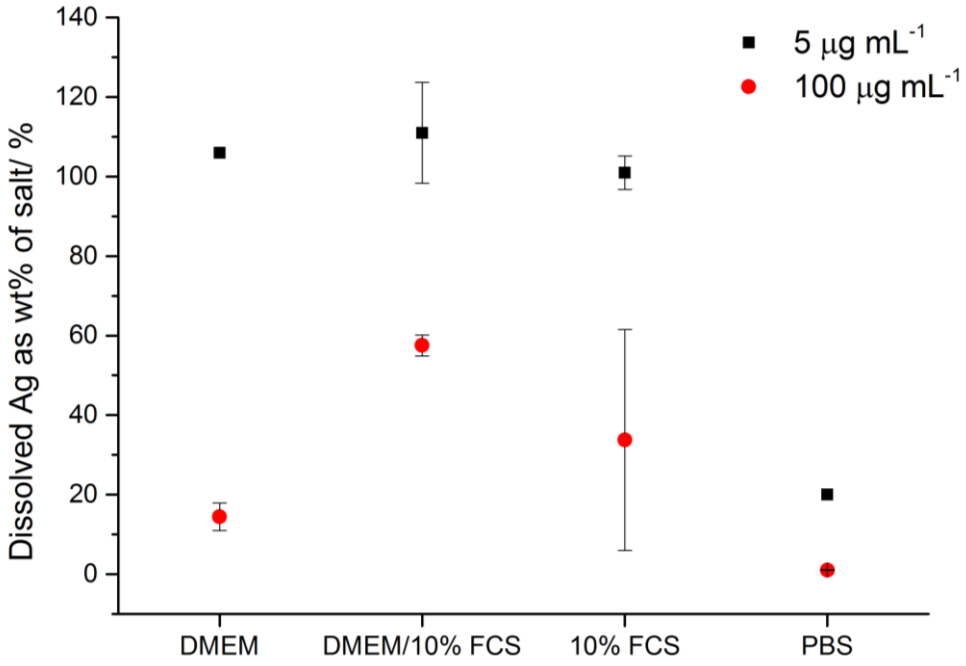

Figure 36: The amount of soluble silver species after incubation of silver nitrate in biological media with different amounts of serum. Silver nitrate was incubated for 24 h; initial silver concentrations were 5 and 100 µg mL^{-1}.

These results confirmed the effect of serum content on the availability of soluble silver species in biological media. It was possible to show that incubation in phosphate-buffered saline solution reduced the amount of silver in the supernatant.[60, 107, 104, 135, 136]

5.3.6.3 Viability of hMSCs treated with silver chloride nanoparticles in correlation of fetal calf serum in medium

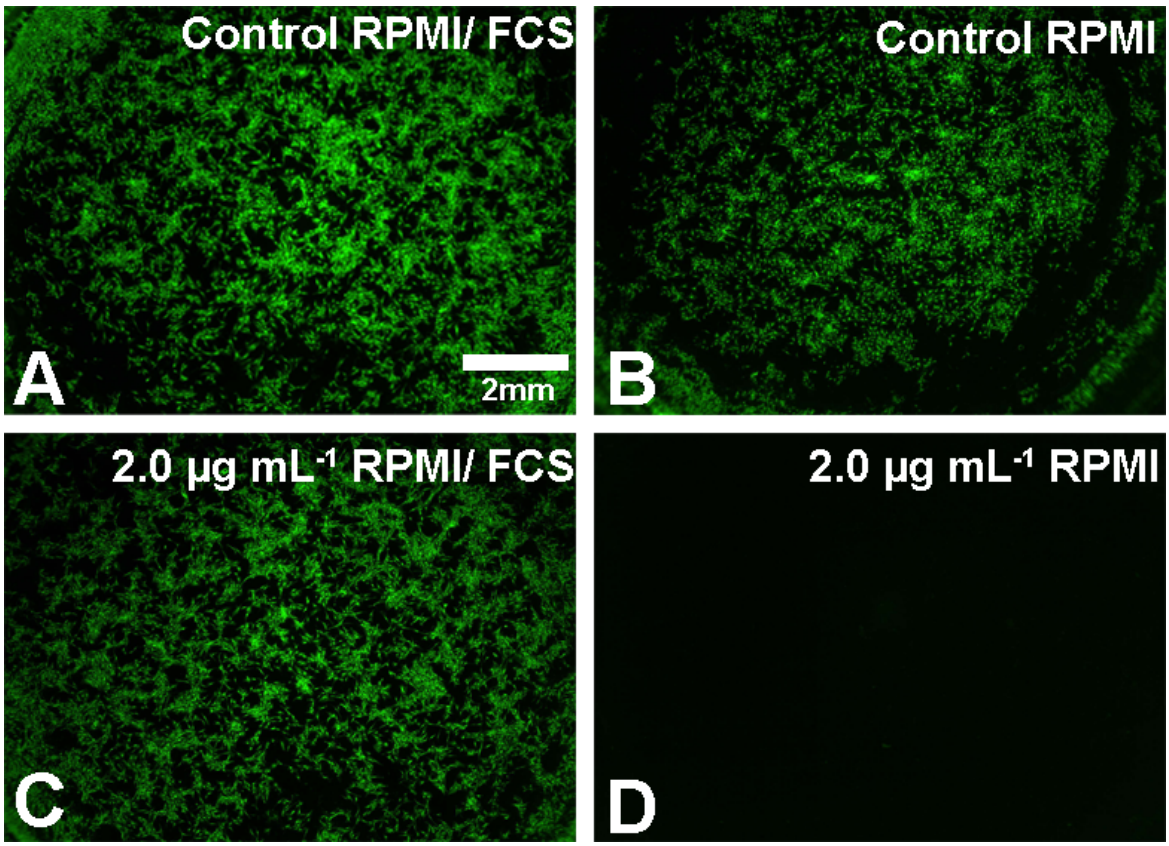

Figure 37: Fluorescence microscopy images of hMSCs incubated with silver chloride nanoparticles cultured in RPMI medium with or without 10% FCS for 24 h at 37 °C. Cultured hMSCs in RPMI + FCS (A) or RPMI (B). Cells incubated in RPMI + FCS (C) and RPMI (D) containing 2.0 µg mL^{-1} silver chloride nanoparticles for 24 h. Afterwards, the viable hMSCs were stained with calcein-AM.

The impact of silver chloride nanoparticles in the presence or absence of proteins (fetal calf serum; FCS) was analyzed after 24 h. hMSCs were incubated with or without PVP-coated silver chloride nanoparticles in the presence or absence of protein within the cell culture media. The control was not treated with nanoparticles and showed a normal cell morphology under the different conditions (Figure 37 A and B). In contrast, an

incubation with 2.0 µg mL^{-1} silver chloride nanoparticles for one day had a strongly different outcome.

Culturing nanoparticles in RPMI-containing FCS and incubation with 2.0 µg mL^{-1} silver chloride for 24 h seemed to have no impact on the hMSCs compared to the control (Figure 37 C). On the other hand, excluding FCS incubated with 2.0 µg mL^{-1} AgCl nanoparticles for one day had a strong effect. In all three trials, no viable hMSCs were observed under these conditions (Figure 37 D). The quantification of these data is summarized in Figure 38.

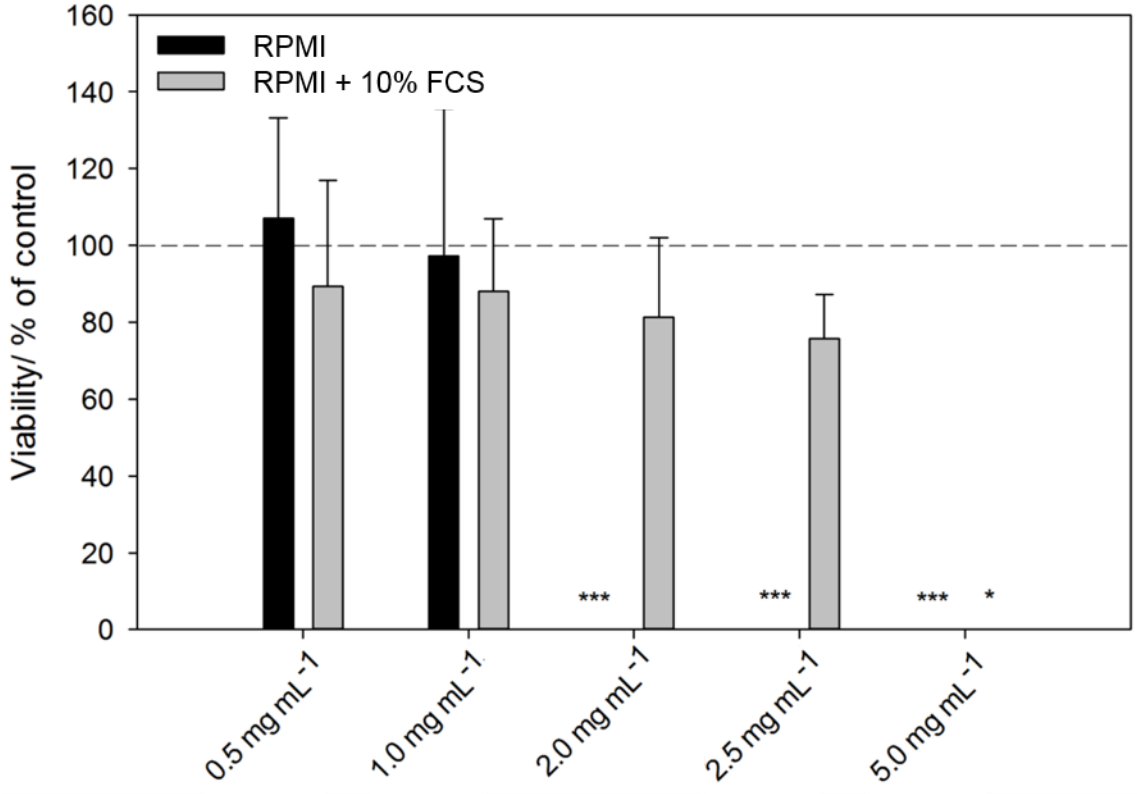

Figure 38. Viability of human mesenchymal stem cells in the presence of AgCl-PVP nanoparticles. The cells were cultured for 24 h with different concentrations of silver chloride nanoparticles in the presence (grey bars) or absence (black bars) of 10% FCS within the cell culture medium RPMI 1640. Incubations without silver served as controls (100%). Living cells were stained by calcein-AM and the fluorescence signals were

quantified by digital image processing (phase analysis). Data are expressed as mean SD (*N*=3 independent experiments). * Significant compared to control ($p<0.05$).

The question of silver protein complexes remains unclear. Because of the complexity of biological systems, there are many possibilities for binding silver. The stability of silver (I) complexes varies with the ligand donor atom: N<<P>As>Sb; O<<S~Se~Te; F<Cl<Br<I, and Ag (I) has been categorized as a "soft" acid.[149] Although it binds most strongly to P and S donor ligands, it has an extensive coordination chemistry with N (in particular) and O donors, and appears to bind to almost every biological molecule tested.[149] Silver (I) has long been known to form complexes with amino acids.[149] It is used to stain proteins in polyacrylamide gels, being more sensitive than staining based on Coomassie Blue techniques. When various polyaminoacids were tested, polyhistidine was stained the most.[150] In certain proteins, silver has been shown to bind at specific sites, forming Ag_6, Ag_{12} and Ag_{18} clusters with a rabbit metallothionein.[151] Because silver (I) tends to complex with so many molecules, it is obviously important to consider which interactions may occur between the medium and added $AgNO_3$. A decreased biocidal activity in certain media was observed by those working on water sterilization.[152-154] The effects of different nutrient media have been specifically investigated.[155] Two silver (I) phosphine complexes exhibited antifungal activity in a defined medium, which was lost in a serum-rich medium, and the toxicity of one of these complexes toward tumor cells *in vitro* was reduced by a factor of five by the presence of fetal calf serum in the medium.[156] The biological effect of PVP-stabilized silver nanoparticles and silver ions on human mesenchymal stem cells was studied in pure RPMI and also in RPMI - BSA and RPMI - FCS mixtures, respectively. Both components considerably increased the cell viability in the presence of silver ions as well as silver nanoparticles, indicating binding of silver by these proteins.[117] These effects were attributed to the reaction with serum and other components of the media.[117, 156]

5.4 Characterization of barium sulfate particles

Barium sulfate in particulate form is often used as a filler system in coatings (*e.g.,* in motor vehicles) due to its mechanical, optical and chemical properties. Lately, $BaSO_4$ nanoparticles have also been implemented in orthopedic medicine, diagnostic imaging and other applications.[157-161] Pellethane with integrated $BaSO_4$ nanoparticles showed antimicrobial properties *in vitro*.[162] An exposure to aerosolized $BaSO_4$ particles may occur during their production, transport, handling, and incorporation into end products, as well as during the use and disposal of those products. Chronic exposure to high levels of $BaSO_4$ microparticles may induce pneumoconiosis (baritosis) in miners.[9, 10, 163] However, an accurate characterization of the barium sulfate particles used is strongly recommended.[27] It should include physico-chemical data not only of primary particles, but of the secondary formed aggregates after the preparation route or during interaction with components of biological media.[63] In contrast, for toxicological studies, barium sulfate particles were used with primary particles in the nanoscale range added as powder with an agglomerate size in the of micrometer range.[63, 164-166] It may underrate the possible biological responses. To investigate the precise cellular reaction to barium sulfate, micro-, sub-micro- and nanoparticles were synthesized. To make the tracking of engineered particles possible, a fluorophore was added. Subsequently, an explicit characterization was performed to establish a model for toxicologically inert particles.

5.4.1 Characterization of barium sulfate microparticles

$BaSO_4$ microparticles were synthesized by precipitation of Na_2SO_4 and $Ba(OH)_2$. The feeding of a precursor was performed by a peristaltic pump. Carboxymethylcellulose conjugated with 6-aminofluorescein (CMC-F) was used as capping agent. Before analysis, the dispersion was purified by ultracentrifugation and then redispersed in pure water. In this way excess CMC-F and by-products were separated. The samples were stored at 4 °C.

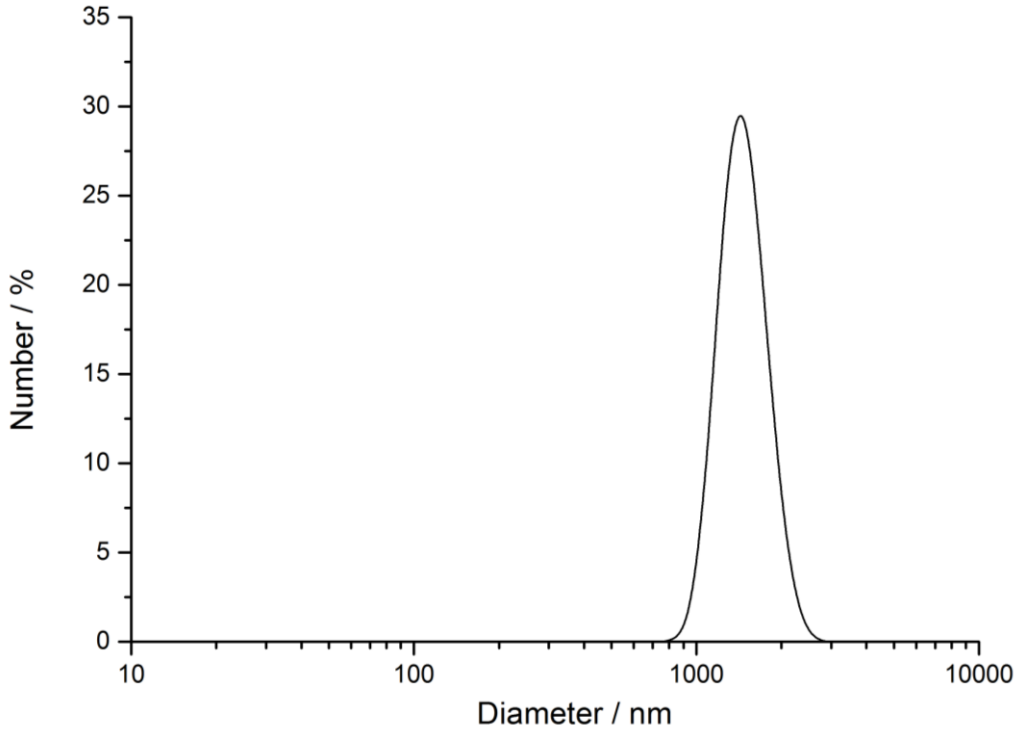

Figure 39: Particle size distribution of CMC-F-coated $BaSO_4$ microparticles as measured by dynamic light scattering.

The hydrodynamic diameter of barium sulfate microparticles was measured by dynamic light scattering. Figure 39 shows the particle size distribution in water. The mean particle diameter was about 1480 nm. The polydispersity index (PDI) was 0.079 and indicates a monodisperse colloid. The particles were negatively charged with a measured zeta potential of -35 mV. A zeta potential different from zero revealed the electrostatic nature of colloid stability.

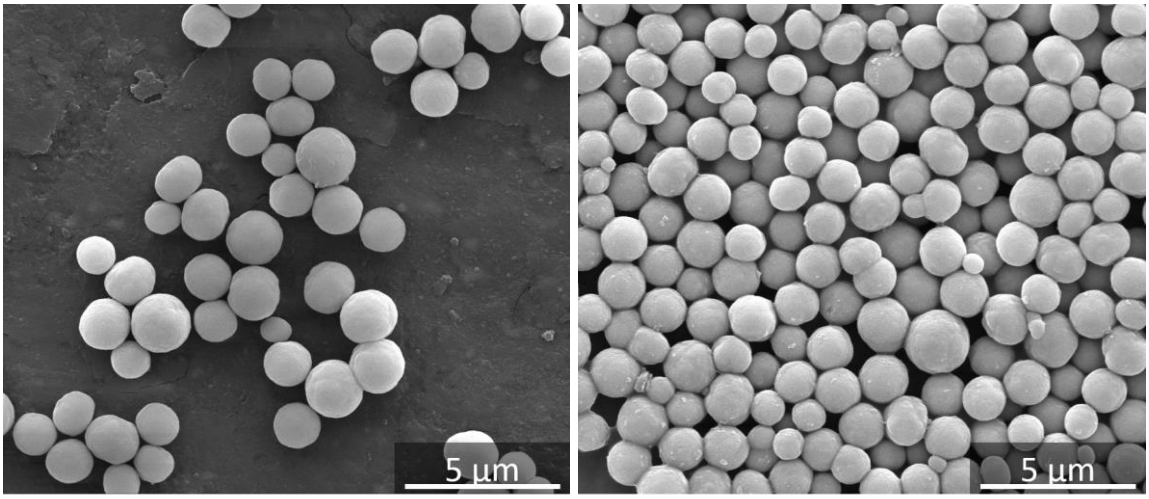

Figure 40: Scanning electron microscopy images of CMC-F-coated $BaSO_4$ microparticles.

Scanning electron micrographs for barium sulfate (Figure 40) showed spherical micro-particles. For the estimation of particle size, individual spherical particles were analyzed and the results are shown as a histogram (Figure 41). The mean particle size assessed by scanning electron microscopy was 1300±210 nm. There was only a slight difference between particle diameters measured by dynamic light scattering and electron microscopy.

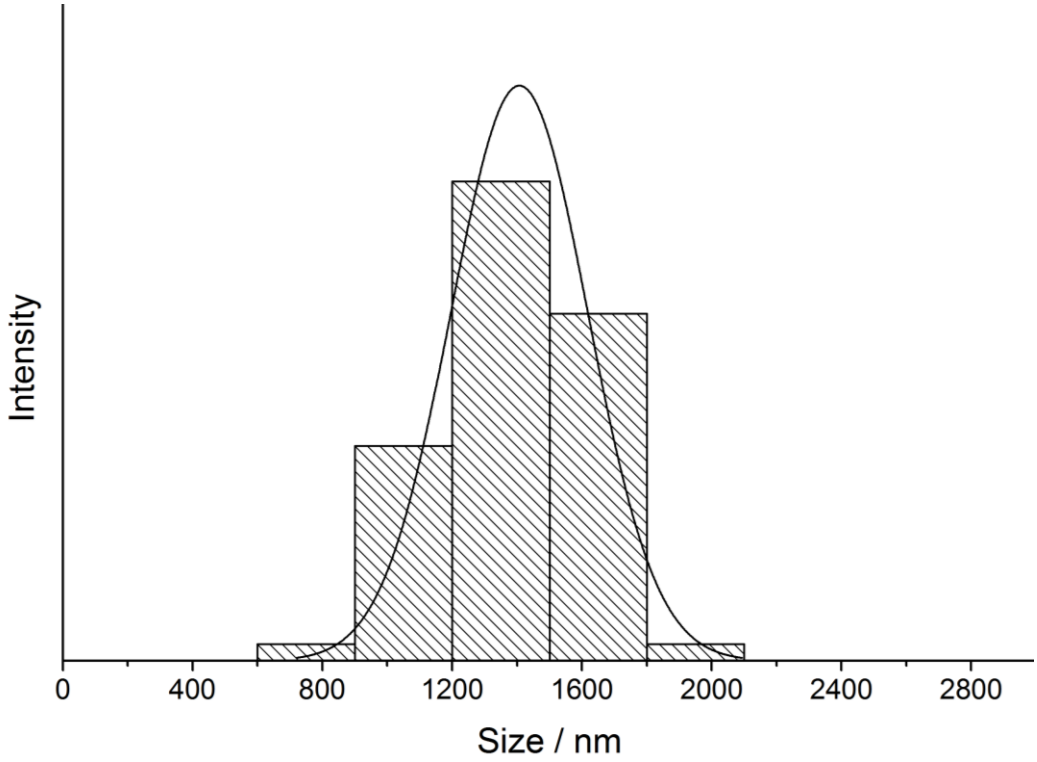

Figure 41: Particle size distribution of CMC-F-coated $BaSO_4$ microparticles as measured by scanning electron microscopy.

Energy-dispersive X-ray spectroscopy detected signals of barium, sulfur and oxygen (Figure 42). The peak of silicon resulted from the substrate, *i.e.* a silicon wafer. The carbon peak corresponded to carboxymethylcellulose. There were no other signals detected.

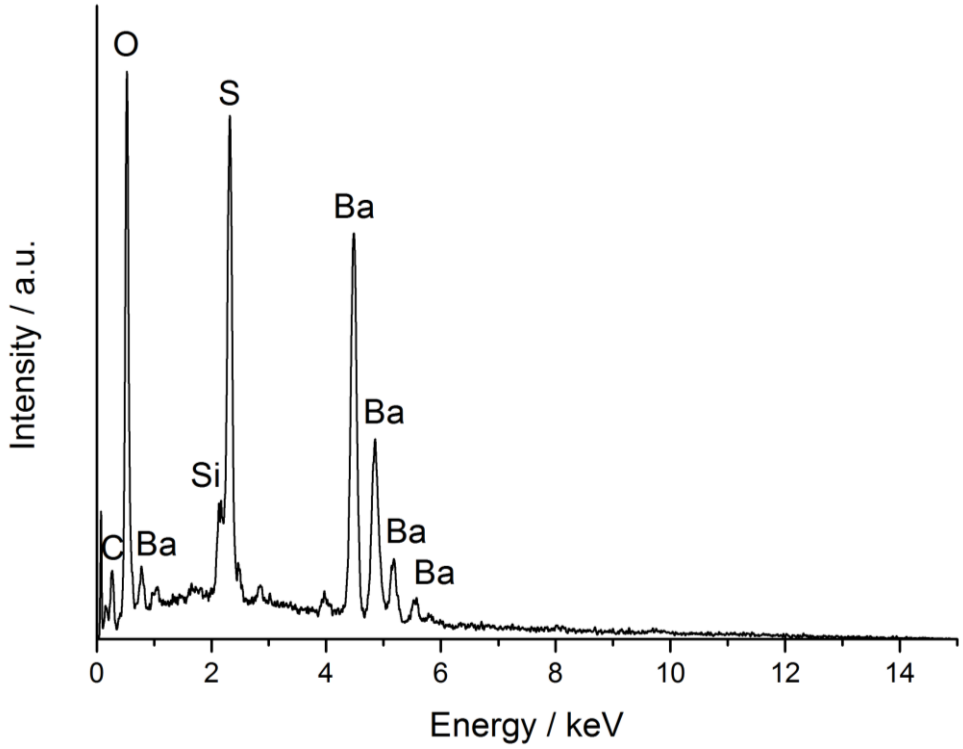

Figure 42: Energy-dispersive X-ray spectrum of CMC-F-coated $BaSO_4$ microparticles.

Identity and crystallinity of the substances were confirmed using X-ray powder diffraction. All materials crystallized in the orthorhombic barite phase. Figure 43 shows representative X-ray diffractogram of CMC-F-coated barium sulfate microparticles. All of the peaks were readily indexed to a pure orthorhombic crystalline phase of $BaSO_4$, which was in good agreement with the literature (PDF No. 00-24-1035). However, the received patterns were typical for nanocrystalline materials due to the broadening of diffraction peaks. To prove the suggestion, the crystallite size was estimated. The size of the crystallites was calculated with the Scherrer equation:

$$D = \frac{K \cdot \lambda}{FWHM \cdot cos\theta}$$

with *K* being a constant set to 0.89, *λ* denoting the wavelength of the X-ray radiation, *FWHM* corresponding to the full width at half maximum for the diffraction peaks and

θ being the diffraction angle. The calculated crystallite size of CMC-F-coated barium sulfate microparticles was around 19 nm. By evaluating the calculated crystallite size and particle size by scanning electron microscopy, the individual microparticles were polycrystalline. A long-term ultrasonication did not result in the disintegration of synthesized CMC-F-coated $BaSO_4$ microparticles.

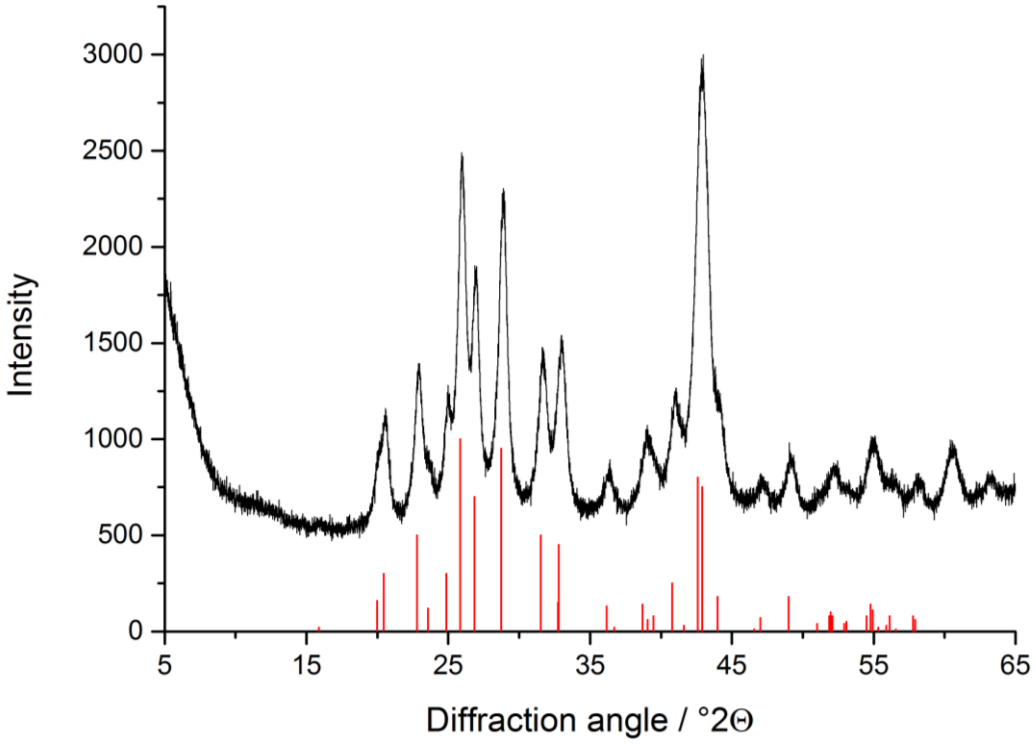

Figure 43: Representative X-ray powder diffractogram of CMC-F-coated $BaSO_4$ microparticles. The red bars correspond to the orthorhombic barite phase.

For quantification of the polymer content in CMC-F-coated $BaSO_4$ microparticles, a thermogravimetric analysis was performed (Figure 44). Prior to the measurement, the dispersion of barium sulfate microparticles was dried in air. The experiments were carried out in a dynamic oxygen atmosphere at a heating rate of 2 K min^{-1} in alumina crucibles. The sample was heated to 1000 °C. In this temperature interval, only the organic part was effected, because a decomposition of barium sulfate starts only at 1422 K.[167] The polymer content of CMC-F-coated $BaSO_4$ microparticles was about 5%.

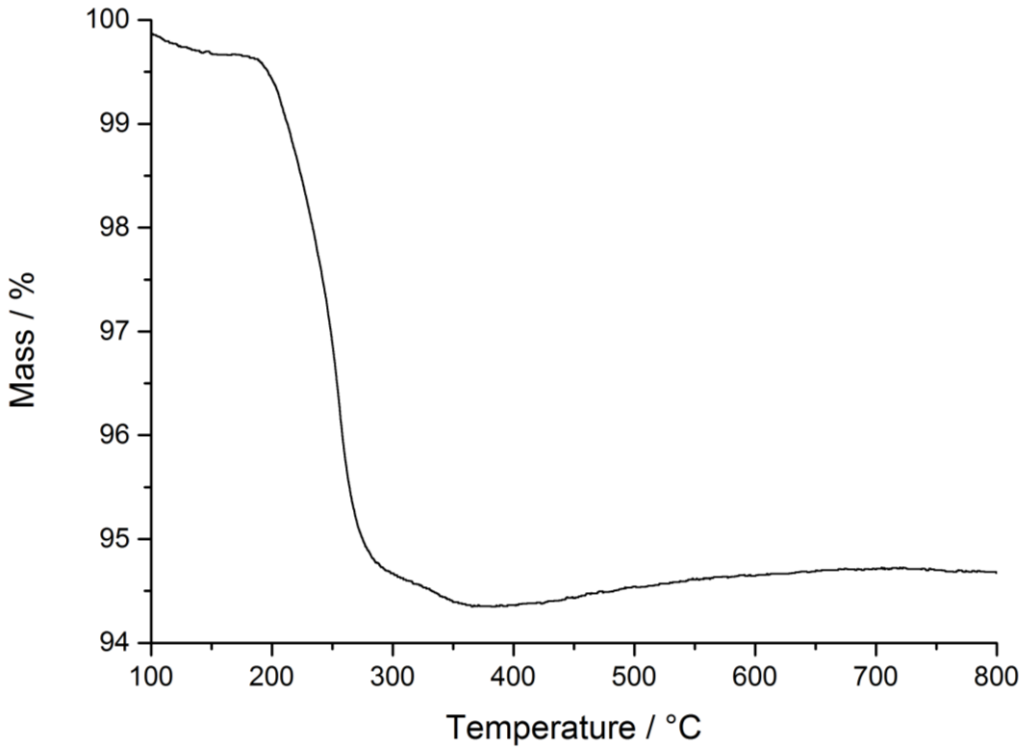

Figure 44: Thermogravimetric analysis of CMC-F-coated $BaSO_4$ microparticles after the sample was dried on air.

As the synthesized CMC-F-coated barium sulfate microparticles were expected to be fluorescent due to the functionalization by carboxymethylcellulose conjugated with 6-aminofluorescein, fluorescence spectroscopy was performed. 6-Aminofluorescein is a fluorophore that is commonly used in microscopy as a marker for numerous applications. Figure 45 shows the emission spectrum of functionalized barium sulfate microparticles. The emission spectrum was characteristic for 6-aminofluorescein for an excitation wavelength 490 nm.

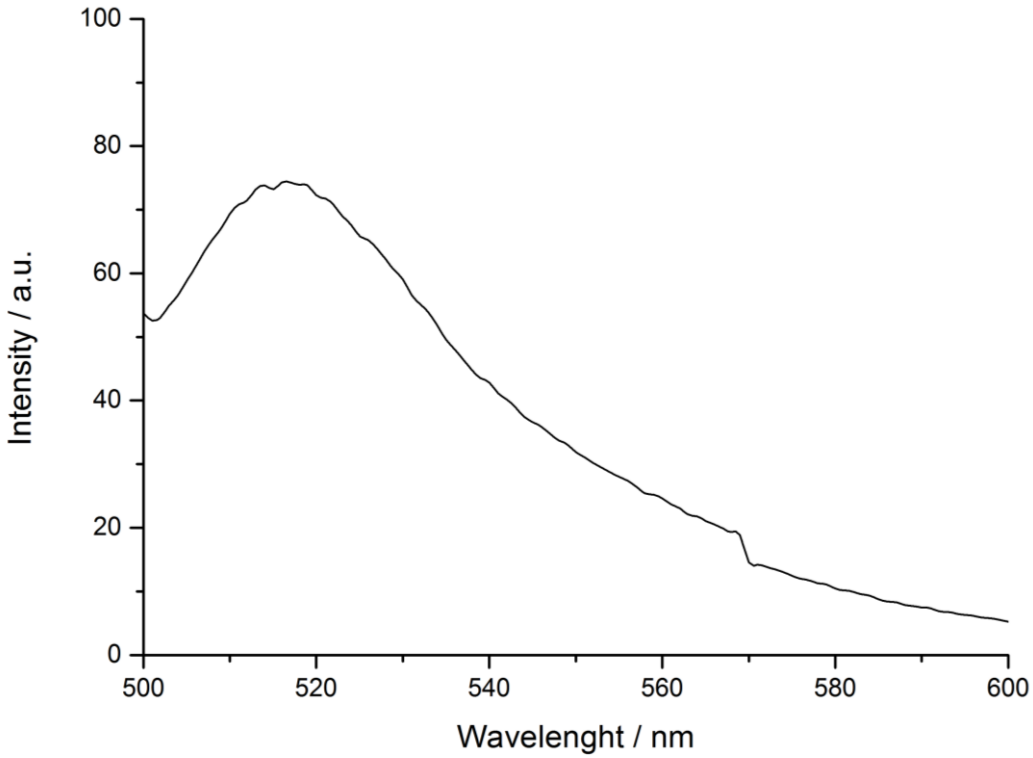

Figure 45: Fluorescence spectrum of CMC-F-coated $BaSO_4$ microparticles; excitation wavelength 490 nm.

Figure 46 shows fluorescently-labelled $BaSO_4$ microparticles. The image was processed by providing an overlay of light and fluorescence microscopy; the excitation wavelength was 490 nm. Before imaging, the particles were dried on a glass slip. The functionalized microparticles were shown in green.

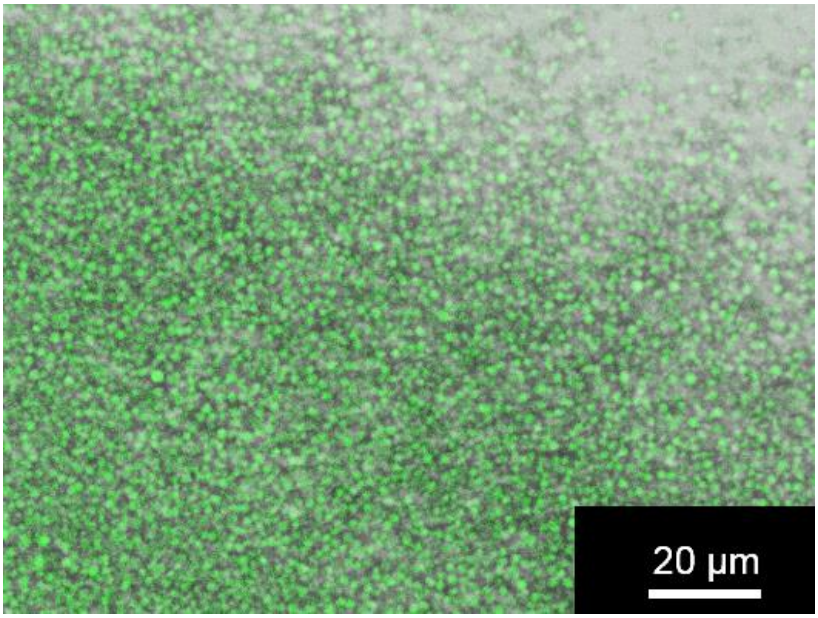

Figure 46: Fluorescently labelled $BaSO_4$ microparticles are shown in green. The image is an overlay of light and fluorescence microscopy; excitation wavelength 490 nm.

The *in situ* observation of the colloidal particle stability is shown in Figure 47. All samples were well dispersable in cell culture medium. The colloidal stability of particles was determined by dynamic light scattering. The average particle size was determined over time. Due to their size, barium sulfate microparticles sedimented over a few hours of incubation in cell culture media supplemented with serum. However, after gentle shaking, the particles were easily dispersible again. No agglomerates were observed. The sedimentation and aggregation of a particulate system can be a crucial point in biological tests *in vitro*, while the bioavailability of the sample may vary for different cell lines (*e.g.,* adherent or suspension cell cultures).[168]

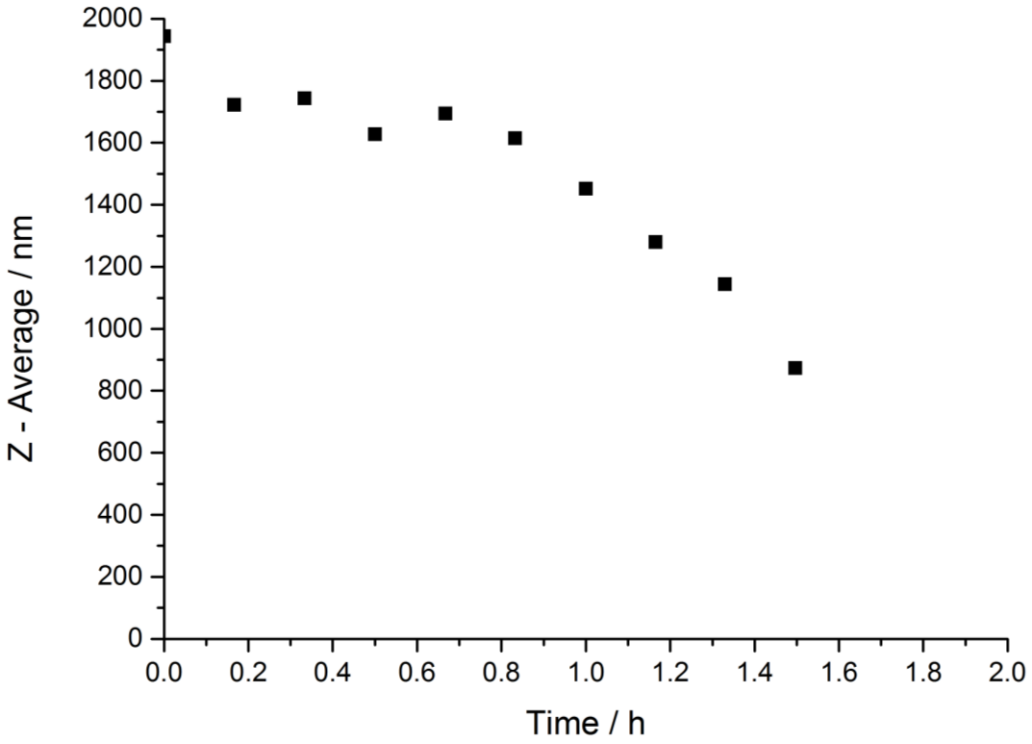

Figure 47: Colloidal stability of synthetic CMC-F-coated barium sulfate microparticles in DMEM + 10% FCS medium at 37 °C under sterile condition.

5.4.2 Characterization of barium sulfate sub-microparticles

$BaSO_4$ sub-microparticles were synthesized by the precipitation of Na_2SO_4 and $Ba(OH)_2$. The feeding of a precursor was performed by a peristaltic pump. Carboxymethylcellulose conjugated with 6-aminofluorescein (CMC-F) was used as a capping agent. Before analysis, the dispersion was purified by ultracentrifugation and then redispersed in pure water. In this way, CMC-F excess and by-products were removed. The samples were stored at 4 °C. An important variation in barium sulfate microparticle and sub-microparticle synthesis was the implementation of a Y-connector. This mixing procedure is often called impinging streams.[169-171] A perfect mixing can be realized within an extremely short time.[172] Using this advantage, inorganic submicron materials could be synthesized. The local supersaturation of the reaction system was improved which resulted in a particle size reduction. These statements were proved by the physico-chemical characterization of the synthesized sub-microparticles.

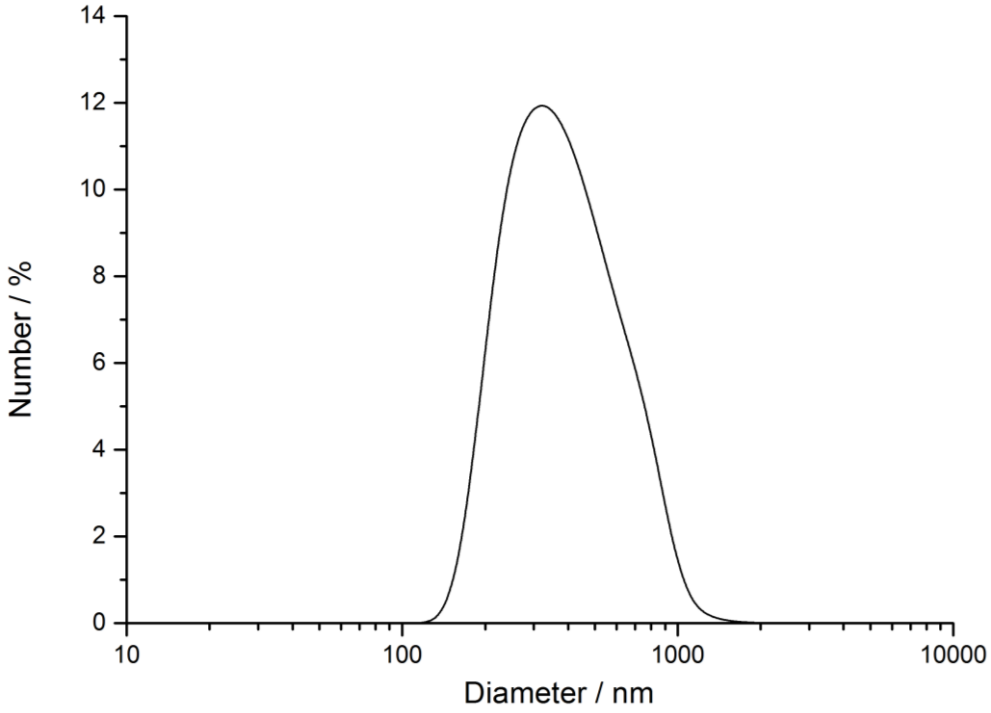

Figure 48: Particle size distribution of CMC-F-coated $BaSO_4$ sub-microparticles as measured by dynamic light scattering.

The hydrodynamic diameter of barium sulfate sub-microparticles was measured by dynamic light scattering. Figure 48 shows the particle size distribution in water. The mean particle diameter was about 420 nm. The polydispersity index (PDI) was 0.181. The particles were negatively charged with a zeta potential of -26 mV.

Morphological studies were performed on a dried suspension of purified CMC-F-coated barium sulfate sub-microparticles by scanning electron microscopy. Figure 49 shows typical micrographs for $BaSO_4$ powders synthesized by impinging streams. The formed objects possessed a regular elliptical morphology.

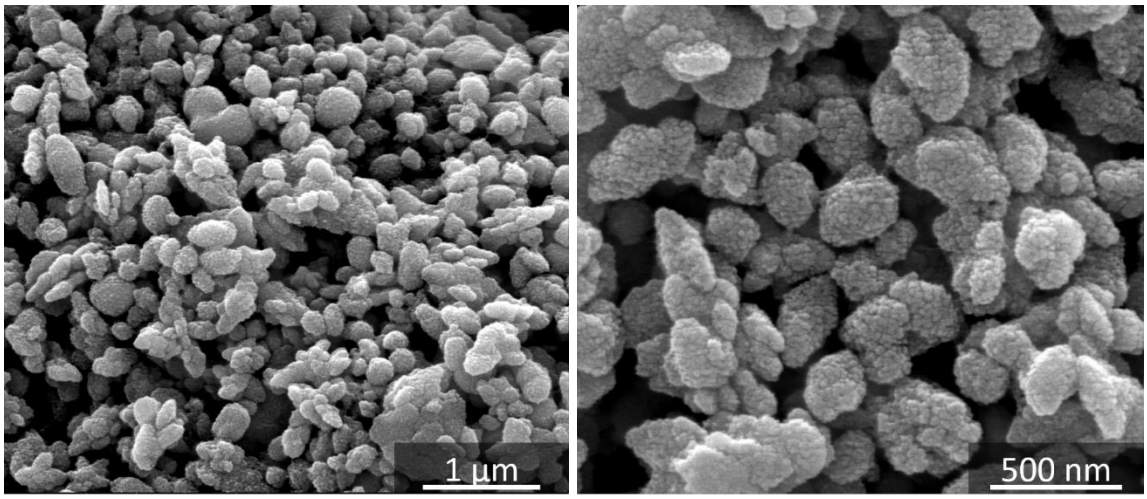

Figure 49: Scanning electron microscopy images of CMC-F-coated $BaSO_4$ sub-microparticles.

The particle size distribution of dried samples was estimated by measuring individual particles. These results were plotted as a histogram. Figure 50 shows a monomodal particle size distribution with a mean particle diameter of 270 nm. A possible minor agglomeration could be one reason for the observed difference in size distribution by dynamic light scattering and electron microscopy. While the differential scattering

cross-sections are proportional to the 6th power of particle size, distributions by intensity of non-ideal disperse dispersions generally give larger particle diameters.

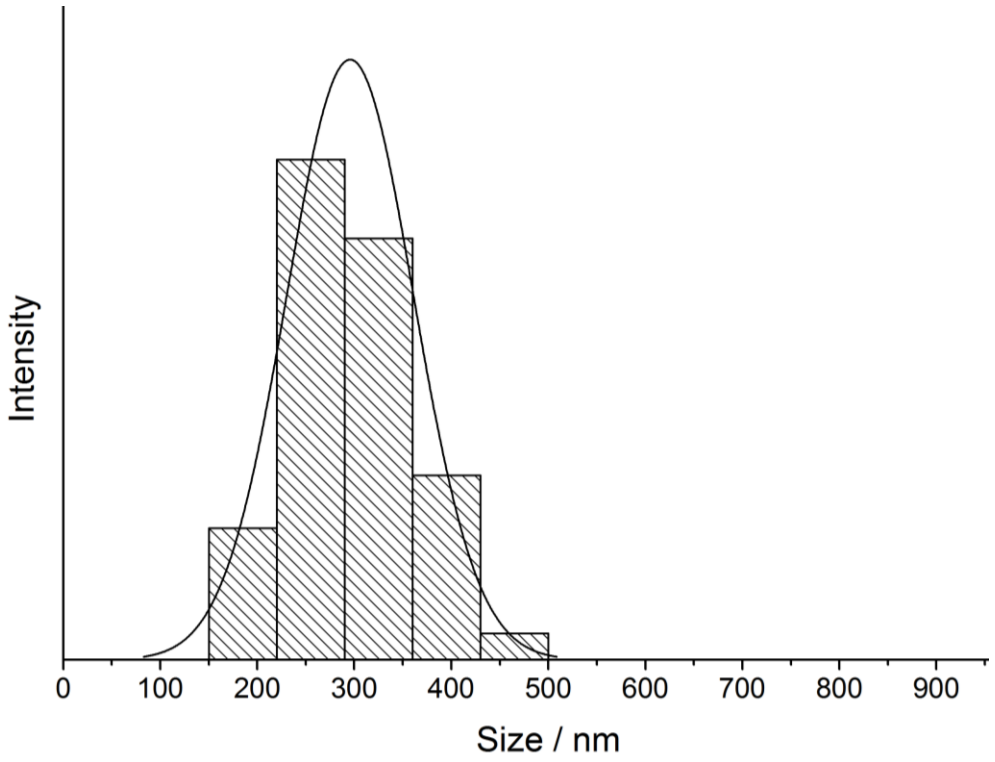

Figure 50: Particle size distribution of CMC-F-coated $BaSO_4$ sub-microparticles as measured by scanning electron microscopy.

Elemental analysis was performed by energy-dispersive X-ray spectroscopy. Figure 51 shows a representative spectrum for CMC-F-coated $BaSO_4$ sub-microparticles. The results showed the presence of barium, sulfur, and oxygen. The peak of silicon resulted from the substrate, and the carbon peak is due to carboxymethylcellulose used as a capping agent.

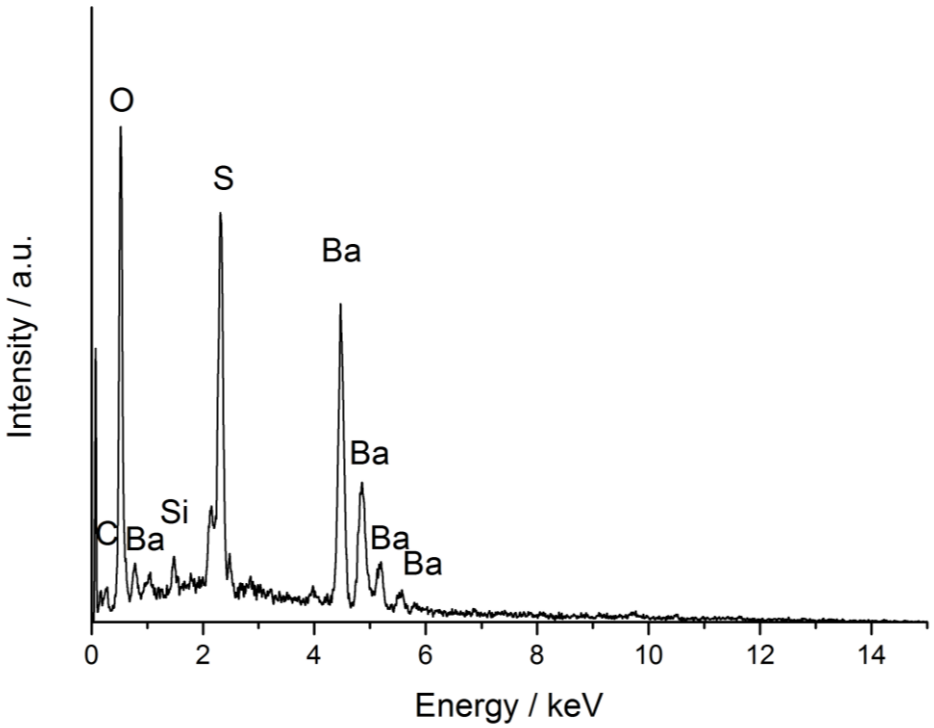

Figure 51: Energy-dispersive X-ray spectrum of CMC-F-coated $BaSO_4$ sub-microparticles.

For the quantification of organic matrix content in CMC-F-coated $BaSO_4$ sub-microparticles, thermogravimetric analysis was performed (Figure 52). Prior to measurement, the dispersion of barium sulfate sub-microparticles was dried on air. The experiments were carried out in a dynamic oxygen atmosphere at a heating rate of 2 K min^{-1} in alumina crucibles. During thermogravimetric examination, the sample was heated up to 1000 °C. The polymer content of CMC-F-coated $BaSO_4$ sub-microparticles was about 3%.

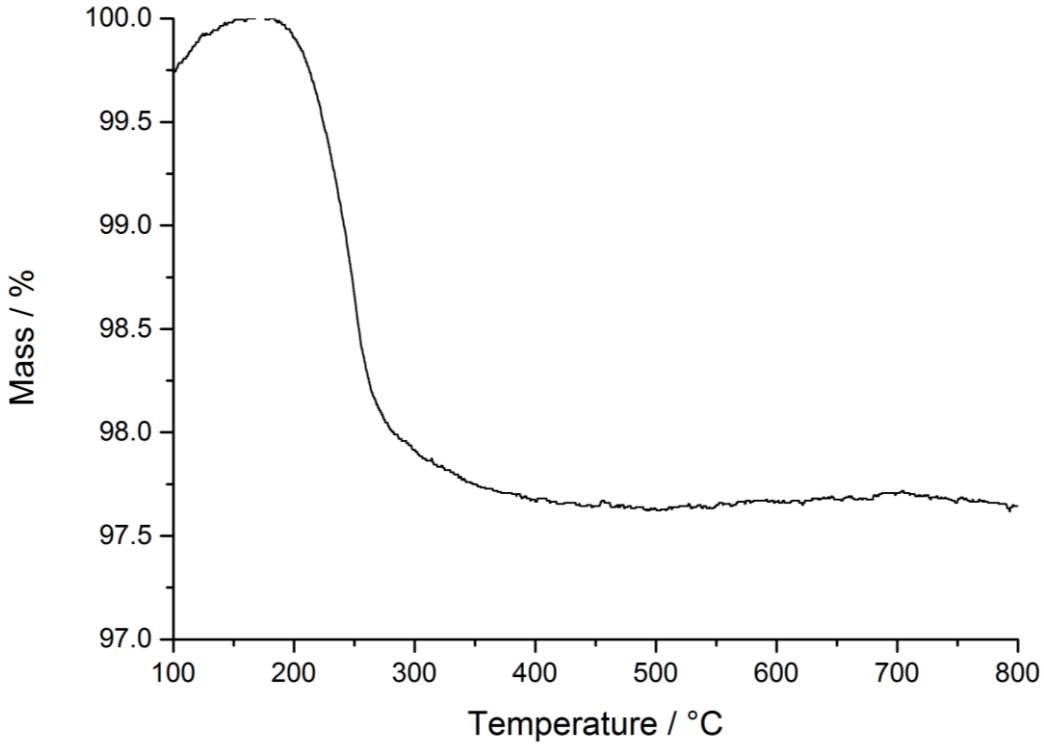

Figure 52: Thermogravimetric analysis of CMC-F-coated $BaSO_4$ sub-microparticles after sample was dried on air.

For the identification and characterization of crystalline solids, X-ray powder diffraction was used. Figure 53 shows a representative X-ray diffractogram of CMC-F-coated barium sulfate sub-microparticles. The measurements were performed on dried purified powders. All of the peaks can be readily indexed to a pure orthorhombic crystalline phase of $BaSO_4$ (PDF No. 00-24-1035). The crystallite size was estimated with the Scherrer equation and found to be around 124 nm. However, the particle size distribution by scanning electron microscopy gave a mean particle diameter of 270±65 nm.

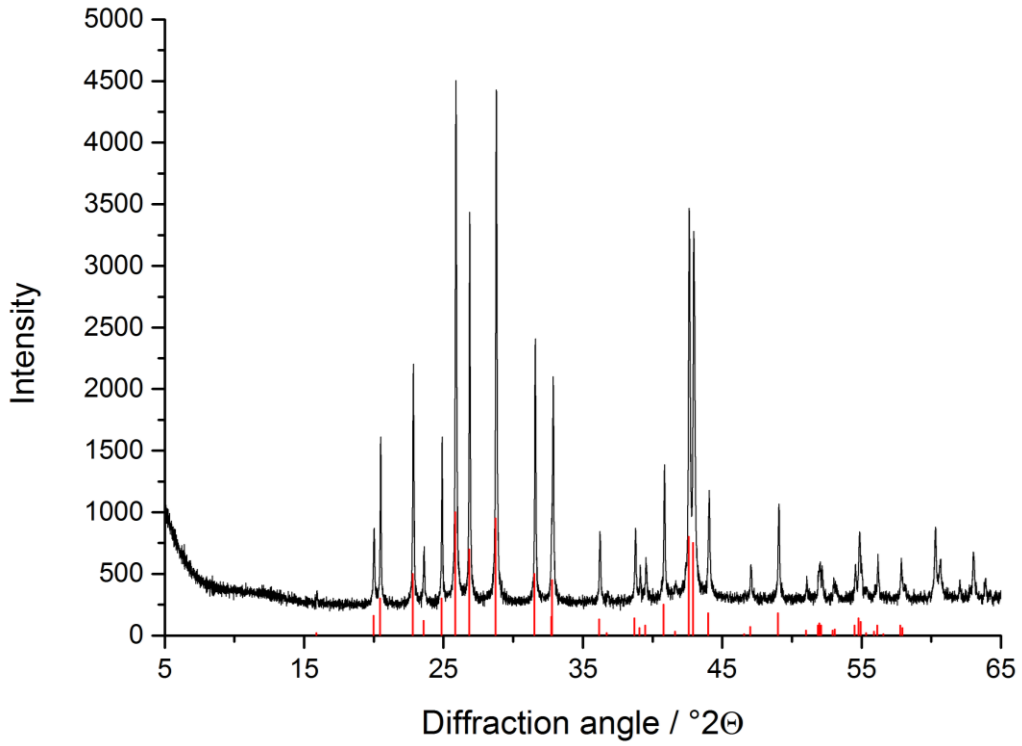

Figure 53: Representative X-ray powder diffractogram of CMC-F-coated $BaSO_4$ sub-microparticles. The red bars correspond to the orthorhombic barite phase.

The *in situ* observation of particle stability is shown in Figure 54. All samples were well dispersable in DMEM medium supplemented with 10% fetal calf serum at 37 °C to mimic cell culture experiments. The colloidal stability of particles was determined by dynamic light scattering. The average particle size was measured over time. The results were plotted as a z-average against the time of incubation (Figure 54). Barium sulfate sub-microparticles showed no significant difference in aggregation behavior during incubation in cell culture media with serum under sterile conditions over 10 h. No agglomerates were observed. Such a performance indicates a sufficient bioavailability of particulate system to cell culture suspensions in *in vitro* investigations.

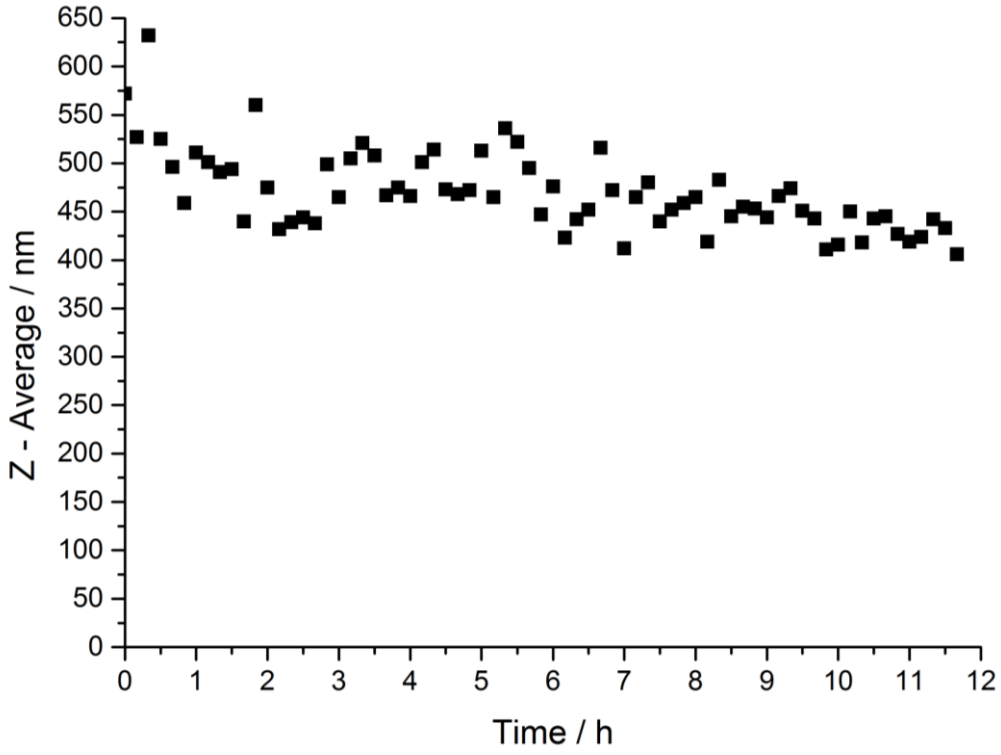

Figure 54: Colloidal stability of synthetic CMC-F-coated barium sulfate sub-microparticles in DMEM + 10% FCS medium at 37 °C under sterile condition.

5.4.3 Characterization of barium sulfate nanoparticles

Fluorescent barium sulfate nanoparticles were synthesized by precipitation from solutions of barium chloride and sodium sulfate in the presence of carboxymethylcellulose conjugated with 6-aminofluorescein. Many different approaches have been employed in the manufacture of well-dispersed $BaSO_4$ nanoparticles.[169, 173-186] In the current report, the $BaSO_4$ nanoparticles were synthesized by co-solvent precipitation in the presence of the polymer as a suitable modifying agent.[180] Sodium sulfate was premixed with ethanol. Barium chloride was also premixed with carboxymethylcellulose conjugated with 6-aminofluorescein. The feeding procedure was performed by pumping sulfate-containing precursor into barium-containing solution. The feeding rate was around 4 µL s^{-1}. The particles were collected by ultracentrifugation, redispersed in pure water and collected again by

ultracentrifugation. The barium sulfate nanoparticles were then redispersed in water by ultrasonication. In this way, polymer excess, barium excess and by-products were removed.

Precipitation is a common procedure for the production of particles of different size distributions, morphologies, and other properties.[187-190] The product properties are affected by various interconnected parameters like mixing, nucleation, growth, and processes such as agglomeration, aggregation, or ripening.[186, 190-196] In our case, the use of a Y-connector reduced the particle size from micrometers down to ca. 300 nm. A further reduction of nucleation time did not have an effect. In this study, $BaSO_4$ nanoparticles were prepared by co-solvent precipitation in the presence of carboxymethylcellulose as suitable functionalizing agent. The previously described procedure was modified by pre-mixing of $BaCl_2$ with carboxymethylcellulose. By such treatment of $BaCl_2$ with carboxymethylcellulose, an electrostatic interaction of positively charged barium ions and negatively charged carboxymethylcellulose polymer chains may occur. This led to a decrease in freely available barium cations in the solution. Together with a slow feeding rate of sulfate ions, it results in nanosized particles. Moreover, the steric interference of carboxymethylcellulose on the surface of $BaSO_4$ nanoparticles reduced the particle-particle interactions and limited the growth of larger agglomerates.

The hydrodynamic diameter of barium sulfate nanoparticles was measured by dynamic light scattering. Figure 55 shows the particle size distribution in water. The mean particle diameter was about 70 nm. A secondary peak was also detected, possibly as a redispersion artifact. The polydispersity index (PDI) was 0.253. The particles were negatively charged with a measured zeta potential of -23 mV. It showed the electrosteric nature of colloid stability.

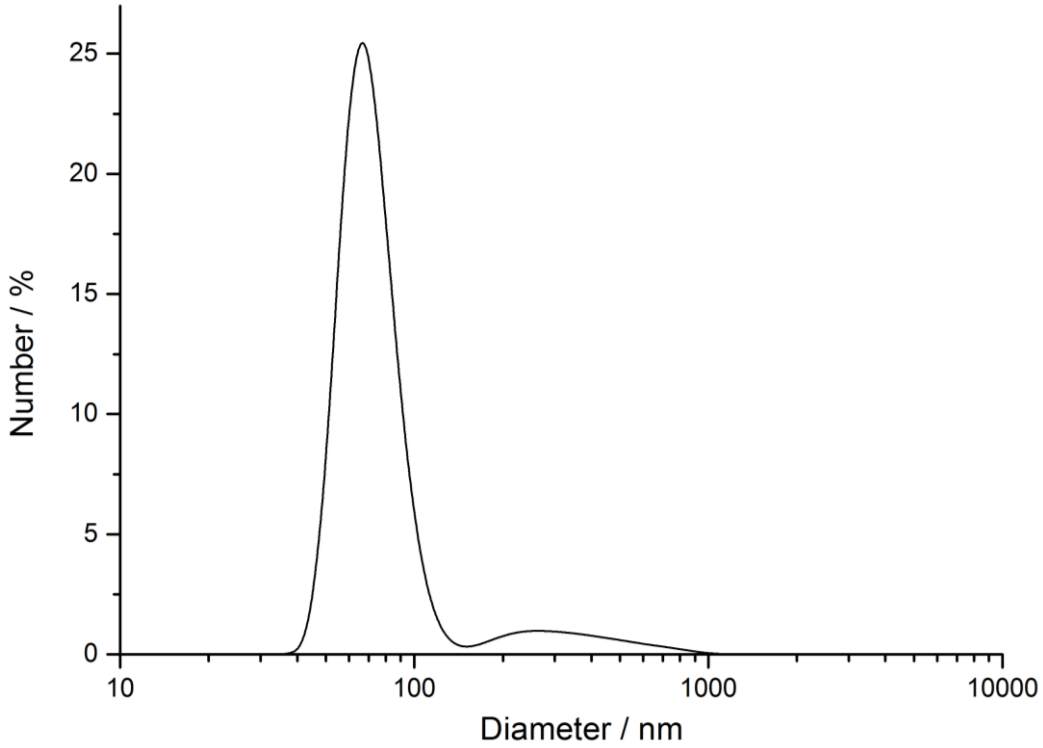

Figure 55: Particle size distribution of CMC-F-coated $BaSO_4$ nanoparticles as measured by dynamic light scattering.

Scanning electron micrographs for barium sulfate (Figure 56) showed regular spherical nanoparticles. The individual spherical particles were analyzed, and the results are shown as histogram. Figure 57 shows a narrow monomodal particle size distribution of the dried sample. The mean particle size assessed by scanning electron microscopy was 40±7 nm. The particle diameter measured by dynamic light scattering and electron microscopy was different, while the slight agglomeration of particles in solution occurred after double ultracentrifugation.

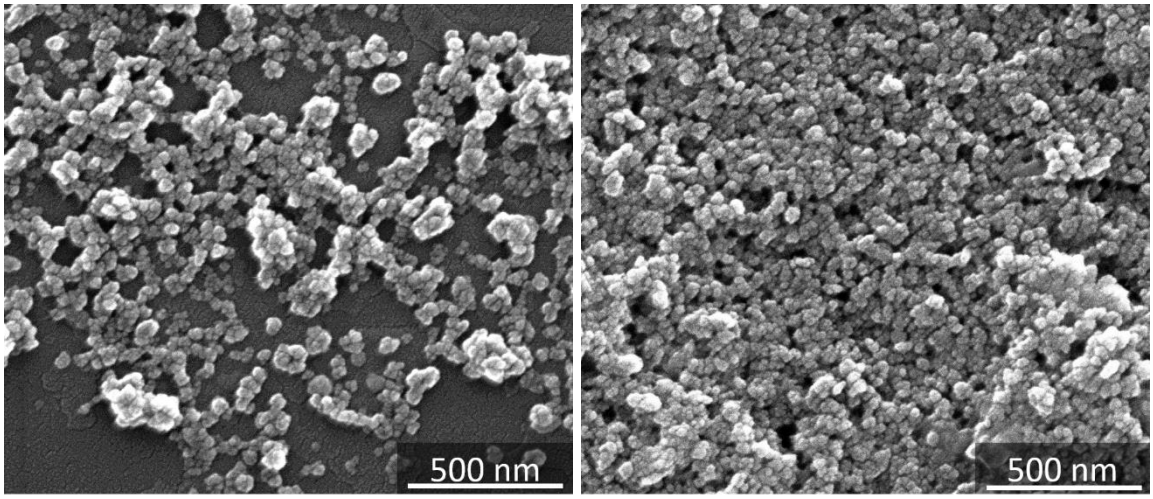

Figure 56: Scanning electron microscopy images of CMC-F-coated $BaSO_4$ nanoparticles.

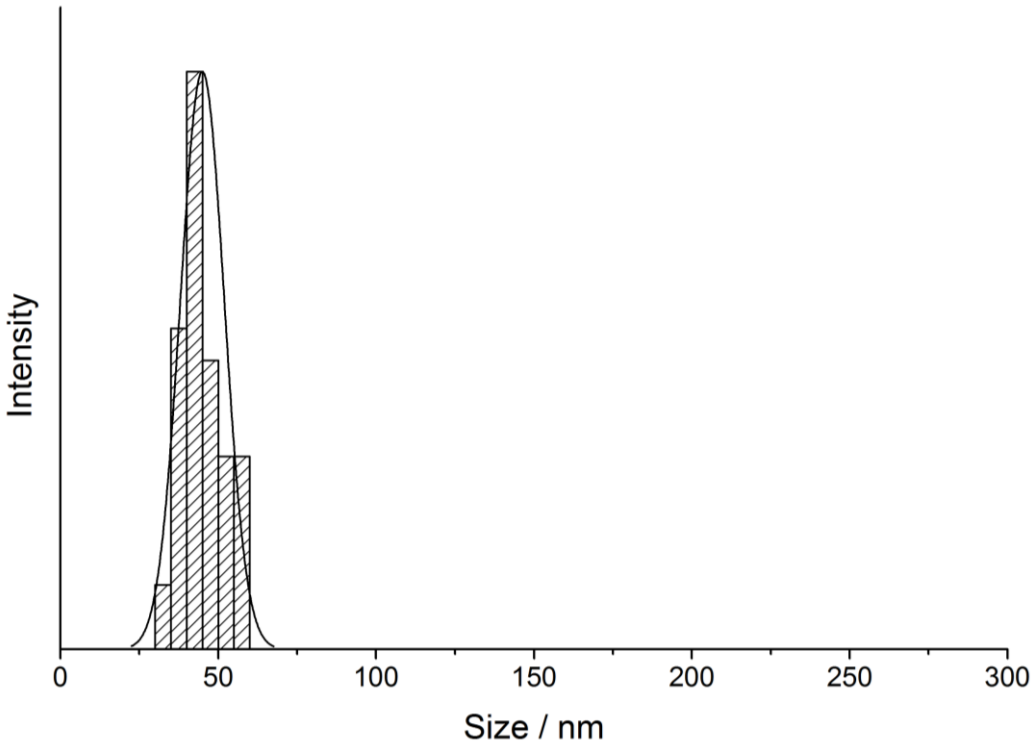

Figure 57: Particle size distribution of CMC-F-coated $BaSO_4$ nanoparticles as measured by scanning electron microscopy.

Energy-dispersive X-ray spectroscopy detected signals of barium, sulfur and oxygen. Typical spectrum is shown in Figure 58. The peak of silicon is due to the substrate. The carbon peak was corresponded to the carboxymethylcellulose polymer.

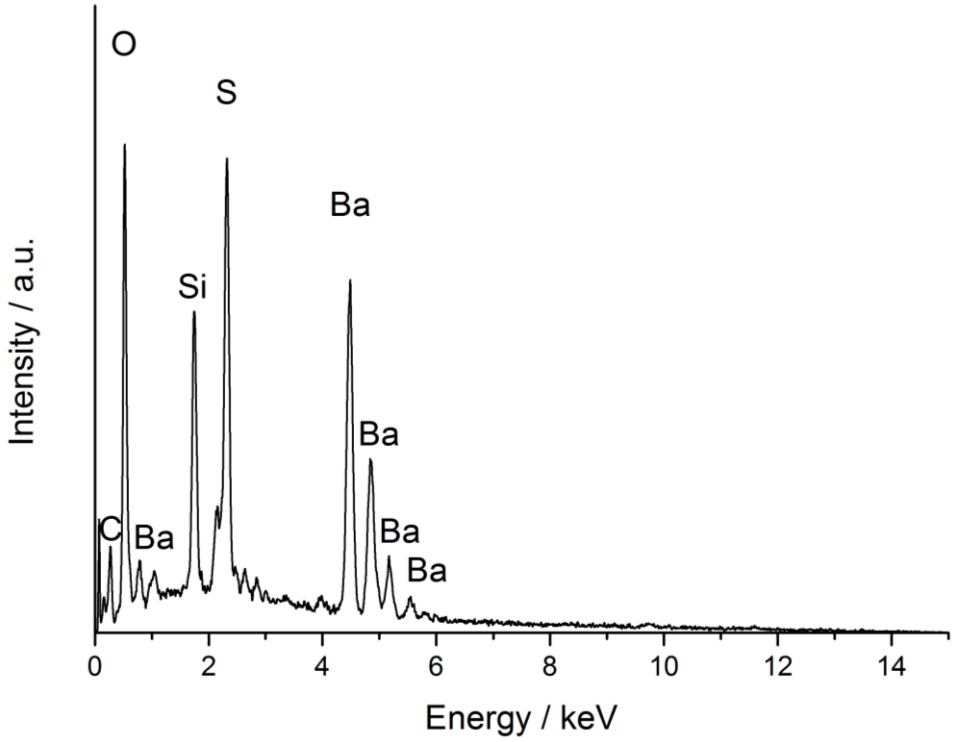

Figure 58: Energy-dispersive X-ray spectrum of CMC-F-coated $BaSO_4$ nanoparticles.

For quantification of the organic matrix content in CMC-F-coated $BaSO_4$ nanoparticles, thermogravimetric analysis was performed (Figure 59). Prior to measurement, the dispersion of barium sulfate nanoparticles was dried on air. The experiments were carried out in a dynamic oxygen atmosphere at a heating rate of 2 K min^{-1} in alumina crucibles. During thermogravimetric examination, the sample was heated to 1000 °C. The decomposition of barium sulfate starts only at 1422 K.[167] The polymer content of CMC-F-coated $BaSO_4$ nanoparticles was about 15%.

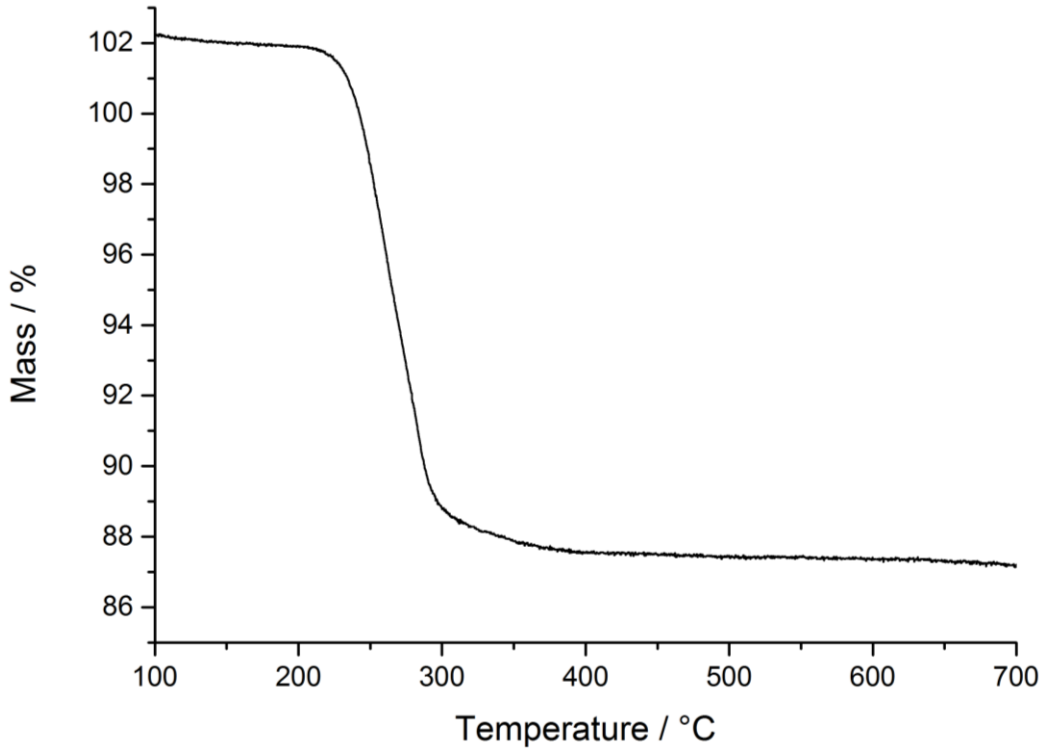

Figure 59: Thermogravimetric analysis of CMC-F-coated $BaSO_4$ nanoparticles in a dynamic oxygen atmosphere.

To prove the crystalline nature of the produced particles and identify the crystallographic phase, X-ray powder diffraction was performed. Figure 60 depicts the representative X-ray diffractogram of CMC-F-coated barium sulfate nanoparticles. The measurements were performed on dried purified powders. All of the peaks were readily indexed to a pure orthorhombic crystalline phase of $BaSO_4$, which was in good agreement with the literature (PDF No. 00-24-1035). Characteristic broadening of diffraction peaks revealed the formation of nanocrystalline precipitate. The crystallite size was estimated with the Scherrer equation. It was found to be around 35 nm. The mean particle size measured by scanning electron microscopy agreed well with the determined crystallite size.

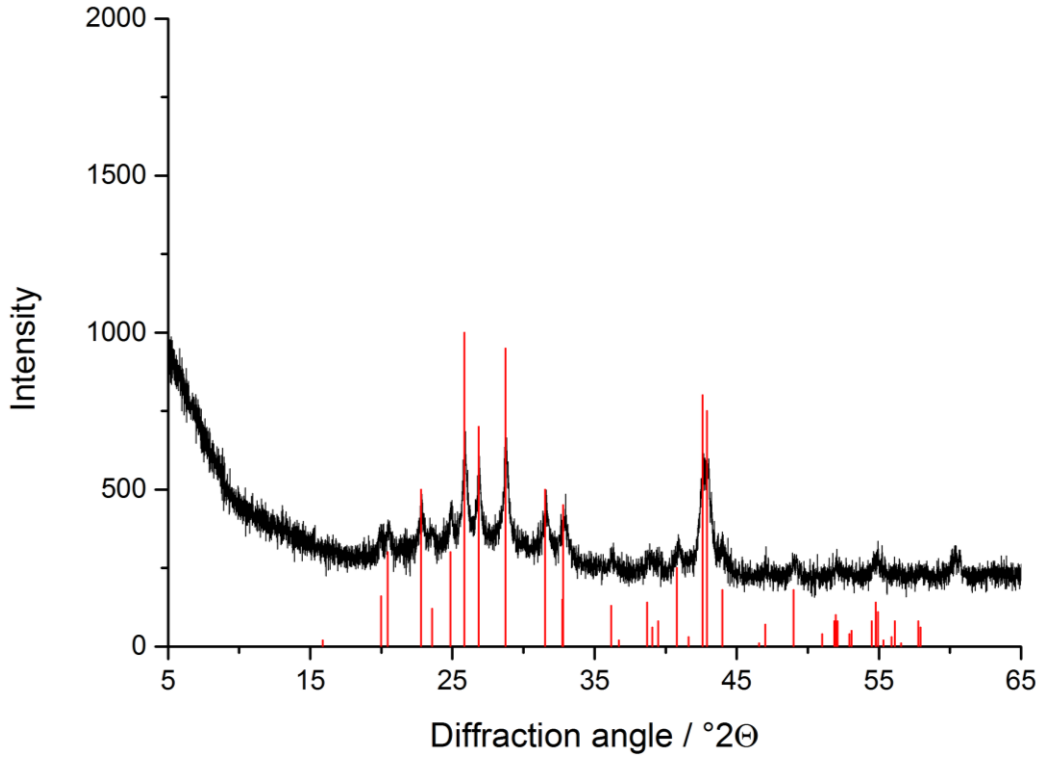

Figure 60: Representative X-ray powder diffractogram of CMC-F-coated $BaSO_4$ nanoparticles. The red bars correspond to the orthorhombic barite phase.

Figure 61 shows fluorescently-labelled $BaSO_4$ nanoparticles. The left image was processed by fluorescence microscopy and the right one by light microscopy. An excitation wavelength was 490 nm. Before imaging, the particles were dried on a cover glass. The functionalized nanoparticles are shown in green. No strong agglomeration of functionalized $BaSO_4$ nanoparticles was observed after double ultracentrifugation.

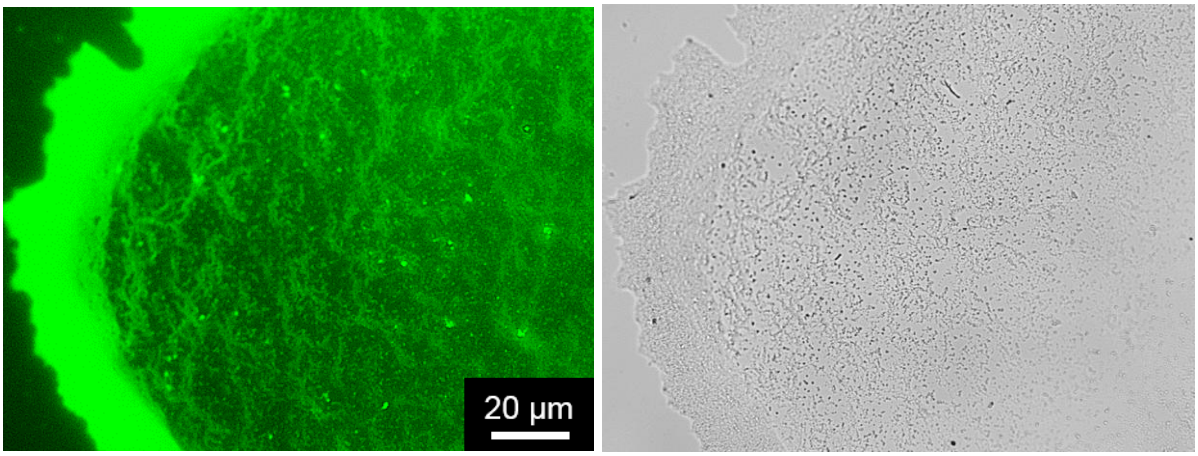

Figure 61: Fluorescently-labelled $BaSO_4$ nanoparticles show up in green. Left: fluorescence microscopy; right: light microscopy; excitation wavelength is 490 nm.

The colloidal stability of produced dispersions was tested in DMEM + 10% FCS (Figure 62). DMEM is a typically used cell medium for the culturing of eukaryotic cells. The experiments were performed under sterile conditions at 37 °C. The evaluation was performed as a control of the hydrodynamic diameter of suspended fluorescently-labelled $BaSO_4$ nanoparticles over time. The graph was plotted as z-average *vs.* time. It is interesting that the initial size of particles in biological medium was not the same as in pure water. Over 10 h, barium sulfate nanoparticles showed no significant difference in aggregation behavior during incubation in cell culture media with serum under sterile conditions.

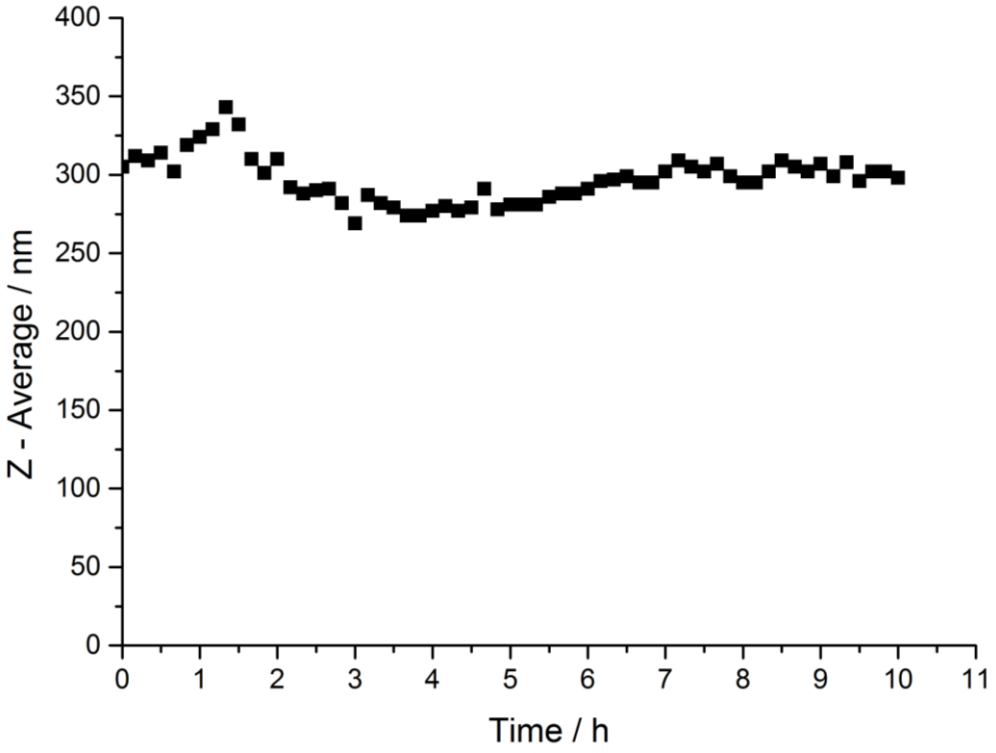

Figure 62: Colloidal stability of synthetic CMC-F-coated barium sulfate nanoparticles in DMEM + 10% FCS medium at 37 °C under sterile condition.

In conclusion, a controlled synthesis of fluorescently-labeled $BaSO_4$ nanoparticles, sub-microparticles and microparticles with a narrow size distribution was achieved. The resultant particles were uniform in shape, chemical composition, and surface modification. All particles were colloidally dispersable in cell culture medium with serum.

Table 7 summarizes the physico-chemical characterization for the synthesized barium sulfate particles. The hydrodynamic diameter of particles was studied by dynamic light scattering. All particles were negatively charged due to functionalization with carboxymethylcellulose. Identity and crystallinity of the substances were confirmed by X-ray powder diffraction. All materials crystallized in orthorhombic barite phase. The size of the crystallites was calculated with the Scherrer equation. By evaluation of the calculated crystallite size and particle size by scanning electron microscopy, it was

notable that microparticles were polycrystalline, whereas nanoparticles presumably consisted of a single domain. The content of the organic matrix was computed from the results of thermogravimetric analysis. The highest polymer amount was found in the case of nanoparticles. Sub-micro and microparticles possessed a comparable quantity of adsorbed carboxymethylcellulose. Size and morphology of the dried dispersion were determined by scanning electron microscopy. The particle number per g was derived by dividing 1 g by the mass of one particle. The particle mass results from the following formula:

$$m_{Particle} = \frac{4}{3}\pi r^3 \rho$$

where *r* is the radius of particle obtained from results of electron microscopy and *ρ* is the density of barium sulfate. The specific surface area was calculated with formula:

$$S = 4\pi r^2 N_{Particles\ per\ 1\ g}$$

The calculated specific surface area for synthesized nanoparticles is in the range of the typical values from literature.[63] In the last column, a typical sample under UV light irradiation (λ=400 nm) after ultrasonication in pure water is shown.

Table 7: Summary of the characterization of synthesized barium sulfate particles.

Barium sulfate	Mean particle diameter by DLS / nm	PDI	Z-Potential / mV	Mean particle diameter by SEM / nm	Crystallite size by XRD / nm	Amount of organic matrix by TG / %	Crystalline phase by XRD	Particle number (calculated) per g	Specific surfaces area (calculated) / m^2g^{-1}	Typical sample imaged under UV light irradiation (λ=400 nm)
Nanoparticles	70±15	0.253	-23±3	40±7	35	15	Barite, orthorhombic	$3.9 \cdot 10^{15}$	25.3	
Sub-microparticles	420±196	0.181	-26±6	270±65	124	3	Barite, orthorhombic	$2.2 \cdot 10^{13}$	4.8	
Microparticles	1480±260	0.079	-35±6	1300±210	19	5	Barite, orthorhombic	$1.3 \cdot 10^{11}$	0.8	

5.4.4 Cellular uptake of fluorescent barium sulfate particles

Fluorescently-labeled barium sulfate nano-, sub-micro- and microparticles were incubated with NR8383 macrophages. The NR8383 cell line provides a homogeneous source of highly responsive alveolar macrophages which can be used *in vitro* to study macrophage related activities. The presence of the particles was measured by confocal laser scanning microscopy. The cells were exposed to 50 µg mL^{-1} $BaSO_4$ particles for 24 h under cell culture conditions. After this incubation, the cells were labeled with specific cell organelle fluorescent probes. As a marker for late endosomes and lysosomes, the cells were incubated with 50 nM Lyso Tracker Red DND 99 in pure RPMI 1640 for 30 min at 37 °C. For labelling of the cell nucleus, the cells were incubated with 162 µM Hoechst33342 in pure RPMI 1640 for 5 min at 37 °C. After three rinses in RPMI 1640, the cells were mounted on glass chamber slides. Images were taken using a 40x oil immersion objective in a laser scanning microscope.

Figure 63 shows the cellular uptake of labeled barium sulfate nano-, sub-micro- and microparticles by NR8383 alveolar macrophages. The cell nucleus was shown in blue, late endosomes and lysosomes in red and particles in green. The upper images are combinations of bright field microscopy and fluorescence microscopy of the cell nucleus. The imaging area was selected to be representative for adherent cell population. As control, cells incubated in particle-free medium were used. Due to the fluorescence staining of cell organelles the presence of barium sulfate nano-, sub-micro-, and microparticles in lysosomes and late endosomes was confirmed.

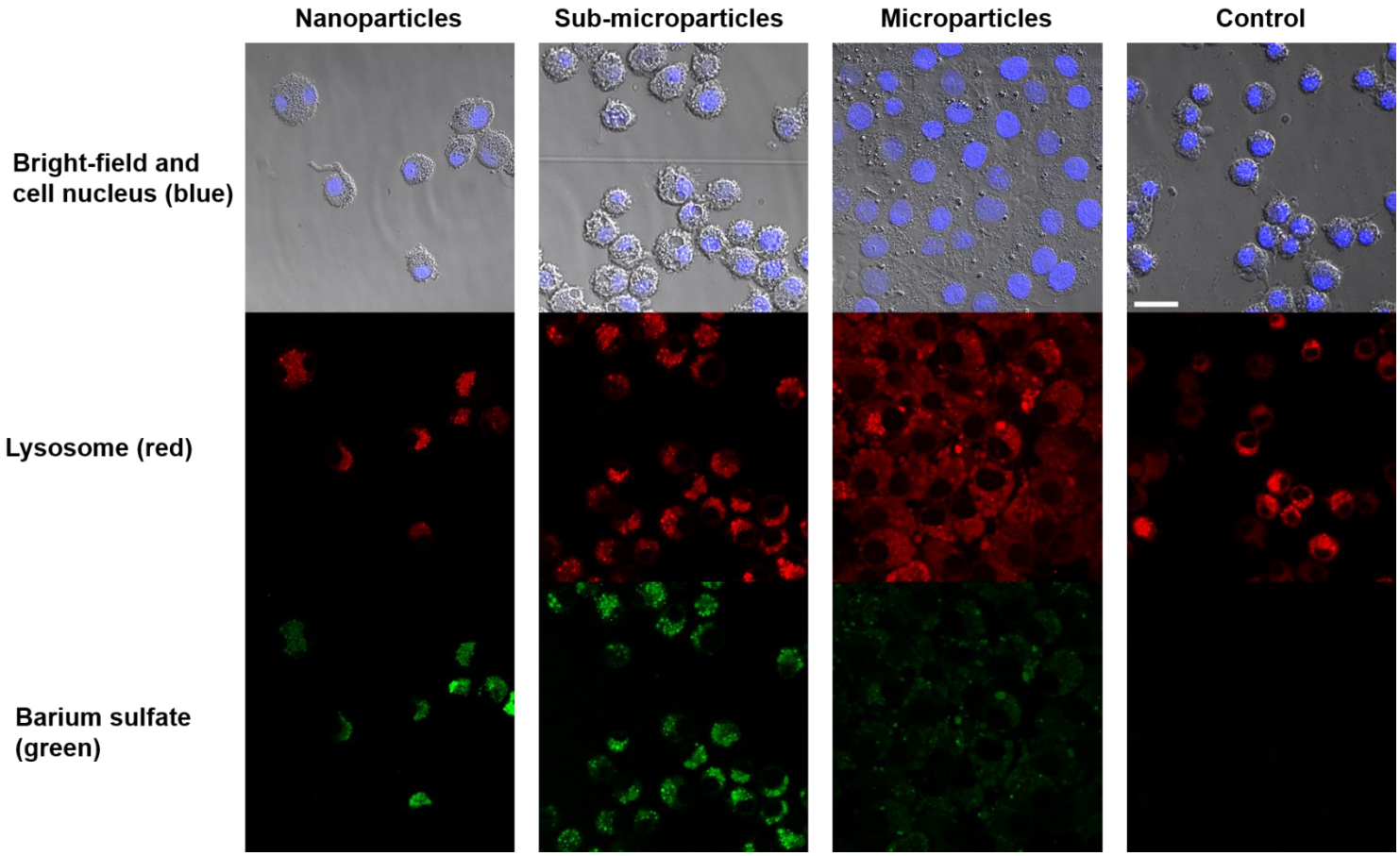

Figure 63: Cellular uptake of fluorescently-labeled barium sulfate particles by NR8383 macrophages. The scale bar is 20 µm.

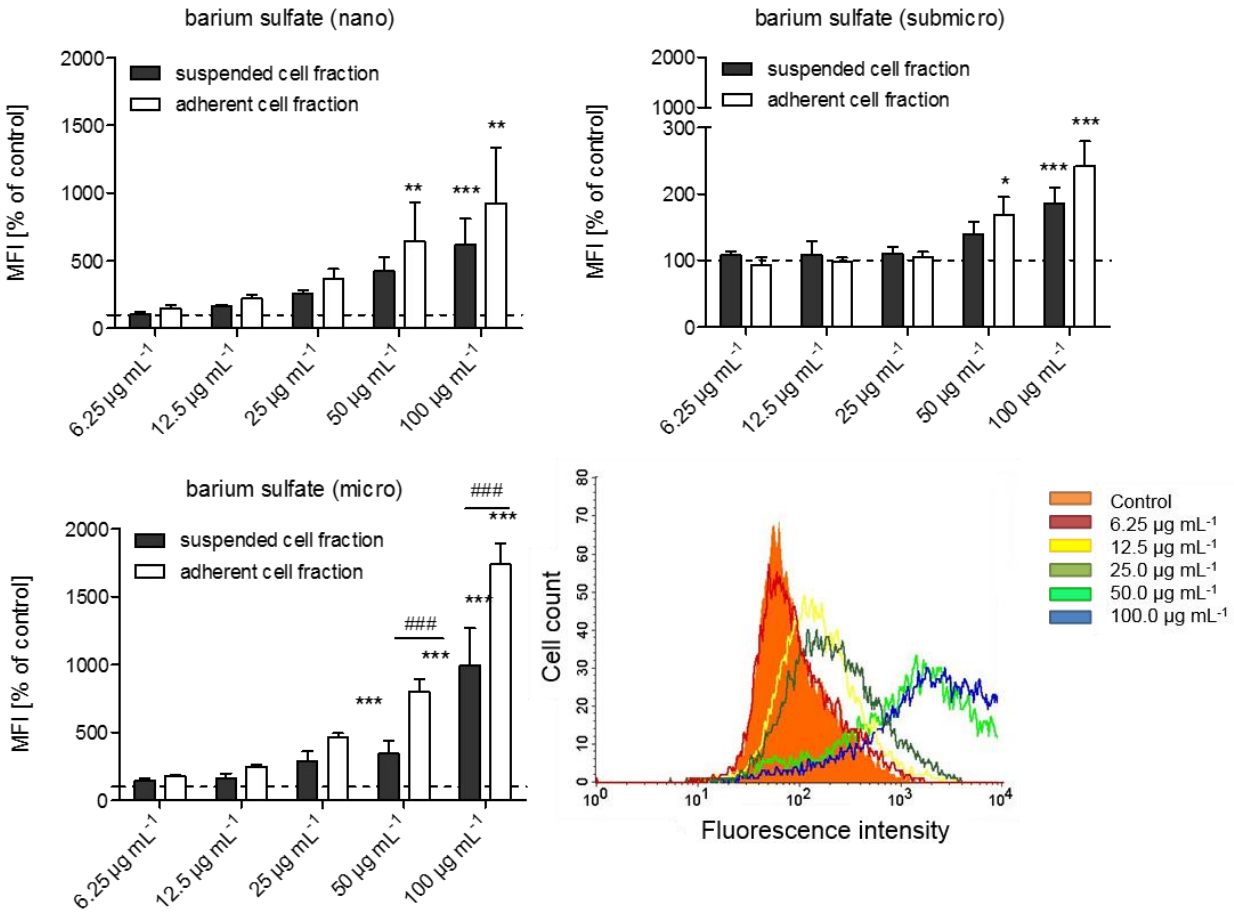

Figure 64: Cellular uptake of fluorescently-labeled barium sulfate particles by NR8383 macrophages as analyzed by flow cytometry. Quantitative data are expressed as the mean±SD (*N* = 3 independent experiments), given as the percent of the control (cells cultured without particles). The asterisk (*) indicates significant differences compared to the control (*p<0.05). A typical measurement run of flow cytometry is shown for barium sulfate microparticles in the lower right corner.

Figure 64 shows the quantitative interpretation of cellular uptake of labeled barium sulfate nano-, sub-micro- and microparticles by NR8383 alveolar macrophages, as measured by flow cytometry. Flow cytometry is normally used in biotechnology for cell counting and sorting.[60, 68, 74, 197, 198] As shown in a typical run, the increase of

fluorescently-labeled particles in the cell resulted in a higher fluorescence signal (right shift). NR8383 macrophages are mixed culture.[199-202] Taking into account this fact, the suspended cell fractions as well as adherent cell fractions were analyzed. Figure 64 shows the results plotted as fluorescent intensity with concentration of added labeled barium sulfate particles. The data suggest that an increase of the mean fluorescence intensity is concentration-dependent. A significant difference occurred in the case of barium sulfate microparticles for suspended and adherent cell fractions. It can be explained by the sedimentation of particles over time. This was confirmed by stability studies of dispersed particles in biological medium by dynamic light scattering.[203] However, an accurate quantitative study of particle uptake should involve a cytometer calibration. Flow cytometer sensitivity is often expressed in the form of molecules of equivalent soluble fluorochrome (MESF).[204] Moreover, the fluorophore content of the nano-, sub-micro-, and microparticles should be measured in order to get quantitative information about, how many particles were taken up by an individual cell.

5.4.5 Inflammatory potential of fluorescently-labeled barium sulfate nano-, sub-micro-, and microparticles

Particle inhalation can cause severe inflammatory lung diseases such as chronic obstructive pulmonary disease (COPD) as well as lung fibrosis and even tumors. These diseases are believed to be a consequence of chronic lung inflammation which can occur at high continuous particle exposure.[205-213] Particle-induced inflammation of the lung is initiated by the recruitment of macrophages and neutrophilic granulocytes.[168]

Accumulation of neutrophils in the lung is a hallmark of inflammatory reactions towards a broad spectrum of particles occurring at different workplaces and in the environment.[210, 214-217] *Westphal et al.* described a model which displays the attraction of neutrophils in response to particle challenge using permanent cell lines.

An inflammatory potential of nano-, sub-micro-, and microparticles was evaluated by particle-induced cell migration assay (PICMA).[168] NR8383 rat alveolar macrophages

were challenged with up to 200 µg mL^{-1} $BaSO_4$ in the form of nano-, sub-micro- and microparticles. The cell supernatants were used to induce cell migration of trans-retinal differentiated human leukemia cells (dHL-60 cells). Figure 65 shows the migration of dHL- 60 cells in response to culture supernatants which were yielded after a challenge of NR8383 macrophages with nano-, sub-micro- and microparticles.

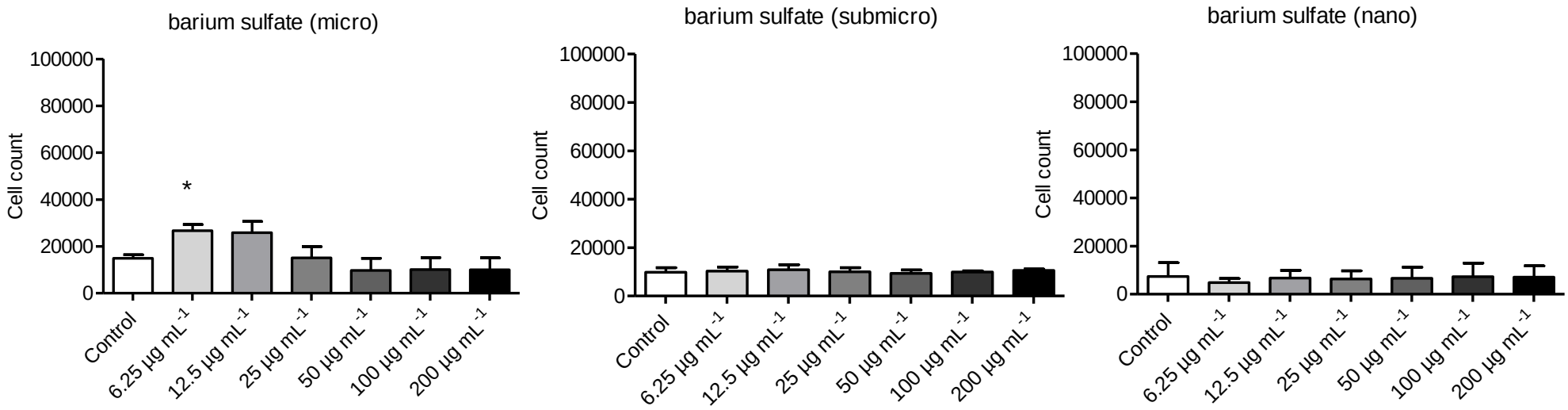

Figure 65: Migration of dHL-60 cells in response culture supernatants which were obtained following the challenge of NR8383 alveolar macrophages with nano-, sub-micro-, and microparticles. No chemotactic effect wasobserved dHL-60 cells. The released chemokines concentration did not trigger the migration of neutrophils.

The data reported in Figure 65 showed no chemotactic effect on dHL-60 cells. This means that chemokines were either not released at all or that they were released at a concentration which was not sufficient to trigger the migration of neutrophils. In this case, a migration of neutrophils should give a measurement of the inflammatory potential of the tested materials, since the accumulation of neutrophils was a hallmark of lung inflammation. No dose-dependency of particle-induced chemotaxis of dHL-60 cells in response to cell supernatants of particle challenged NR8383 macrophages could be shown. $BaSO_4$ was repeatedly shown to be not or only very weakly inflammatory *in vivo*.[218, 219] In agreement with these data weak - if any - cell migration was observed following a challenge with $BaSO_4$ nano-, sub-micro-, and microparticles. Moreover, no size effect of barium sulfate was observed.

The results of the present study demonstrated that barium sulfate nano-, sub-micro- and microparticles were fabricated and characterized extensively. Neither dose nor size dependency were shown for the particle-induced chemotaxis. These facts allow to use barium sulfate as a model compound for inert nanoparticle to identify factors which contribute to particle-induced inflammation.

.

6 Summary

This work comprises the synthesis procedures of toxicologically relevant particles, and their behavior in complex biological media in terms of stability and dissolution, with specific biological responses to the synthesized materials. Two toxicologically relevant particulate systems were studied. As a model of a biologically active material, silver compounds, especially silver nanoparticles, were investigated. In contrast, barium sulfate was examined as a bioinert system.

The formation of silver nanoparticles during the reduction with glucose in the presence of poly(vinylpyrrolidone) as a capping agent was followed for more than 3000 min. It was shown that spherical silver nanoparticles were formed first, but in later stages, an increasing fraction of nano-triangles and also a few nanorods developed. By electron microscopy, the growth of spherical and trigonal nanoparticles with time was described. From X-ray powder diffractometry, it was concluded that the domain size in the spherical nanoparticles increased proportionally to the particle diameter and was always about ¼ of the diameter, indicating that twinned seeds were formed very early in the process and then simply grew by extending their size. The lattice constant of the nanoparticles was systematically increased in comparison to microcrystalline silver, but did not change as a function of particle diameter.

The behavior of silver ions was investigated in biologically relevant concentrations in different media, from physiological salt solution over phosphate-buffered saline solution to protein-containing cell culture media. The results showed that silver ions that were initially present were bound as silver chloride due to the presence of chloride. Only in the absence of chloride, glucose was able to reduce Ag^{+} to Ag^{0}. The precipitation of silver phosphate was never observed in any case. It was concluded that the predominant silver species in biological media is dispersed nanoscopic silver chloride, surrounded by a protein corona which prevents the growth of crystals and leads to colloidal stabilization. Using bacteria (*S. aureus*) and cell culture experiments (human mesenchymal stem cells; T-cells; monocytes), it was possible to show that a

toxic effect occurred at the same silver concentration of ionic silver and synthetically prepared silver chloride nanoparticles. Furthermore, the dissolution of silver nanoparticles and the solubility products of silver chloride and silver nitrate were quantified in protein-containing cell culture media.

Barium sulfate micro-, sub-micro-, and nanoparticles were synthesized for evaluation of inflammatory potential. The synthesis of fluorescent labeled $BaSO_4$ particles with a narrow size distribution was achieved. The resultant powders were uniform in form, chemical composition and surface modification by the fluorescent dye. All of the particles were colloidally dispersed in cell culture medium with serum. From the cellular uptake studies on rat alveolar macrophages, it was concluded that a significant difference occurred in the case of barium sulfate microparticles for suspended and adherent cell fractions. This was explained by the sedimentation of synthesized particles over time, and confirmed by stability studies of dispersed particles in biological medium by dynamic light scattering. However, in a particle-induced cell migration assay for evaluation of the inflammation potential of the system, no dose- and size-dependency was found.

7 Literature

1. H. M. C. de Azeredo, *Int. Food Res. J.*, 2009, **42**, 1240-1253.
2. T. V. Duncan, *J. Colloid Interf. Sci.*, 2011, **363**, 1-24.
3. N. R. Panyala, E. M. Pena-Mendez and J. Havel, *J. Appl. Biomed.*, 2008, **6**, 117-129.
4. C. Silvestre, D. Duraccio and S. Cimmino, *Prog. Colloid Polym. Sci.*, 2011, **36**, 1766-1782.
5. Q. Li, S. Mahendra, D. Y. Lyon, L. Brunet, M. V. Liga, D. Li and P. J. J. Alvarez, *Water Res.*, 2008, **42**, 4591-4602.
6. B. Nowack, H. F. Krug and M. Height, *Environ. Sci. Technol.*, 2011, **45**, 1177-1183.
7. B. Nowack, J. F. Ranville, S. Diamond, J. A. Gallego-Urrea, C. Metcalfe, J. Rose, N. Horne, A. A. Koelmans and S. J. Klaine, *Environ. Toxicol. Chem.*, 2012, **31**, 50-59.
8. H. Cember, T. F. Hatch, J. A. Watson and T. Grucci, *AMA Arch. Ind. Health*, 1955, **12**, 628-634.
9. A. T. Doig, *Thorax*, 1976, **31**, 30-39.
10. T. Dosios and A. G. Karydas, *Ann. Thorac. Surg.*, 2003, **76**, 297.
11. S. Chernousova and M. Epple, *Angew. Chem. Int. Ed.*, 2013, **52**, 1636-1653.
12. R. Foldbjerg, P. Olesen, M. Hougaard, D. A. Dang, H. J. Hoffmann and H. Autrup, *Toxicol. Lett.*, 2009, **190**, 156-162.
13. J. S. Kim, E. Kuk, K. N. Yu, J.-H. Kim, S. J. Park, H. J. Lee, S. H. Kim, Y. K. Park, Y. H. Park and C.-Y. Hwang, *Nanomed. Nanotech. Biol. Med.*, 2007, **3**, 95-101.
14. M. Rai, A. Yadav and A. Gade, *Biotechnol. Adv.*, 2009, **27**, 76-83.
15. P. K. Jain, X. Huang, I. H. El-Sayed and M. A. El-Sayed, *Acc. Chem. Res.*, 2008, **41**, 1578-1586.
16. X. Chen and H. J. Schluesener, *Toxicol. Lett.*, 2008, **176**, 1-12.
17. D. A. LaVan, T. McGuire and R. Langer, *Nature Biotechnol.*, 2003, **21**, 1184-1191.
18. M. Ahamed, M. S. Al Salhi and M. K. J. Siddiqui, *Clin. Chim. Acta*, 2010, **411**, 1841-1848.
19. J. Jain, S. Arora, J. M. Rajwade, P. Omray, S. Khandelwal and K. M. Paknikar, *Molec. Pharm.*, 2009, **6**, 1388-1401.

20. R. Kaegi, A. Voegelin, C. Ort, B. Sinnet, B. Thalmann, J. Krismer, H. Hagendorfer, M. Elumelu and E. Mueller, *Water Res.*, 2013, **47**, 3866-3877.

21. A. A. Keller, S. McFerran, A. Lazareva and S. Suh, *J. Nanopart. Res.*, 2013, **15**.

22. R. Singh and H. S. Nalwa, *J. Biomed. Nanotechnol.*, 2011, **7**, 489-503.

23. R. Kresse, U. Baudis, P. Jäger, H. H. Riechers, H. Wagner, J. Winkler and H. U. Wolf, in *Ullmann's Encyclopedia of Industrial Chemistry*, Wiley, 2000.

24. F. Grum and G. W. Luckey, *Appl. Opt.*, 1968, **7**, 2289-2294.

25. D. J. Ott and D. W. Gelfand, *JAMA-J. Am. Med. Assoc.*, 1983, **249**, 2380-2384.

26. O. Choi and Z. Q. Hu, *Environ. Sci. Technol.*, 2008, **42**, 4583-4588.

27. R. Landsiedel, L. Ma-Hock, A. Kroll, D. Hahn, J. Schnekenburger, K. Wiench and W. Wohlleben, *Adv. Mater.*, 2010, **22**, 2601-2627.

28. G. Oberdoerster, J. Ferin and B. E. Lehnert, *Environ. Health Perspect.*, 1994, **102**, 173-179.

29. H. Johnston, G. Pojana, S. Zuin, N. R. Jacobsen, P. Moller, S. Loft, M. Semmler-Behnke, C. McGuiness, D. Balharry, A. Marcomini, H. Wallin, W. Kreyling, K. Donaldson, L. Tran and V. Stone, *Crit. Rev. Toxicol.*, 2013, **43**, 1-20.

30. O. Choi, K. K. Deng, N. J. Kim, L. Ross, R. Y. Surampalli and Z. Q. Hu, *Water Res.*, 2008, **42**, 3066-3074.

31. C. Greulich, D. Braun, A. Peetsch, J. Diendorf, B. Siebers, M. Epple and M. Koller, *RSC Adv.*, 2012, **2**, 6981-6987.

32. F. Herzog, M. J. D. Clift, F. Piccapietra, R. Behra, O. Schmid, A. Petri-Fink and B. Rothen-Rutishauser, *Part. Fibre Toxicol.*, 2013, **10**.

33. C. M. Ho, C. K. Wong, S. K. W. Yau, C. N. Lok and C. M. Che, *Chem. Asian J.*, 2011, **6**, 2506-2511.

34. T. Cosgrove, *Colloid Science: Principles, Methods and Applications*, John Willey and Sons Ltd, 2010.

35. I. N. Levine, *Physical Chemistry*, McGraw-Hill., Boston, 2001.

36. J. Sarquis, *J. Chem. Educ.*, 1980, **57**, 602-605.

37. J. N. Anker, W. P. Hall, O. Lyandres, N. C. Shah, J. Z. Zhao and R. P. Van Duyne, *Nat. Mater.*, 2008, **7**, 442-453.

38. A. N. Shipway, E. Katz and I. Willner, *Chem. Phys. Chem.*, 2000, **1**, 18-52.

39. R. M. Crooks, M. Q. Zhao, L. Sun, V. Chechik and L. K. Yeung, *Acc. Chem. Res.*, 2001, **34**, 181-190.

40. D. V. Talapin, J.-S. Lee, M. V. Kovalenko and E. V. Shevchenko, *Chem. Rev.*, 2010, **110**, 389-458.

41. Q. Wu, G. Zhao, C. Feng, C. Wang and Z. Wang, *J. Chromatogr. A*, 2011, **1218**, 7936-7942.

42. A. T. Bell, *Science*, 2003, **299**, 1688-1691.

43. R. Narayanan and M. A. El-Sayed, *J. Phys. Chem. B*, 2005, **109**, 12663-12676.

44. H. D. Dörfler, *Grenzflächen und kolloid-disperse Systeme*, Springer, Berlin, 2002.

45. G. Fritz, V. Schaedler, N. Willenbacher and N. J. Wagner, *Langmuir*, 2002, **18**, 6381-6390.

46. R. Zhang, G. Wang, S. Guo, M. L. Zamora, Q. Ying, Y. Lin, W. Wang, M. Hu and Y. Wang, *Chem. Rev.*, 2015, **115**, 3803-3855.

47. S. Bakshi, Z. L. He and W. G. Harris, *Critic. Rev. Envir. Sci. Technol.*, 2014, **45**, 861-904.

48. A. K. Madl, T. Kadir and K. E. Pinkerton, in *Reference Module in Biomedical Sciences*, Elsevier, 2015.

49. A. Kulkarni, G. S. Kumar, J. Kaur and K. Tikoo, *Inhal. Toxicol.*, 2014, **26**, 772-788.

50. C. A. Pope, D. W. Dockery and J. Schwartz, *Inhal. Toxicol.*, 1995, **7**, 1-18.

51. T. Kuwayama, C. R. Ruehl and M. J. Kleeman, *Environ. Sci. Technol.*, 2013, **47**, 13957-13966.

52. J. Ferin, G. Oberdoerster and D. P. Penney, *Am. J. Respir. Cell Mol. Biol.*, 1992, **6**, 535–542.

53. M. H. Tan, C. A. Commens and L. Burnett, *Australas. J. Dermatol.*, 1996, **37**.

54. S. R. Pinnell, D. Fairhurst, R. Gillies, M. A. Mitchnick and N. Kollias, *Derm. Surg.*, 2000, **26**, 309-313.

55. P. Jani, G. W. Halbert, J. Langridge and A. T. Florence, *J. Pharm. Pharmacol.*, 1990, **42**, 821-826.

56. A. M. Hillery, P. U. Jani and A. T. Florence, *J. Drug Target.*, 1994, **2**, 151-156.

57. C. R. Arciola, D. Campoccia, P. Speziale, L. Montanaro and J. W. Costerton, *Biomaterials*, 2012, **33**, 5967-5982.

58. W. Zimmerli and C. Moser, *Pathogenesis and treatment concepts of orthopaedic biofilm infections*, 2012.

59. J. W. Alexander, *Surg. Infect.*, 2009, **10**, 289-292.

60. K. Loza, J. Diendorf, C. Greulich, L. Ruiz-Gonzales, J. M. Gonzalez-Calbet, M. Vallet-Regi, M. Koeller and M. Epple, *J. Mater. Chem. B*, 2014, **2**, 1634-1643.

61. Z. M. Xiu, Q. B. Zhang, H. L. Puppala, V. L. Colvin and P. J. J. Alvarez, *Nano Lett.*, 2012, **12**, 4271-4275.

62. H. Cember, T. F. Hatch, J. A. Watson, T. Grucci and P. Bell, *AMA Arch. Ind. Health*, 1956, **13**, 170-176.

63. N. Konduru, J. Keller, L. Ma-Hock, S. Groeters, R. Landsiedel, T. C. Donaghey, J. D. Brain, W. Wohlleben and R. M. Molina, *Part. Fibre. Toxicol.*, 2014, **11**.

64. J. Goldstein, *Scanning Electron Microscopy and X-Ray Microanalysis*, Springer, 2003.

65. A. W. Coats and J. P. Redfern, *Analyst*, 1963, **88**, 906-924.

66. H. Wang, X. Qiao, J. Chen and S. Ding, *Coll. Surf. A Physicochem. Eng. Aspects*, 2005, **256**, 111-115.

67. C. An, S. Peng and Y. Sun, *Adv. Mater.*, 2010, **22**, 2570-2574.

68. C. Greulich, J. Diendorf, T. Simon, G. Eggeler, M. Epple and M. Köller, *Acta Biomater.*, 2011, **7**, 347-354.

69. S. Kittler, C. Greulich, J. Diendorf, M. Köller and M. Epple, *Chem. Mater.*, 2010, **22**, 4548-4554.

70. S. Kittler, C. Greulich, M. Köller and M. Epple, *Mat.-wiss. u. Werkstofftech.*, 2009, **40**, 258-264.

71. D. English and B. R. Andersen, *J. Immunol. Meth.*, 1974, **5**, 249-252.

72. S. Ahlberg, A. Antonopulos, J. Diendorf, R. Dringen, M. Epple, R. Floeck, W. Goedecke, C. Graf, N. Haberl, J. Helmlinger, F. Herzog, F. Heuer, S. Hirn, C. Johannes, S. Kittler, M. Koeller, K. Korn, W. G. Kreyling, F. Krombach, J. Lademann, K. Loza, E. M. Luther, M. Malissek, M. C. Meinke, D. Nordmeyer, A. Pailliart, J. Raabe, F. Rancan, B. Rothen-Rutishauser, E. Ruehl, C. Schleh, A. Seibel, C. Sengstock, L. Treuel, A. Vogt, K. Weber and R. Zellner, *Beilstein J. Nanotechnol.*, 2014, **5**, 1944-1965.

73. S. Banerjee, K. Loza, W. Meyer-Zaika, O. Prymak and M. Epple, *Chem. Mater.*, 2014, **26**, 951-957.

74. C. Greulich, J. Diendorf, J. Geßmann, T. Simon, T. Habijan, G. Eggeler, T. A. Schildhauer, M. Epple and M. Köller, *Acta Biomater.*, 2011, **7**, 3505-3514.

75. S. Hirn, N. Haberl, K. Loza, M. Epple, C. Schleh, W. G. Kreyling, B. Rothen-Rutishauser, M. Rehberg and F. Krombach, *Beilstein J. Nanotechnol.*, 2014, **5**, 2440-2449.

76. S. K. Arumugam, T. P. Sastry, B. Sreedhar and A. B. Mandal, *J. Biomed. Mater. Res. A*, 2007, **80**, 391-398.

77. Y. A. Krutyakov, A. A. Kudrinskiy, A. Y. Olenin and G. V. Lisichkin, *Uspekhi Khimii*, 2008, **77**, 242-269.

78. S. Wojtysiak and A. Kudelski, *Colloids Surf. A Physicochem. Eng. Asp.*, 2012, **410**, 45-51.

79. Q. Zhang, Y. Hu, S. Guo, J. Goebl and Y. Yin, *Nano Lett.*, 2010, **10**, 5037-5042.

80. H. P. Klug and L. E. Alexander, *X-ray diffraction procedures for polycrystalline and amorphous materials*, Wiley-Interscience, New York, 1974.

81. H. E. Swanson and Fuyat, *Nat. Bureau Standards (U.S.), Circular*, 1954, **539**, 3.

82. I. K. Suh, H. Ohta and Y. Waseda, *J. Mater. Sci.*, 1988, **23**, 757-760.

83. M. Fukuhara, *Phys. Lett. A*, 2003, **313**, 427-430.

84. Y. Xia, X. Xia, Y. Wang and S. Xie, *MRS Bull.*, 2013, **38**, 335-344.

85. B. Wiley, Y. Sun, B. Mayers and Y. Xia, *Chem. Eur. J.*, 2005, **11**, 454-463.

86. B. Wiley, Y. Sun and Y. Xia, *Acc. Chem. Res.*, 2007, **40**, 1067-1076.

87. X. Xia, J. Zeng, L. K. Oetjen, W. Li and Y. Xia, *J. Am. Chem. Soc.*, 2012, **134**, 1793-1801.

88. Y. N. Xia, Y. Xiong, B. Lim and S. E. Skrabalak, *Angew. Chem. Int. Ed.*, 2009, **48**, 60-103.

89. Y. G. Sun and Y. N. Xia, *Science*, 2002, **298**, 2176-2179.

90. J. E. Millstone, S. J. Hurst, G. S. Metraux, J. I. Cutler and C. A. Mirkin, *Small*, 2009, **5**, 646-664.

91. S. Galdiero, A. Falanga, M. Vitiello, M. Cantisani, V. Marra and M. Galdiero, *Molecules*, 2011, **16**, 8894-8918.

92. M. Beattie and J. Taylor, *J. Clin. Nurs.*, 2011, **20**, 2098-2108.

93. B. Simoncic and B. Tomsic, *Text. Res. J.*, 2010, **80**, 1721-1737.

94. K. Chaloupka, Y. Malam and A. M. Seifalian, *Trends Biotechnol.*, 2010, **28**, 580-588.

95. K. Vasilev, J. Cook and H. J. Griesser, *Expert Rev. Med. Devices*, 2009, **6**, 553-567.

96. C. Dowsett, *Nurs. Stand.* , 2004, **19**, 56-60.

97. H. J. Klasen, *Burns*, 2000, **26**, 131-138.

98. S. F. Hansen and A. Baun, *Nat. Nanotechnol.*, 2012, **7**, 409-411.

99. F. Gottschalk and B. Nowack, *J. Environ. Monit.*, 2011, **13**, 1145-1155.

100. M. E. Quadros and L. C. Marr, *J. Air Waste Manage.*, 2010, **60**, 770-781.

101. C. Marambio-Jones and E. M. V. Hoek, *J. Nanopart. Res.*, 2010, **12**, 1531-1551.

102. S. W. P. Wijnhoven, W. J. G. M. Peijnenburg, C. A. Herberts, W. I. Hagens, A. G. Oomen, E. H. W. Heugens, B. Roszek, J. Bisschops, I. Gosens, D. van De Meent, S. Dekkers, W. H. De Jong, M. van Zijverden, A. J. A. M. Sips and R. E. Geertsma, *Nanotoxicology*, 2009, **3**, 109-138.

103. H. T. Ratte, *Environ. Toxicol. Chem.*, 1999, **18**, 89-108.

104. J. R. Reinfelder and S. I. Chang, *Env. Sci. Toxicol.*, 1999, **33**, 1860-1863.

105. J. K. Schluesener and H. J. Schluesener, *Arch. Toxicol.*, 2013, **87**, 569-576.

106. G. A. Sotiriou and S. E. Pratsinis, *Environ. Sci. Technol.*, 2010, **44**, 5649-5654.

107. H. Zhang, J. A. Smith and V. Oyanedel-Craver, *Water Res.*, 2012, **46**, 691-699.

108. S. K. Zhang, C. Du, Z. Z. Wang, X. G. Han, K. Zhang and L. H. Liu, *Toxicol. Vitro*, 2013, **27**, 739-744.

109. J. M. Zook, S. E. Long, D. Cleveland, C. L. A. Geronimo and R. I. MacCuspie, *Anal. Bioanal. Chem.*, 2011, **401**, 1993-2002.

110. S. Ahlberg, M. C. Meinke, L. Werner, M. Epple, J. Diendorf, U. Blume-Peytavi, J. Lademann, A. Vogt and F. Rancan, *Eur. J. Pharm. Biopharm.*, 2014, **88**, 651-657.

111. E. M. Luther, Y. Koehler, J. Diendorf, M. Epple and R. Dringen, *Nanotechnology*, 2011, **22**, 375101.

112. A. Vogt, F. Rancan, S. Ahlberg, B. Nazemi, C. S. Choe, M. E. Darvin, U. Blume-Peytavi, K. Loza, J. Diendorf, M. Epple, C. Graf, E. Rühl, M. C. Meinke and J. Lademann, *Beilstein J. Nanotechnol.*, 2014, **5**, 2363-2373.

113. J. Y. Liu, Z. Y. Wang, F. D. Liu, A. B. Kane and R. H. Hurt, *ACS Nano*, 2012, **6**, 9887-9899.

114. S. Tenzer, D. Docter, J. Kuharev, A. Musyanovych, V. Fetz, R. Hecht, F. Schlenk, D. Fischer, K. Kiouptsi, C. Reinhardt, K. Landfester, H. Schild, M. Maskos, S. K. Knauer and R. H. Stauber, *Nat. Nanotechnol.*, 2013, **8**, 772-781.

115. J. S. Gebauer, M. Malissek, S. Simon, S. K. Knauer, M. Maskos, R. H. Stauber, W. Peukert and L. Treuel, *Langmuir*, 2012, **28**, 9673-9679.

116. S. Grass, J. Diendorf, J. S. Gebauer, M. Epple and L. Treuel, *J. Nanosci. Nanotechnol.*, 2015, **15**, 1591-1596.

117. S. Kittler, C. Greulich, J. S. Gebauer, J. Diendorf, L. Treuel, L. Ruiz, J. M. Gonzalez-Calbet, M. Vallet-Regi, R. Zellner, M. Köller and M. Epple, *J. Mater. Chem.*, 2010, **20**, 512-518.

118. V. Mirshafiee, M. Mahmoudi, K. Lou, J. Cheng and M. L. Kraft, *Chem. Comm.*, 2013, **49**, 2557-2559.

119. C. Röcker, M. Pötzl, F. Zhang, W. J. Parak and G. U. Nienhaus, *Nat. Nanotechnol.*, 2009, **4**, 577-580.

120. L. Shang, Y. Wang, J. Jiang and S. Dong, *Langmuir*, 2007, **23**, 2714-2721.

121. L. Treuel, S. Brandholt, P. Maffre, S. Wiegele, L. Shang and G. U. Nienhaus, *ACS Nano*, 2014, **28**, 503-513.

122. L. Treuel and G. U. Nienhaus, *Biophys. Rev.*, 2012, **4**, 137-147.

123. I. Lynch and K. A. Dawson, *Nano Today*, 2008, **3**, 40-47.

124. M. P. Monopoli, C. Åberg, A. Salvati and K. A. Dawson, *Nature Nanotechnol.*, 2012, **7**, 779-786.

125. M. P. Monopoli, D. Walczyk, A. Campbell, G. Elia, I. Lynch, F. B. Bombelli and K. A. Dawson, *J. Am. Chem. Soc.*, 2011, **133**, 2525-2534.

126. B. L. Nielsen and L. R. Brown, *Anal. Biochem.*, 1984, **141**, 311-315.

127. H. C. Li, K. W. Michael Siu, R. Guevremont and J. C. Yves Le Blanc, *J Am Soc Mass Spectrom*, 1997, **8**, 781-792.

128. A. Hreniak, J. Rybka, A. Gamian, K. Hermanowicz, J. Hanuza and K. Maruszewski, *J. Lumin.*, 2007, **122**, 987-989.

129. E. Caballero-Díaz, C. Pfeiffer, L. Kastl, P. Rivera-Gil, B. Simonet, M. Valcárcel, J. Jiménez-Lamana, F. Laborda and W. J. Parak, *Part. Part. Syst. Char.*, 2013, **30**, 1079-1085.

130. I. Canton and G. Battaglia, *Chem. Soc. Rev.*, 2012, **41**, 2718-2739.

131. T. G. Iversen, T. Skotland and K. Sandvig, *Nano Today*, 2011, **6**, 176-185.

132. G. Sahay, D. Y. Alakhova and A. V. Kabanov, *J. Control. Release*, 2010, **145**, 182-195.

133. J. R. Morones, J. L. Elechiguerra, A. Camacho, K. Holt, J. B. Kouri, J. T. Ramirez and M. J. Yacaman, *Nanotechnology*, 2005, **16**, 2346-2353.

134. J. Ji, N. Rosenzweig, C. Griffin and Z. Rosenzweig, *Anal. Chem.*, 2000, **72**, 3497-3503.

135. C. M. Wood, M. Grosell, C. Hogstrand and H. Hansen, *Aquat. Toxicol.*, 2002, **56**, 197-213.

136. M. Grosell, C. Hogstrand, C. M. Wood and H. J. M. Hansen, *Aquat. Toxicol.*, 2000, **48**, 327-342.

137. Y. Teow, P. V. Asharani, M. P. Hande and S. Valiyaveettil, *Chem. Comm.*, 2011, **47**, 7025-7038.

138. G. A. Sotiriou and S. E. Pratsinis, *Curr. Opinion Chem. Eng.*, 2011, **1**, 3-10.

139. J. Liu, D. A. Sonshine, S. Shervani and R. H. Hurt, *ACS Nano*, 2010, **4**, 6903-6913.

140. L. Liu and R. H. Hurt, *Environ. Sci. Technol.*, 2010, **44**, 2169-2175.

141. W. Liu, Y. A. Wu, C. Wang, H. C. Li, T. Wang, C. Y. Liao, L. Cui, Q. F. Zhou, B. Yan and G. B. Jiang, *Nanotoxicology*, 2010, **4**, 319-330.

142. X. Li, J. J. Lenhart and H. W. Walker, *Langmuir*, 2010, **26**, 16690-16698.

143. C. M. Ho, S. K. W. Yau, C. N. Lok, M. H. So and C. M. Che, *Chem. Asian J.*, 2010, **5**, 285-293.

144. C. Levard, B. C. Reinsch, F. M. Michel, C. Oumahi, G. V. Lowry and G. E. Brown, *Environ. Sci. Technol.*, 2011, **45**, 5260-5266.

145. Q. Zhang, N. Li, J. Goebl, Z. D. Lu and Y. D. Yin, *J. Am. Chem. Soc.*, 2011, **133**, 18931-18939.

146. W. Zhang, Y. Yao, N. Sullivan and Y. Chen, *Environ. Sci. Technol.*, 2011, **45**, 4422-4428.

147. Z. M. Xiu, J. Ma and P. J. J. Alvarez, *Environ. Sci. Technol.*, 2011, **45**, 9003-9008.

148. K. Loza, C. Sengstock, S. Chernousova, M. Köller and M. Epple, *RSC Adv.*, 2014, **4**, 35290-35297.

149. R. J. Lancashire, *Comprehensive Coordination Chemistry*, Pergamon Press 1987.

150. J. Heukeshoven and R. Dernick, *Electrophoresis*, 1985, **6**, 103.

151. A. J. Zelazowski, Z. Gasyna and M. J. Stillman, *J. Biol. Chem.*, 1989, **264**, 17091.

152. N. Farrell, *Transition Metal Complexes as Drugs and Chemotherapeutic Agent*, Kluwer Academic Publishers, 1989.

153. R. M. Slawson, H. Lee and J. T. Trevors, *Biol. Metals*, 1990, **3**, 151.

154. A. D. Russell and W. B. Hugo, *Prog. Med. Chem.*, 1994, **31**, 351.

155. R. C. Tilton and B. Rosenberg, *Appl. Environ. Microbiol.*, 1978, **35**, 1116.

156. S. J. Berners-Pdce, R. K. Johnson, A. J. Giovenella, L. F. Faucette, C. K. Mirabelli and P. J. Sadler, *J. Inorg. Biochem.*, 1988, **33**, 285.

157. R. Gillani, R. Ercan, A. Qiao and T. J. Webster, *Int. J. Nanomedicine*, 2010, **5**, 1-11.

158. A. H. Gomoll, W. Fitz, R. D. Scott, T. S. Thornhill and A. Bellare, *Acta Orthop.*, 2008, **79**, 421-427.

159. D. Mohn, M. Zehnder, T. Imfeld and W. J. Stark, *Int. Endod. J.*, 2010, **43**, 210-217.

160. R. Noreen, R. Pineau, C. C. Chien, C.-G. M., Y. Hwu, A. Marcelli, M. Moenner and C. Petibois, *Anal. Bioanal. Chem.*, 2011, **401**, 795-801.

161. J. R. Villalobos-Hernández and C. C. Müller-Goymann, *Eur. J. Pharm. Biopharm.*, 2005, **60**, 113-122.

162. G. E. Aninwene, D. Stout, Z. Yang and T. J. Webster, *Int. J. Nanomedicine* 2013, **8**, 1197-1205.

163. P. Levi-Valensi, M. Drif, A. Dat and G. Hadjadj, *J. Fr. Med. Chir. Thorac.*, 1966, **20**, 443-455.

164. R. T. Cullen, C. L. Tran, D. Buchanan, J. M. C. Davis, A. Searl, A. D. Jones and K. Donaldson, *Inhal. Toxicol.*, 2000, **12**, 1089-1111.

165. S. N. Cullen and A. S. McIntyre, *Eur. J. Gastroenterol. Hepatol.*, 2000, **12**, 1151-1162.

166. C. L. Tran, D. Buchanan, R. T. Cullen, A. Searl, A. D. Jones and K. Donaldson, *Inhal. Toxicol.*, 2000, **12**, 1113-1126.

167. P. Mohazzabi and A. W. Searcy, *J. Chem. Soc., Faraday Trans. 1*, 1976, **72**, 290-295.

168. G. A. Westphal, I. Schremmer, A. Rostek, K. Loza, N. Rosenkranz, T. Bruening, M. Epple and J. Buenger, *Toxicol. Vitro*, 2015, **29**, 997-1005.

169. G. Wu, H. Zhou and S. Zhu, *Mater. Lett.*, 2007, **61**, 168-170.

170. M. Sohrabi and S. F. Pirkashani, *Int. J. Chem. React. Eng.*, 2007, **5**.

171. G.-H. Wu, H.-Z. Zhou and S.-L. Zhu, *J. Inorg. Mater.*, 2006, **21**, 1079-1084.

172. Y. Liu, C. Cheng, Y. Liu, R. K. Prud'homme and R. O. Fox, *Chem. Eng. Sci.*, 2008, **63**, 2829-2842.

173. H. C. Schwarzer and W. Peukert, *AIChe J.*, 2004, **50**, 3234-3247.

174. C. Fang, F. Hua, Y. Cong, J. Fu and Y. Cheng, *J. Mater. Chem. B*, 2013, **1**, 4043-4047.

175. H. C. Schwarzer and W. Peukert, *Chem. Eng. Technol.*, 2002, **25**, 657-661.

176. H. Bala, W. Y. Fu, Y. P. Guo, J. Z. Zhao, Y. Q. Jiang, X. F. Ding, K. F. Yu, M. G. Li and Z. C. Wang, *Colloid Surface A*, 2006, **274**, 71-76.

177. C. Fang, R. Hou, K. Zhou, F. Hua, Y. Cong, J. Zhang, J. Fu and Y. Cheng, *J. Mater. Chem. B*, 2014, **2**, 1264-1274.

178. B. Judat and M. Kind, *J. Colloid Interf. Sci.*, 2004, **269**, 341-353.

179. M. Kucher, D. Babic and M. Kind, *Chem. Eng. Proces.*, 2006, **45**, 900-907.

180. D. E. Lee, H. Koo, I. C. Sun, J. H. Ryu, K. Kim and I. C. Kwon, *Chem. Soc. Rev.*, 2012, **41**, 2656-2672.

181. H. Lee, M. Veerapandian, B. T. Kim, K. Yun and S.-W. Seo, *J. Nanosci. Nanotechnol.*, 2012, **12**, 7752-7763.

182. B. M. Nagaraja, H. Abimanyu, K. D. Jung and K. S. Yoo, *J. Colloid Interf. Sci.*, 2007, **316**, 645-651.

183. B. Niemann and K. Sundmacher, *Chem. Eng. J.*, 2008, **143**, 314-325.

184. A. Petrova, W. Hintz and J. Tomas, *Chem. Eng. Technol.*, 2008, **31**, 604-608.

185. M. Pieper, S. Aman, W. Hintz and J. Tomas, *Chem. Eng. Technol.*, 2011, **34**, 1567-1574.

186. X. Yao, Y. Zhang, L. Du, J. Liu and J. Yao, *Renew. Sust. Energ Rev.*, 2015, **47**, 519-539.

187. H. Dabir, M. Davarpanah and A. Ahmadpour, *Appl. Phys. A Mater.*, 2015, **120**, 105-113.

188. M. Hosni, S. Farhat, M. Ben Amar, A. Kanaev, N. Jouini and I. Hinkov, *Aiche J.*, 2015, **61**, 1708-1721.

189. D. Konopacka-Lyskawa, B. Koscielska and J. Karczewski, *J. Cryst. Growth*, 2015, **418**, 25-31.

190. R. T. Kuegler, S. Doyle and M. Kind, *Chem. Eng. Sci.*, 2015, **133**, 140-147.

191. L. Hu, G. Wang, R. Cao, C. Yang and X. Chen, *Appl. Surf. Sci.*, 2014, **315**, 184-189.

192. E. Vafa, M. Shahrokhi and A. M. Dehkordi, *Ind. Eng. Chem. Res.*, 2014, **53**, 12705-12719.

193. M. Kowacz, M. Marchel, J. M. S. S. Esperanca and L. P. N. Rebelo, *Mater. Chem. Phys.*, 2015, **160**, 308-314.

194. S. Sivakumar, P. Soundhirarajan, A. Venkatesan and C. P. Khatiwada, *Spectrochim. Acta A Mol. Biomol. Spectrosc.*, 2015, **137**, 137-147.

195. Q. Wang, K. Qian, S. Liu, Y. Yang, B. Liang, C. Zheng, X. Yang, H. Xu and A. Q. Shen, *Biomacromolecules*, 2015, **16**, 1240-1246.

196. M. Wszelaka-Rylik, K. Piotrowska and P. Gierycz, *J. Therm. Anal. Calorim.*, 2015, **119**, 1323-1338.

197. G. Grynkiewicz, M. Poenie and R. Y. Tsien, *J. Appl. Biol. Chem.*, 1985, **260**, 3440-3450.

198. M. F. Pittenger, A. M. Mackay, S. C. Beck, R. K. Jaiswal, R. Douglas, J. D. Mosca, M. A. Moorman, D. W. Simonetti, S. Craig and D. R. Marshak, *Science*, 1999, **284**, 143-147.

199. M. Kitamura, *J. Immunol.*, 1997, **159**, 1404-1411.

200. M. Barua, Y. Liu and M. R. Quinn, *J. Immunol.*, 2001, **167**, 2275-2281.

201. Y. Ikezumi, L. A. Hurst, T. Masaki, R. C. Atkins and D. J. Nikolic-Paterson, *Kidn. Int.*, 2003, **63**, 83-95.

202. K. Pulskamp, S. Diabate and H. F. Krug, *Toxicol. Lett.*, 2007, **168**, 58-74.

203. R. C. Murdock, L. Braydich-Stolle, A. M. Schrand, J. J. Schlager and S. M. Hussain, *Toxicol. Sci.*, 2008, **101**, 239-253.

204. E. M. Goldys, *Fluorescence applications in biotechnology and life sciences*, Wiley-Blackwell, 2008.

205. J. Schwartz, D. W. Dockery and L. M. Neas, *J. Air Waste Manage.*, 1996, **46**, 927-939.

206. D. L. Costa and K. L. Dreher, *Environ. Health Persp.*, 1997, **105**, 1053-1060.

207. C. A. Pope, *Environ. Health Persp.*, 2000, **108**, 713-723.

208. R. W. Atkinson, H. R. Anderson, J. Sunyer, J. Ayres, M. Baccini, J. M. Vonk, A. Boumghar, F. Forastiere, B. Forsberg, G. Touloumi, J. Schwartz and K. Katsouyanni, *Am. J. Respir. Critic. Care Med.*, 2001, **164**, 1860-1866.

209. A. L. F. Braga, A. Zanobetti and J. Schwartz, *Environ. Health Perspect.*, 2002, **110**, 859-863.

210. J. C. Hogg, *Lancet*, 2004, **364**, 709-721.

211. C. A. Pope, R. T. Burnett, G. D. Thurston, M. J. Thun, E. E. Calle, D. Krewski and J. J. Godleski, *Circulation*, 2004, **109**, 71-77.

212. B. Brunekreef and B. Forsberg, *Eur. Respir. J.*, 2005, **26**, 309-318.

213. F. Dominici, R. D. Peng, M. L. Bell, L. Pham, A. McDermott, S. L. Zeger and J. M. Samet, *JAMA-J. Am. Med. Assoc.*, 2006, **295**, 1127-1134.

214. J. E. Krawisz, P. Sharon and W. F. Stenson, *Gastroenterology*, 1984, **87**, 1344-1350.

215. C. G. Larsen, A. O. Anderson, E. Appella, J. J. Oppenheim and K. Matsushima, *Science*, 1989, **243**, 1464-1466.

216. R. T. Dean, S. L. Fu, R. Stocker and M. J. Davies, *Biochem. J.*, 1997, **324**, 1-18.

217. C. Lamb and R. A. Dixon, *Annu. Rev. Plant Physiol. Plant Mol. Biol.*, 1997, **48**, 251-275.

218. C. L. Klein, K. Wiench, M. Wiemann, L. Ma-Hock, B. van Ravenzwaay and R. Landsiedel, *Arch. Toxicol.*, 2012, **86**, 1137-1151.

219. T. Trong Binh, N. Phuong Diem, S. H. Um, S. J. Son and J. Min, *J. Biomed. Nanotechnol.*, 2013, **9**, 286-290.

8 Appendix

8.1 List of abbreviations

AAS	Atomic absorption spectroscopy
CMC-F	Carboxymethylcellulose conjugated with 6-aminofluorescein
DLS	Dynamic light scattering
DLVO	Derjaguin, Landau, Verwey, Overbeek
DMEM	Dulbecco's modified Eagle's medium
DMEM + 10% FCS	Dulbecco's modified Eagle's medium supplemented with 10% fetal calf serum
EDTA	Ethylenediaminetetraacetate
EDX	Energy-dispersive X-ray spectroscopy
FACS	Fluorescence-activated cell sorting
FCS	Fetal calf serum
FWHM	Full width at half maximum
HeLa	Henrietta Lacks

hMSCs	Human mesenchymal stem cells
JCPDS	Joint Committee on Powder Diffraction Standards
LB	Lysogeny broth
MBC	Minimum bactericidal concentration
MIC	Minimum inhibitory concentration
NR8383	Rat alveolar macrophages
NTA	Nanoparticle tracking Analysis
PBMC	Peripheral blood mononuclear cells
PBS	Phosphate-buffered saline
PDI	Polydispersity index
PEI	Poly(ethyleneimine)
PVP	Poly(vinylpyrrolidone)
ROS	Reactive oxygen species
RPMI	Roswell Park Memorial Institute

S. aureus	*Staphylococcus aureus*
SEM	Scanning electron microscopy
TEM	Transmission electron microscopy
Uv/Vis	Ultraviolett / Visible
XRD	X-ray diffraction

8.2 Publications

B. Schütze, C. Mayer, K. Loza, M. Gocyla, M. Heggen, M. Epple, "The conjugation of thiol-terminated molecules to ultrasmall 2 nm-gold nanoparticles leads to remarkably complex ^{1}H-NMR spectra", Journal of Materials Chemistry B

M. Tolkachov, V. Sokolova, K. Loza, V. Korolovych, Yu. Prylutskyy, M. Epple, U. Ritter, P. Scharff, "*In vitro* toxic effect of nanocarbon particles on various cell types", Materialwissenschaft und Werkstofftechnik (submitted)

I. Schremmer, A. Brik, D.G. Weber, N. Rosenkranz, A. Rostek, K. Loza, T. Brüning, G. Johnen, M. Epple, J. Bünger, G.A. Westphal, "Chemotaxis, cytokine and chemokine release of NR8383 macrophages after exposure to amorphous silica, crystalline quartz, barium sulfate and titanium dioxide", Toxicology in Vitro (submitted)

C. Hadjicharalambous, O. Prymak, K. Loza, A. Buyakov, S. Kulkov, M. Chatzinikolaidou, "Effect of porosity of alumina and zirconia ceramics towards pre-osteoblast response", Frontiers in Bioengineering and Biotechnology 3 (2015) 175

A. Lübke, J. Enax, K. Loza, O. Prymak, P. Gaengler, H.-O. Fabritius, D. Raabe, M. Epple, "Dental lessons from past to present: ultrastructure and composition of teeth from plesiosaurs, dinosaurs, extinct and recent sharks", RSC Advances 5 (2015) 61612-61622

S. Ristig, O. Prymak, K. Loza, M. Gocyla, W. Meyer-Zaika, M. Heggen, D. Raabe, M. Epple, "Nanostructure of wet-chemically prepared, polymer-stabilized silver–gold nanoalloys (6 nm) over the entire composition range", Journal of Materials Chemistry B 3 (2015) 4654-4662

G.A. Westphal, I. Schremmer, A. Rostek, K. Loza, N. Rosenkranz, T. Brüning, M. Epple, J. Bünger, "Particle induced cell migration assay (PICMA): a new in vitro

assay for inflammatory particle effects based on permanent cell lines", Toxicology in vitro 29 (2015) 997-1005

A.A. Ivanova, R.A. Surmenev, M.A. Surmeneva, T. Mukhametkaliyev, K. Loza, O. Prymak, M. Epple, "Hybrid biocomposite with a tunable antibacterial activity and bioactivity based on rf magnetron sputter deposited coating and silver nanoparticles", Applied Surface Science 329 (2015) 212-218

S. Hirn, N. Haberl, K. Loza, M. Epple, W.G. Kreyling, B. Rothen-Rutishauser, M. Rehberg, F. Krombach, "Proinflammatory and cytotoxic response to nanoparticles in precision-cut lung slices", Beilstein Journal of Nanotechnology 5 (2014) 2440-2449

A. Vogt, F. Rancan, S. Ahlberg, B. Nazemi, C.S. Choe, M.E. Darvin, U. Blume-Peytavi, K. Loza, J. Diendorf, M. Epple, C. Graf, E. Rühl, M.C. Meinke, J. Lademann, "Interaction of dermatologically relevant nanoparticles with skin cells and skin", Beilstein Journal of Nanotechnology 5 (2014) 2363-2373

S. Ahlberg, A. Antonopoulos, J. Diendorf, R. Dringen, M. Epple, R. Flöck, W. Goedecke, C. Graf, N. Haberl, J. Helmlinger, F. Herzog, F. Heuer, S. Hirn, C. Johannes, S. Kittler, M. Köller, K. Korn, W.G. Kreyling, F. Krombach, J. Lademann, K. Loza, E.M. Luther, M. Malissek, M.C. Meinke, D. Nordmeyer, A. Pailliart, J. Raabe, F. Rancan, B. Rothen-Rutishauser, E. Rühl, C. Schleh, A. Seibel, C. Sengstock, L. Treuel, A. Vogt, K. Weber, R. Zellner, "PVP-coated, negatively charged silver nanoparticles: A multi-center study of their physicochemical characteristics, cell culture and in vivo experiments", Beilstein Journal of Nanotechnology 5 (2014) 1944–1965

F. Herzog, K. Loza, S. Balog, M.J.D. Clift, M. Epple, P. Gehr, A. Petri-Fink, B. Rothen-Rutishauser, "Mimicking exposures to acute and lifetime concentrations of inhaled silver nanoparticles by two different in vitro approaches", Beilstein Journal of Nanotechnology 5 (2014) 1357-1370

K. Loza, C. Sengstock, S. Chernousova, M. Köller, M. Epple, "The predominant species of ionic silver in biological media is colloidally dispersed nanoparticulate silver chloride", RSC Advances 4 (2014) 35290–35297

K. Loza, J. Diendorf, C. Sengstock, L. Ruiz-Gonzalez, J. M. Gonzalez-Calbet, M. Vallet-Regi, M. Köller, M. Epple, "The dissolution and biological effects of silver nanoparticles in biological media", Journal of Materials Chemistry B 2 (2014) 1634–1643

S. Banerjee, K. Loza, W. Meyer-Zaika, O. Prymak, M. Epple, "Structural evolution of silver nanoparticles during wet-chemical synthesis", Chemistry of Materials 26 (2014) 951-957

Z.Z. Zyman, D.V. Rokhmistrov, K.I. Loza, "Determination of the Ca/P ratio in calcium phosphates during the precipitation of hydroxyapatite using X-ray diffractometry", Processing and Application of Ceramics 7 (2013) 93-95

D.V. Rokhmistrov, O.T. Nikolov, O.A. Gorobchenko, K.I. Loza, "Study of structure of calcium phosphate materials by means of electron spin resonance", Applied Radiation and Isotopes 70 (2012) 2621-2626

8.3 Posters and presentations

Microstructure physics and alloy design department, Max-Planck-Institut für Eisenforschung, Düsseldorf, Germany, 10.11.2015, K. Loza, "Nanostructure of wet-chemically prepared, polymer-stabilized silver-gold nanoalloys (6 nm) over the entire composition range" (oral presentation)

Jahrestagung der Deutschen Gesellschaft für Biomaterialien, Freiburg, Germany, 12.-14.11.2015 C. Greulich, K. Loza, M. Epple, T. Schildhauer, M. Köller, "Silver chloride nanoparticles have a higher antimicrobial activity compared to than silver nanoparticles" (oral presentation)

Ukrainian-German Symposium on Nanoscience and Nanotechnology, Kyiv, Ukraine, 22.-25.09.2015, K. Loza, J. Diendorf, S. Chernousova, C. Sengstock, M. Köller, M. Epple, "On the behavior of silver nanoparticles in complex media" (oral presentation)

27th European Conference on Biomaterials ESB 2015, Krakow, Poland, 30.08-3.09.2015, M. Epple, S. Chernousova, K. Loza, O. Prymak, M. A. Surmeneva, R. Surmenev, "Antimicrobial effects of biomaterials: Silver ions, silver nanoparticles and antimicrobial peptides" (oral presentation)

Recent advances in nano-science and technology (RAINSAT-2015), Chennai, India, 8.-10.07.2015, K. Loza, S. Berger, K. Wallat, M. Gepp, R. Le Harzic, H. Zimmermann, F. Stracke, M. Epple, "Electrophoretic deposition of calcium phosphate nanoparticles on nanostructured silicon surfaces" (oral presentation)

Chemistry Department, Panjab University, Chandigarh, India, 15.07.2015, K. Loza, "Inorganic nanoparticles for biomedical application" (oral presentation)

Crystal Growth Center, Anna University, Chennai, India, 13.07.2015, K. Loza, "Inorganic nanoparticles for biomedical application" (oral presentation)

8th Annual meeting of Scandinavian Society for Biomaterials, Sigulda, Latvia, 6.- 8.05.2015, A.A. Ivanova, R.A. Surmenev, M.A. Surmeneva, T.M. Mukhametkaliyev, K. Loza, O. Prymak, M. Epple, "Hydroxyapatite-based biocomposite with silver nanoparticles: synthesis and characterization" (oral presentation)

TERMIS 2014, Washington, D.C., USA, 13.-16.12.2014, C. Sengstock, K. Loza, M. Epple, T. Schildhauer, M. Köller, "Effect of Silver Nanoparticles on the Differentiation of Human Mesenchymal Stem Cells" (oral presentation)

MRS Fall Meeting 2014, 30.11.-06.12.2014, Boston, USA, K. Loza, C. Sengstock, S. Chernousova, M. Köller, M. Epple, "The predominant species of ionic silver in biological media is colloidally dispersed nanoparticulate silver chloride" (oral presentation)

9th IFOST, Chittagong, Bangladesh, 21.-23.10.2014, A.A. Ivanova, R.A. Surmenev, M.A. Surmeneva, T.M. Mukhametkaliyev, K. Loza, S. Chernousova, O. Prymak, M. Epple, "Antibacterial sandwich-structured biocomposites" (oral presentation)

International Conference on Thin Films (ICTF-16), Dubrovnik, Croatia, 13.-16.10.2014, A.A. Ivanova, R.A. Surmenev, M.A. Surmeneva, T.M. Mukhametkaliyev, K. Loza, O. Prymak, M. Epple, "A novel biocompatible composite with a tunable antibacterial activity" (poster)

Biomaterials in Medicine and Veterinary Medicine, Rytro, Poland, 9.-12.10.2014, K. Loza, J. Diendorf, C. Sengstock, M. Köller, M. Epple, "On the nature of silver ions in complex media" (oral presentation)

EUROTOX Congress 2014, Edinburgh, Great Britain, 7.-10.09.2014, G.A. Westphal, I. Schremmer, A. Rostek, K. Loza, N. Rosenkranz, T. Brüning, M. Epple, J. Bünger, "NR8383 rat macrophages can induce migration of differentiated HL-60 cells following challenge with TiO_2, SiO_2 or carbon black" (poster)

26th Annual Conference of the European Society for Biomaterials (ESB), Liverpool, Great Britain, 31.08.-03.09.2014, A.A. Ivanova, R.A. Surmenev, M.A. Surmeneva, T. Mukhametkaliyev, K. Loza, O. Prymak, M. Epple, "Synthesis of a bifunctional silver-containing biocomposite" (oral presentation)

XII International Conference on Nanostructured Materials (NANO 2014), Moscow, Russia, 13.-18.07.2014, A.A. Ivanova, K. Loza, O. Prymak, M. Epple, M.A. Surmeneva, R.A. Surmenev, "A novel dual action tunable antimicrobial silver-containing biocomposite", (oral presentation)

28th International Conference on Surface Modification Technologies (SMT28),16.-18.06.2014, Tampere, Finland, A.A. Ivanova, K. Loza, O. Prymak, M. Epple, M.A. Surmeneva, R.A. Surmenev, "Functionalization of titanium surface with silver nanoparticles and an RF-magnetron sputter-deposited calcium phosphate coating for biomedical application" (oral presentation)

NANOTOX 2014, 7th International Nanotoxicology Congress, Antalya, Turkey, 23.-26.04.2014, S. Hirn, N. Haberl, K. Loza, M. Epple, W. G. Kreyling, B. Rothen-Rutishauser, M. Rehberg, F. Krombach, "Cytotoxic and inflammatory response to nanoparticles in precision-cut lung slices" (poster)

MRS Fall Meeting 2013, Boston, USA, 1.-6.12.2013, K. Loza, S. Banerjee, W. Meyer-Zaika, O. Prymak, M. Epple, "Structural evolution of silver nanoparticles during wet-chemical synthesis" (poster)

Nanosafety 2013, Saarbrucken, Germany, 20.-22.11.2013, S. Hirn, N. Haberl, K. Loza, M. Epple, W. G. Kreyling, B. Rothen-Rutishauser, M. Rehberg, F. Krombach, "Are precision-cut lung slices (PCLS) an effective tool for in vitro nanotoxicology studies?" (poster)

German-Russian Workshop "Coated Surfaces for biomedical application", Essen, Germany, 4.-5.11.2013, K. Loza, M. Epple, "Scanning electron microscopy to characterize coatings" (oral presentation)

6th Late Summer Workshop "Micropollutants in the water cycle" Schloss Maurach, Lake Constance, Germany, 29.09-2.10.2013, K. Loza, J. Diendorf, C. Greulich, M. Köller, M. Epple, "On the behavior of silver nanoparticles in complex media" (poster)

Jahrestagung der Deutschen Gesellschaft für Biomaterialien, Erlangen, Germany, 6.-28.09.2013, C. Greulich, K. Loza, M. Epple, T. Schildhauer, M. Köller, "Subtoxic concentrations of nano-silver influence human stem cell differentiation" (poster)

Microscopy Conference MC2013, Regensburg, Germany, 25.-30.08.2013, K. Loza, D. Kozlova, M. Epple, "Visualization of cell-nanoparticle interactions by scanning electron microscopy" (poster)

MRS Spring Meeting 2013, San Francisco, USA, 1.-5.04.2013, K. Loza, C. Greulich, M. Koeller, M. Epple, "On the nature of silver ions in biological media" (oral presentation)

QualityNano, Prag, Czech Republic, 27.02.-1.03.2013, S. Hirn, N. Haberl, F. Herzog, K. Loza, M. Epple, W. G. Kreyling, B. Rothen-Rutishauser, F. Krombach, "Are precision-cut lung slices (PCLS) an effective tool for in vitro nanotoxicology studies?" (poster)

Russian-German Workshop "Biocompatible Materials and Coatings: Fundamental Problems & Trends, Biomedical Applications" (BMC-2013), Tomsk, Russia, 24.- 27.02.2013, K. Loza, C. Greulich, M. Köller, M. Epple, "On the nature of silver ions in biological media" (oral presentation)

Russian-German Workshop "Biocompatible Materials and Coatings: Fundamental Problems & Trends, Biomedical Applications" (BMC-2013), Tomsk, Russia, 24.-

27.02.2013, O. Prymak, S. Banerjee, K. Loza, W. Meyer-Zaika, M. Epple, "X-ray powder diffraction as tool to investigate the ultrastructure of nanoparticles" (oral presentation)

German-Ukrainian Symposium on Physics and Chemistry of Nanostructures and on Nanobiotechnology, Ilmenau, Germany, 18.-20.09.2012, K. Loza, M. Epple, "On the nature of silver ions in biological media" (oral presentation)

8.4 Curriculum vitae

Der Lebenslauf ist in der Online-Version aus Gründen des Datenschutzes nicht enthalten.

8.5 Acknowledgments

I would like to express my sincere gratitude to

My advisor Prof. Dr. Matthias Epple for the continuous support of my PhD study and related research, for providing me with the interesting interdisciplinary research topic, motivation, and enabling many research stays and presentations at numerous conferences abroad,

Prof. Dr. Christian Mayer for assessment of the dissertation,

Prof. Dr. Manfred Köller and Jun.-Prof. Dr. Christina Sengstock for outstanding collaboration and fruitful scientific discussions,

Prof. Dr. Jürgen Bünger, Dr. Götz Westphal and Dr. Isabell Schremmer for productive cooperation and discussions,

Dr. Oleg Prymak for performing extensive X-ray powder diffraction studies and numerous discussions,

Dr. Wolfgang Meyer-Zaika for providing TEM images, assistance in the field of electron microscopy and friendly conversations,

Mr. Soham Banerjee for a nice teamwork in laboratory in Essen as well as in New York,

Mr. Christoph Jensky and Mr. Tim Unterschemmann for providing numerous sample preparations for dissolution studies,

Mrs. Ursula Giebel and Mr. Smail Boukercha for the assistance and perfect teamwork in the electron microscopy laboratory,

Mr. Jürgen Gündel-Graber for assistance with numerous X-ray diffraction measurements and friendly conversations,

Mrs. Veronika Hiltenkamp, Mrs. Kerstin Brauner and Mr. Robin Meya for many AAS measurements and testing different analytical protocols,

Mrs. Sabine Bollmann, Mrs. Carola Fischer and Mrs. Sabine Kiefer for kind assistance with paperwork,

Mrs. Carola Fischer, Dr. Gregor Dördelmann and Mr. Jens Nelsen for technical assistance in hardware and software configuration,

Dr. Svitlana Chernousova for performing cell biological studies, valuable comments and suggestions as well as friendly support over the entire work,

Dr. Diana Kozlova for cell biological studies, stimulating discussions, and helpfulness,

Dr. Simon Ristig, Dr. Jörg Diendorf and Mr. Alexander Rostek for a nice work in priority program, friendly lab assistance and pleasant time in Fulda and Berlin,

Dr. Simon Ristig for a wonderful time as a lab mate and friendly guidance into a noble art of music,

Dr. Gregor Dördelmann, Dr. Joachim Enax, Dr. Johannes Rüsing, Dr. Alexander Peetsch, Dr. Sven Range, Dr. Volker Seifarth, Mr. Bernhard Richard Heinrich Neuhaus, Mrs. Olga Rotan, Dr. Viktoriya Sokolova, Dr. Jan Klesing, Dr. Sven Backhaus, Mrs. Sabrina Daumann, Mrs. Alwina Lübke, Dr. Janina Petrack, Mrs. Tatiana Ruks, Mr. Jens Nelsen, Mrs. Anna Ivanova, Mrs. Viktoria Grasmik, Dr. Katrin Wallat, Mr. Benjamin Schütze and Mr. Jens Helmlinger for enjoyable moments and helpfulness in everyday lab life,

My family for their love, helpfulness and support.

Eidesstattliche Erklärung

Hiermit versichere ich, dass ich die vorliegende Arbeit mit dem Titel

"Behavior of toxicologically relevant silver compounds and barium sulfate particles in complex media: from synthesis to biological investigations**"**

selbst verfasst und keine außer den angegebenen Hilfsmitteln und Quellen benutzt habe, und dass die Arbeit in dieser oder ähnlicher Form noch bei keiner anderen Universität eingereicht wurde.

Essen,